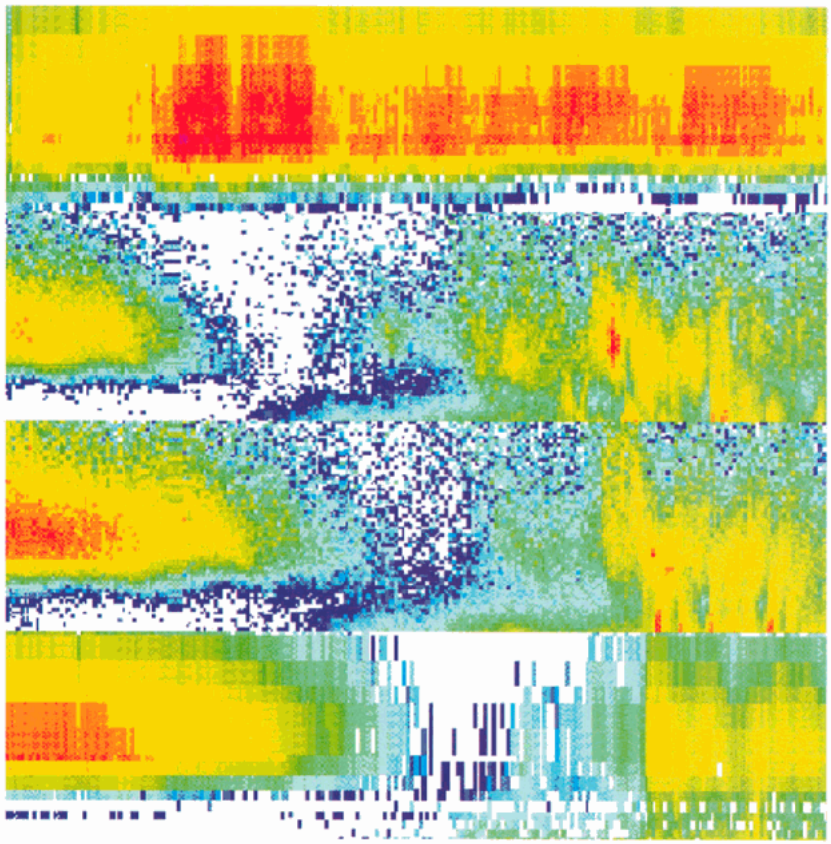

EISCAT

EUROPEAN INCOHERENT SCATTER SCIENTIFIC ASSOCIATION

ANNUAL REPORT
1996 - 1997

SE-981 28 KIRUNA, SWEDEN

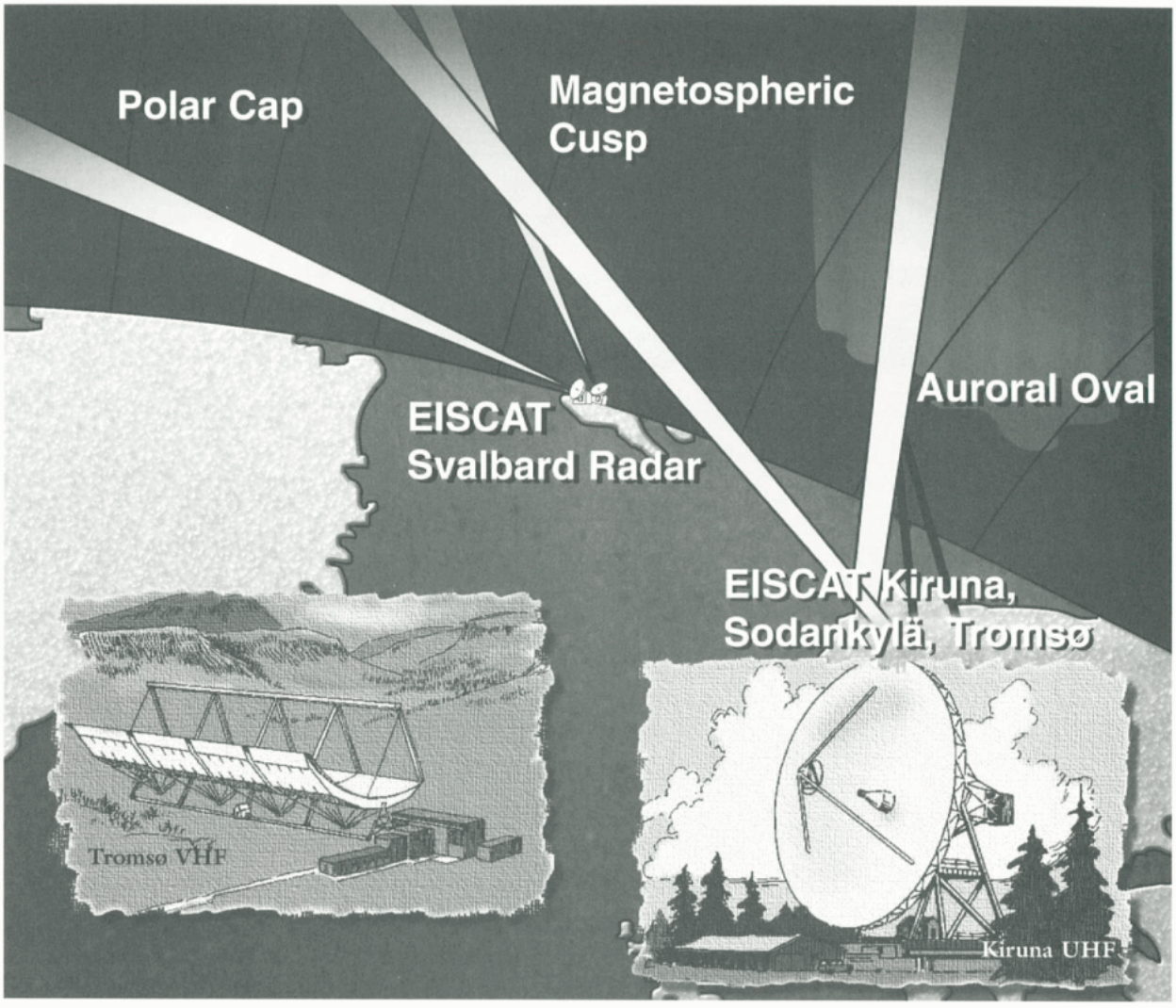

EISCAT Radar Systems

Location		Tromsø	Kiruna	Sodankylä	Longyearbyen	
Geograph. Coordinates		69°35´N	67°52´N	67°22´N	78°09´N	
		19°14´E	20°26´E	26°38´E	16°02´E	
Geomagn. Inclination		77°30´N	76°48´N	76°43´N	82°06´N	
Invariant Latitude		66°12´N	64°27´N	63°34´N	75°18´N	
Band	VHF	UHF	UHF	UHF	UHF	
Frequency (MHz)	224	931	931	931	500	
Max. bandwith (MHz)	3	8	8	8	10	
Transmitter	2 klystr	1 klystr	-	-	16 klystr	
Channels	8	8	8	8	6	
Peak power (MW)	2x1.5	1.5	-	-	1.0	
Average power (MW)	2x0.15	0.15	-	-	0.25	
Pulse duration (msec)	.001-2.0	.001-1.0	-	-	<.001-2.0	
Phase coding	binary	binary	binary	binary	binary	
Min. interpulse (msec)	1.0	1.0	-	-	0.1	
Receiever	analog	analog	analog	analog	anal.-digital	
Sustem temperature (K)	250-350	90-110	30-35	30-35	55-65	
Digital processing	8 bit ADC, 32 bit complex, autocorrelation functions, parallel channels				12 bit ADC, lag profiles 32 bit complex	
					Antenna 1	Antenna 2*
Antenna	parabolic cylinder 120m x 40m Steerable	parabolic dish 32m Steerable	parabolic dish 32m Steerable	parabolic dish 32m Steerable	parabolic dish 32 m Steerable	parabolic dish 42m Fixed
Feed system	line feed 128 crossed dipoles	Cassegrain	Cassegrain	Cassegrain	Cassegrain	Cassegrain
Gain (dBi)	46	48	48	48	42,5	45
Polarization	circular	circular	any	any	circular	circular

* Antenna 2 under construction

EISCAT Heating Facility in Tromsø

Frequency range: 4-8 MHz, Maximum transmitter power: 12 x 0.1 MW, Antennas: two arrays (4-8MHz): 24dBi, one array (5.4-8MHz): 30 dBi. Additionally a Dynasonde is operated at the Heating facility.

Front cover: approximately three hours of electron density data (see page 62) recorded simultaneously on March 14 1997 by the ESR (top), two independent beams of the VHF (middle) and the UHF radars.

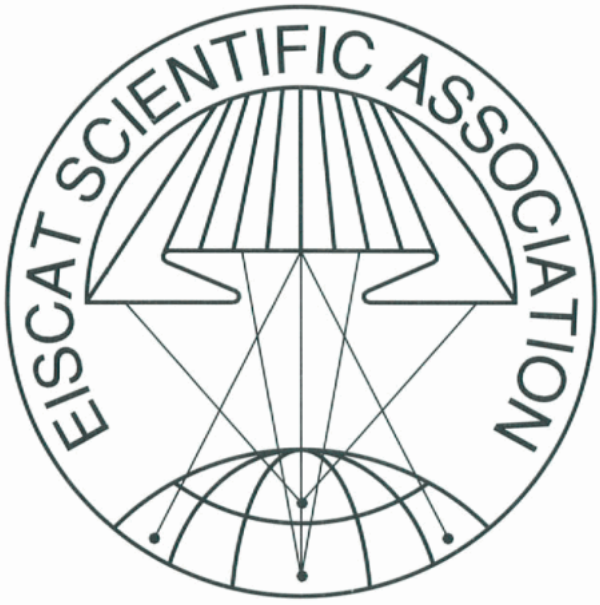

ANNUAL REPORT 1996-1997

EISCAT, the European Incoherent Scatter Scientific Association, is established to conduct research on the lower, middle and upper atmosphere and ionosphere using the incoherent scatter radar technique. This technique is the most powerful ground-based tool for these research applications. EISCAT is also being used as a coherent scatter radar for studying instabilities in the ionosphere, as well as for investigating the structure and dynamics of the middle atmosphere and as a diagnostic instrument in ionospheric modification experiments with the Heating facility.

There are ten incoherent scatter radars in the world, and EISCAT operates three of the highest-standard facilities. The experimental sites of EISCAT are located in the Scandinavian sector, north of the Arctic Circle. They consist of two independent radar systems on the mainland, together with a new radar constructed on the island of Spitsbergen in the Svalbard archipelago - the EISCAT Svalbard Radar (see schematic and operating parameters on the inside of the front cover).

The EISCAT UHF radar operates in the 931 MHz band with a peak transmitter power of 1.5 MW and 32 m, fully steerable parabolic dish antennas. The transmitter and one receiver are in Tromsø (Norway). Receiving sites are also located near Kiruna (Sweden) and Sodankylä (Finland), allowing continuous tristatic measurements to be made.

The monostatic VHF radar in Tromsø operates in the 224 MHz band with a peak transmitter power of 2 x 1.5 MW and a 120 m x 40 m parabolic cylinder antenna, which is subdivided into four sectors. It can be steered mechanically in the meridional plane from vertical to 60o north of the zenith; limited east-west steering is also possible using alternative phasing cables.

The EISCAT Svalbard radar (ESR), located near Longyearbyen, operates in the 500 MHz band with a peak transmitter power of 0.5 MW (modular design allowed to rise this to 1.0 MW) and a fully steerable parabolic dish antenna of 32 m diameter (another antenna is being added). The high latitude location of this facility is particularly aimed at studies of the cusp and polar cap region.

The basic data measured with the incoherent scatter radar technique are profiles of electron density, electron and ion temperature and ion velocity. Subsequent processing allows a wealth of further parameters, describing the ionosphere and neutral atmosphere, to be derived. A selection of well-designed radar pulse schemes are available to adapt the data-taking routines to many particular phenomena, occurring at altitudes between about 50 km and more than 2000 km. Depending on geophysical conditions, a best time resolution of less than one second and an altitude resolution of a few hundred meters can be achieved.

Operations of approximately 1700 hours each year are distributed equally between Common Programmes (CP) and Special Programmes (SP). At present, six well-defined Common Programmes are run regularly, for between one and three days, typically about once per month, to provide a database for long term synoptic studies. A large number of Special Programmes, defined individually by Associate scientists, are run to support national and international studies of both specific and global geophysical phenomena.

The Annual Reports present a summary of EISCAT's operations, developments, scientific results, publications, budget and Council and committee structure for each year. Further details of the EISCAT system and operation can be found in various EISCAT reports, including illustrated brochures, which can be obtained from EISCAT Headquarters in Kiruna, Sweden.

The investments and operational costs of EISCAT are shared between:

Suomen Akatemia, Finland
Centre National de la Recherche Scientifique, France
Max-Planck-Gesellschaft, Federal Republic of Germany
National Institute of Polar Research, Japan
Norges Forskningsråd, Norway
Naturvetenskapliga Forskningsrådet, Sweden
Particle Physics and Astronomy Research Council, United Kingdom

EISCAT ANNUAL REPORT 1996-1997

CONTENTS

	Page
Council Chairmens' Page	5
Outgoing Director's Final Report	7
EISCAT Operations 1996-1997	23
Scientific Research and Developments	
Geomagnetic pulsations and ULF waves	27
Mesosphere and D-Region	28
Polar Mesospheric Summer Echoes (PMSE)	32
Meteor Studies	34
Particle Precipitation and Auroral Processes	36
E-Region	42
Neutral Atmosphere	45
Atmospheric Gravity Waves and TIDs	49
Coupling Between the Thermosphere, Ionosphere, and Magnetosphere	52
Storms and substorm	55
The Ionospheric Trough	62
Topside Ionosphere	62
Large Scale Electrodynamics and Convection	64
Non-Thermal plasma Echoes	67
Ionospheric Tomography	68
Ionospheric Modelling	70
Ionospheric Modification (Heating)	72
Passive Observations: Interplanetary Scintillation	77
Search for new radar coding schemes	78
Data Analysis Techniques	80
EISCAT Svalbard Radar – technical highlights	83
Publications	93
Reports and Meetings	102
Balance Sheets	103
EISCAT Council, Committes and Senior Staff	106
The EISCAT Associates	Inside back cover
Addresses	Back Cover

Council Chairmens' Page

This introduction to the biannual report for the period 1996-1997 cover a period straddling that of two chairmen, hence this joint introduction.

The period was marked by a number of events boding well for the long-term future of EISCAT. The major one was the opening of the EISCAT Svalbard Radar (ESR), an incoherent scatter radar system operating with a fully steerable dish antenna allowing studies of the ionosphere and convection over the polar cap region. The first observations were made in March 1996. This crowned a major effort by the EISCAT staff, to design, develop and build a facility with a number of novel technical features. It is clear that without the major contribution and dedication of the EISCAT staff, the facility could never have been completed on time and within the tight budget.

In August 1996, the official inauguration of the new facility took place in Longyearbyen, with 200 guests from 12 countries, including the president of the Norwegian Parliament and ambassadors, officials from the EISCAT member countries and representatives of the international scientific community. The Norwegian Minister of Education, Science and Church Affairs, Mr. Reidar Sandal, formally opened the facility by setting the antenna in motion and starting an observing session. On 30 August 1996 the opening was also celebrated with a special session at the General Assembly of the International Union of Radio Science (URSI) held in Lille.

Japan became a full official member of the EISCAT Association in April 1996. This enabled the Association to plan new technical improvements to the system. An additional antenna to allow squinted beam operation was studied, and an increase in the transmitter power to 1 MW was considered. These two improvements will have major impacts on the science activities of the Association. The power increase improves the sensitivity of the radar, making it possible to measure at higher altitudes or greater ranges and to increase the time resolution. The construction of the new antenna, made possible thanks to the new funds provided by Japan, will give EISCAT the ability to observe in two directions at the same time and therefore account for the spatial variability of the ionosphere. An antenna manufacturer was selected on the basis of several proposals and the Council decided to build the second antenna. The antenna will be completed in 1999.

In 1997, the Council decided to entrust the direction of the Association to Dr. Tauno Turunen. Dr. Jürgen Röttger at that time had been EISCAT Director for eleven years and has played a major role in EISCAT life. It is especially to his credit that the ESR planning and construction could be completed so successfully. We owe our most sincere thanks to Jürgen Röttger for his contribution to EISCAT and for his untiring efforts to make EISCAT a scientific endeavour to be counted in the international scientific community.

The new Director, Tauno Turunen, is well known to the community through his long association with EISCAT. He will have a difficult role, especially because of the budget restrictions facing the majority of European countries. These budgetary problems will be a major challenge for the Council to solve in the future.

The long list of publications resulting from EISCAT work, the frequent use of EISCAT data in the interpretation of space experiments and the number of scientists participating in EISCAT experiments show that EISCAT plays a crucial role in the scientific community. This role is bound to increase with the launch of several new space missions, such as CLUSTER, in the not too distant future. The role of the Council will be to solve the difficult budgetary problems by a number of measures such as increasing the membership of the Association and by encouraging new uses of EISCAT.

T. Hagfors
Chair 1995-1996

W. Kofman
Chair 1997-1998

Outgoing Director's Final Report
Years 1996 and 1997

This report covers the years 1996 and 1997 and comprises also the final report of the Director in charge of the EISCAT management for the period 1986 to 1997. This period ended with the basic completion of the EISCAT Svalbard Radar (ESR), which had been the major challenge during the past five years. A complete description of this project has been published in the EISCAT Annual Report 1994-1995. The major events in the two following years were the initial operation of the ESR, the first detection of echoes from the ionosphere and the inauguration of this new facility, the increase of the transmitter power and the planning of the second antenna for the ESR. Another notable event was the expansion of the EISCAT Scientific Association by the new Associate Japan. The following part of this report deals with details of these events. It also summarises the development and operation of the EISCAT mainland systems in Kiruna, Sodankylä and Tromsø.

Following its final acceptance test, the ESR antenna was taken over from Kvaerner-Kamfab on 1 March 1996. The antenna was then used for further intensive tests for electromagnetic compatibility and potential interference. At the same time the final integration and tests of the receiver, exciter, controller and the digital-signal-processing systems of the ESR was done at Kiruna site in the beginning of March 1996. These units were shipped thereafter to Svalbard for on-site integration, which took place in the middle of March. All these tests proved to be successful and experimental operation could commence. The first operation of the ESR on 16 March 1996 was outstanding, since good data were recorded from the beginning. The experiment code GUP0 used six frequency channels and a 360 microsecond long pulse. Some ten hours of good ionospheric data were recorded during this initial period and the first on-line analysis showed exemplary spectra (Figure 1 and Figure 2). The colour plot in Figure displays the temporal development of these basic plasma parameters in the F-region over Svalbard. These initial experiments proved the EISCAT Svalbard Radar to be basically ready as planned for the ground-based co-operation with the Cluster mission.

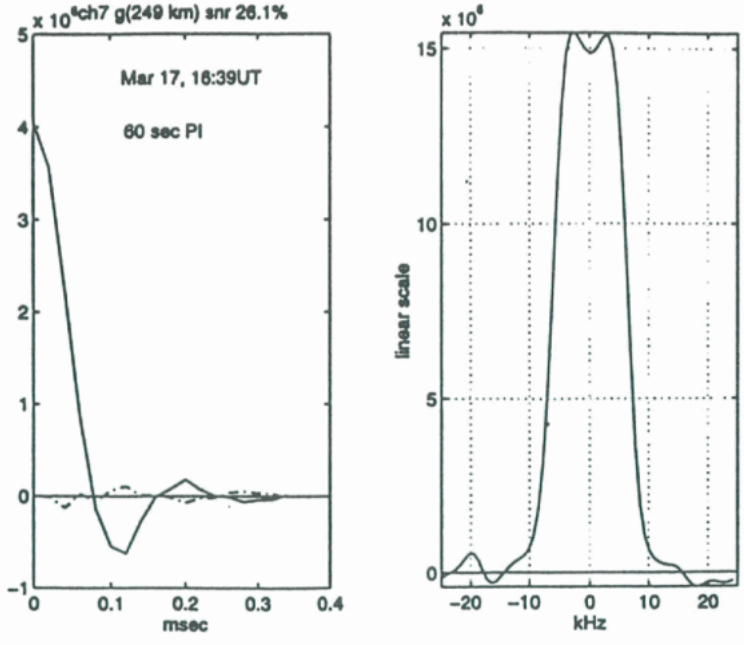

Figure 1: The first autocorrelation function and spectrum of incoherent scatter signals from the ionosphere over Svalbard observed at 16:39 UT on 17 March 1996

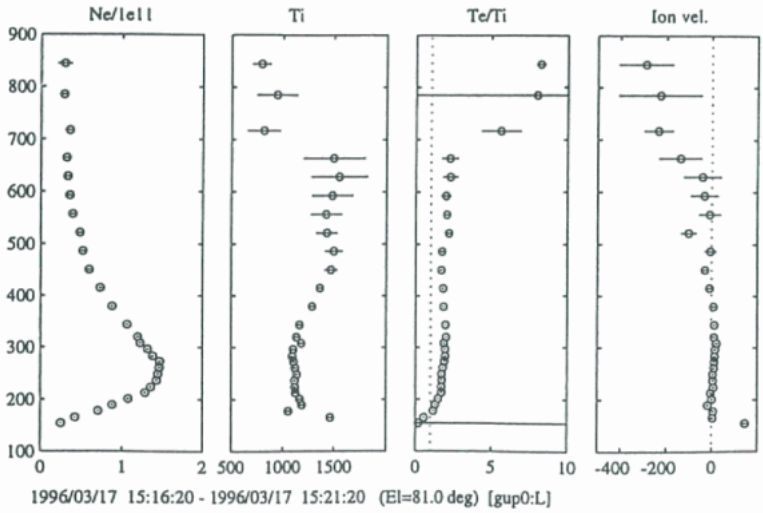

Figure 2: Height profiles of the basic plasma parameters (electron density Ne, electron temperature Te, and ratio of electron and ion temperature Te/Ti and the ion velocity) deduced with the GUISDAP analysis program at the EISCAT Svalbard Radar

During the years 1996 and 1997 the EISCAT Svalbard Radar operated with 500 kW peak power and the fully steerable dish antenna (detailed system parameters were given on page 35 of the EISCAT Annual Report 1994-1995). The analysis of the data was done by the GUISDAP software package, which was supplied to EISCAT as an in-kind contribution by Finland. Besides the engineering software designed by EISCAT staff, which is extensively used in the experiments, further user-oriented software for on-line control and monitoring of the ESR was made available through a contract with Rutherford Appleton Laboratory/CLRC of the United Kingdom.

The month of March in 1996 represented another exceptional highlight in the history of EISCAT, since during this time the final negotiations with the National Institute of Polar Research (NIPR) in Tokyo and the Solar-Terrestrial Environment Laboratory (STEL) in Nagoya took place to assure a timely joining of Japan into the EISCAT Scientific Association. The finalisation of administrative procedures and the modification of the EISCAT Agreement was performed in time such that Japan became a full member of the Association on 1 April 1996. Figure 3 shows the Director of NIPR and the Director of EISCAT after completing the final administrative negotiations.

Figure 3: Prof. T. Hirasawa, Director of NIPR, and Dr. J. Röttger, Director of EISCAT, on 30 March 1996 at the National Institute of Polar Research in Tokyo.

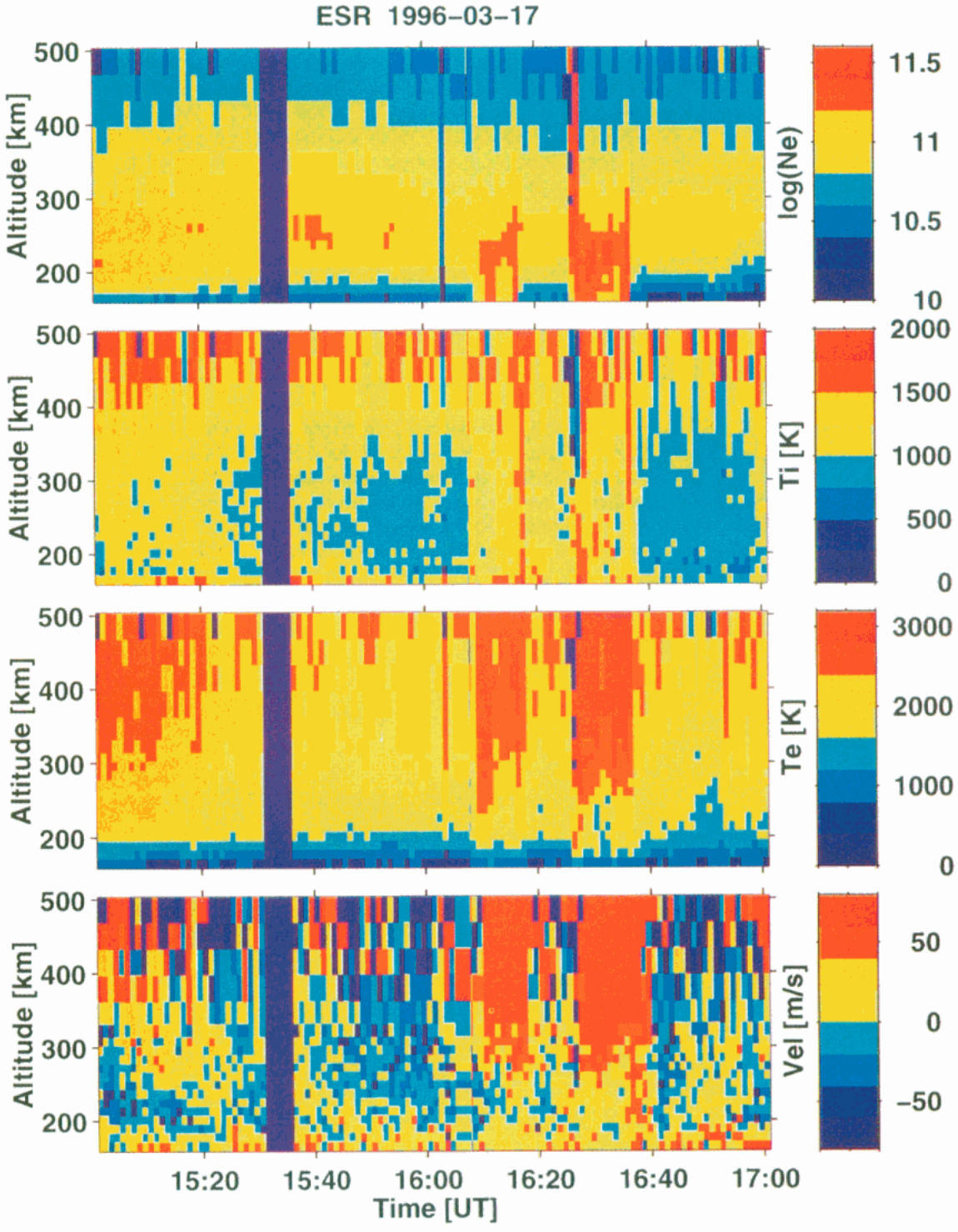

Figure 4: The temporal variation of ionospheric plasma parameters derived from the EISCAT Svalbard Radar raw data by the analysis program GUISDAP

On 22 August 1996 the formal inauguration of the EISCAT Svalbard Radar took place. This was preceded by intense preparations during the summer months in order to accommodate the reception of more than 200 guests from 12 countries. The opening of the ESR was done by the Norwegian Minister of Education, Science and Church Affairs, Mr. Reidar Sandal. The ambassadors to Norway of Japan and Germany were present and high level delegates from all seven EISCAT Associates' countries attended the opening ceremony. Other incoherent scatter radar facilities and geophysical observatories and universities were represented. Prof. William E. Gordon, the founding father of the incoherent scatter radar technique, gave the inaugural speech (see photographs between pages 19 and 22).

Following the inauguration on Svalbard a special session and a reception were held on 30 August 1996 at the General Assembly of the International Union of Radio Science - URSI - in Lille, France, where the scientific community was informed about the EISCAT Svalbard Radar as a new international facility opened for polar ionosphere and atmosphere research. A paper on the innovative technical design of the ESR was presented at the URSI Assembly by the Deputy Director Technical, Dr. Gudmund Wannberg. It was subsequently published in the journal Radio Science with the title "The EISCAT Svalbard Radar: A case study in modern incoherent scatter radar system design".

The completion of the EISCAT Svalbard Radar represents a significant evolution and expansion of the EISCAT radar systems. This project has been funded jointly by the EISCAT Associates. The funding, which accumulated over the years 1990-1997, is shown in the graphics of Figure 5 shows the distribution of the funds to the different system parts of the ESR. Following the new Agreement between the EISCAT Associates the contributions to the operating costs have been adjusted as shown in Figure . The system usage and distribution of observation time of the ESR and the mainland KST sites to the Associates has been revised accordingly. The EISCAT Agreement had been revised, signed and is printed in a new edition of the Blue Book.

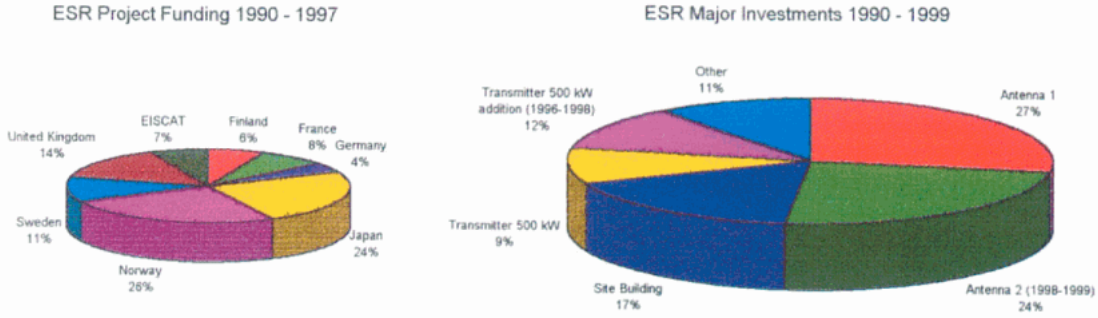

Figure 5

The total investment costs for the EISCAT Svalbard Radar project are 175 million Swedish Crowns, which also cover the expansion to the 1000 kW transmitter and the second antenna.

The annual operating costs of the EISCAT systems, including the ESR, had been 29 million SEK (see after page 103 for exact numbers), and are provided by the Associates according to a share depicted in the right-hand-side pie chart.

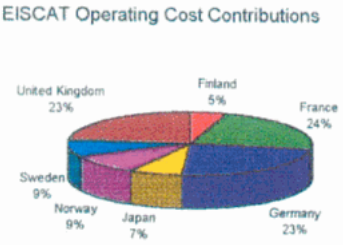

Figure 6

Further engineering and system tests of the ESR followed during the remaining part of 1996. These included also some more experiment operation. The Final Presentation Meeting (FPM) of the ESR project took place in Tromsø on 25-28 November 1996 after the 42nd EISCAT Council Meeting. This FPM was combined with the Annual Review Meeting of all EISCAT staff. During these meetings technical and organisational matters of the ESR and the mainland systems (KST = Kiruna-Sodankylä-Tromsø) were presented and discussed. Upgrading of the ESR hardware by expanding the transmitter peak power to 1000 kW and adding a second antenna were specified, as well as an outline of adjustments and modifications of the digital-signal-processing (DSP). The latter has special importance in view of the ageing DSP at the mainland KST sites. Upgrading of the front-end at the Tromsø UHF radar is also considered essential, since it would significantly reduce the system temperature. The recent years have essentially been used to concentrate on the construction of the ESR and staff have not been available for dedicated and time-consuming developments at the KST sites. It was foreseen, that funds saved and set aside for the purpose of this kind of upgrading would be used in the coming years to design and construct the corresponding system components.

The final balance of the budget of the EISCAT Svalbard Radar allowed an upgrading of the transmitter. The modular transmitter and the ESR building at the site near Longyearbyen were initially designed to encompass such an upgrade by adding more transmitter units, since the corresponding power increase would improve the system sensitivity. It was, thus, a natural evolutionary step to increase the transmitter power to 1000 kW. At the end of 1996 a contract was signed with Harris Corporation Broadcast Division in Cambridge, UK, for the construction and commissioning of this transmitter expansion. This contract included the combining of the transmitter power of the first 500-kW unit with the newly added 500-kW unit. The following drawing (Figure 7) shows the layout of the total 1000-kW transmitter, where the newly added part is drawn in dark. The system is designed such that the transmitted power can be switched from pulse to pulse from one antenna to a second antenna. This transmitter upgrade was installed at the ESR site in time at the end of 1997 and was tested at full power soon thereafter.

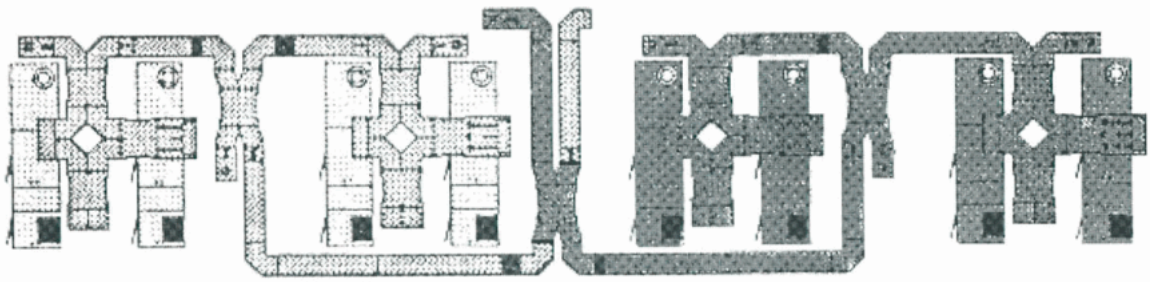

Figure 7: The lay-out of the total ESR transmitter, consisting of 8 sub-units

After Japan became a member of EISCAT it was possible to focus also on the second antenna for the ESR. Based on input from the EISCAT Executive, detailed considerations of scientific merits were debated by the Scientific Advisory Committee about the design of this antenna. It was finally decided to choose a fixed dish antenna with larger aperture than the first antenna and assuring a gain of 45 dBi and extreme sidelobe suppression, and one pointing direction parallel to the Earth's magnetic field. Requests for proposals were issued in spring 1997. By the deadline of 1 August 1997 six proposals were received at Headquarters and initially evaluated. An evaluation committee, consisting of members from all EISCAT Associates and the Director designate, were called to analyse the proposals in collaboration with the EISCAT Executive. Short-listed bids were also assessed by the consulting company TICRA. Two proposals were thereafter screened by the Scientific Advisory Committee and the Administrative and Finance Committee. This resulted in a proposal to the Council at its meeting on 17/18 November 1997. The Council then decided to choose Alcatel of France as the successful bidder to construct the second antenna for the EISCAT Svalbard Radar.

Besides many engineering tests, performance improvements and continuing development of software, the ESR was operated in experimental observations for 42 hours in the year 1996. All these operations were with the long-pulse code GUP0 with some tests of the GUP1 code (a combination of alternating code and long pulse). In 1997 a total of 420 hours of experiments were operated at the ESR. Most of these were in campaign modes, which took place about once per month. As much as possible, these operations were done concurrent with the mainland KST operations, covering international incoherent scatter world-days as well as particular satellite passes. Some of these operations were in modes where the antenna was pointing at elevation angles down to 45 degrees.

All the operations with the ESR showed that there exist significant clutter echoes through antenna sidelobes from mountains out to distances of about 105 km. This was a major concern, since the unwanted clutter contaminated the standard observations with long and coded pulses at ranges smaller than about 150 - 180 km. The plot in Figure indicates for instance no data below 180 km, because the analysis routine did not converge due to the clutter. Further test operations were subsequently done in 1997 to deduce specific characteristics of this ground clutter to investigate how it could be removed. A long complementary code was implemented, which was properly adapted for the dual purpose for D-region/mesosphere observations as well as to study ground clutter profiles. Figure shows a typical clutter profile caused by leakage of power through antenna sidelobes. The main beam of the antenna was pointing along the Earth's magnetic field line. The strong power peaks above the noise level are due to the clutter from mountains. Spectrum analysis of these clutter echoes proved that these contaminating signals have a very narrow bandwidth and can be removed by suitable procedures. This will allow proper observations at altitudes below 150 km down to the lower D-region. These tasks to implement suitable digital filter procedures remained to be completed.

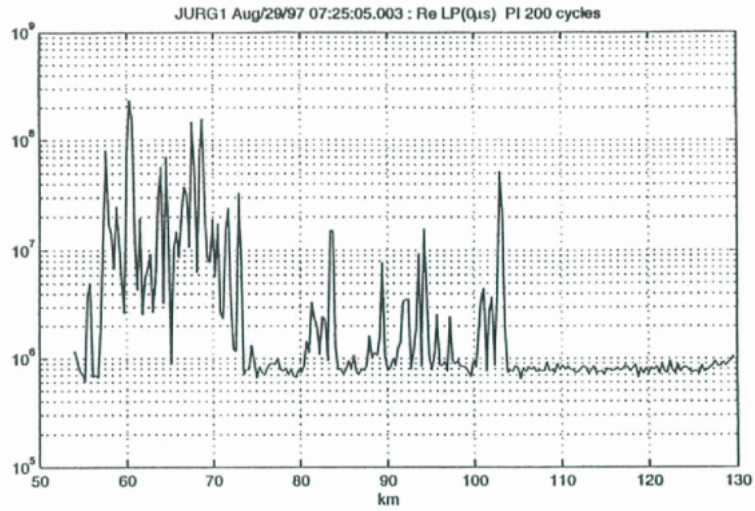

Figure 8: A typical ground clutter profile of the ESR

In parallel to the operations of the ESR the mainland sites of EISCAT in Kiruna, Sodankylä and Tromsø continued their operations in a reasonably reliable mode. Faults, such as computer break downs, wave-guide, coaxial cable, rotary joint, antenna feed and some UHF radar klystron problems, power supply malfunctions, cryogenics failures, antenna servo-loop problems, etc., occurred just due to the ageing of this equipment. The staff was able to quickly localise the faults and do the instant repair such that no real loss in operating time occurred. The VHF klystrons, both carrying around 7000 hours of operation, do not show signs of ageing and work reliably up to 2 MW peak power level. The repaired UHF klystron, however, suffered from arc marks on an outer ceramic ring, which limited the high voltage and consequently the output power. This repaired klystron was used over 3000 hours and the other one about 12000 hours. All time and frequency standards at the KST and ESR sites are now GPS controlled. The inter-site communication via the Internet between Kiruna, Sodankylä and Tromsø has established itself as fully reliable.

The following operating hours were achieved with the KST and ESR systems:

1996	Common Programmes:	686
	Special Programmes	826
	Heating	103
1997	Common Programmes	745
	Special Programmes	889
	Heating	192

A detailed break-up of the Common Programmes, and of the Special Programmes into the contingent of the Associates and third parties is given on page 23 of this Annual Report. That list also contains information about the analysed common programme data as well as a summary of the data archiving. The latter included copying from old magnetic tapes (back to the earlier EISCAT operations in 1984) to DAT and Exabyte tapes and was almost completed by the end of 1997.

The Heating facility was used very efficiently in several campaigns with multinational participation. A power savings modification of the transmitters was implemented and a peak power meter installed to avoid excess power consumption, which could occur when the diagnostics of the VHF and UHF radars are simultaneously operated with the Heating transmitters. A Heating training course and a Heating workshop were held. The Dynasonde again proved a most useful supplement to many experiments.

Executive and Budget meetings were held regularly with the Site Leaders, Executive Assistant and Deputy Directors. The overall administration of EISCAT is under proper control at Headquarters in Kiruna. On 1 July 1996 the personnel of Tromsø and Svalbard were taken over by the University of Tromsø, based on a new contract with EISCAT. The Sodankylä personnel were taken over by the University of Oulu on 1 August 1997. The Kiruna site personnel of EISCAT remain employed by the Swedish Institute of Space Physics (IRF), and EISCAT Headquarters remains an individually administered entity.

A few of the staff spent part of their time at the Tromsø or the Svalbard radar sites to support the extended experimental operations. I would like to thank those persons, who worked full or part time for EISCAT, mostly for the ESR project, and left the Association during the two years 1996-1997. These were: Ann Christine Aittamaa, Pierre Louis Blelly, Carmen Kroll, Tom Grydeland, Stefan Heck, Andre Helvig, Reinhard Hund, Ingela Kyrö, Misha Savitski, and Mikael Snällfot. The engineer Knut Koskkenniemi retired after twenty years of experienced service at the EISCAT Kiruna site. In August 1997 Lasse Olsen joined the Tromsø site as an apprentice. Thanks are also expressed to many staff members, who did the preparations for the hardware and software to allow the inclusion of the graphics and figures in this final report.

In summary I would like to remark that the EISCAT systems in Kiruna, Sodankylä, Tromsø and on Svalbard are in good operational shape, taking into account their different generations. The naturally foreseen fine-tuning and expansion of the new EISCAT Svalbard Radar continues. The scientific operations were well appreciated as conferences and the number of published papers (see graphics on page 16) confirm, and as it was also highlighted during the 8th International EISCAT Workshop held at the University of Leicester, UK, in June 1997.

The Headquarters administration functions efficiently and the final accounts in the years 1996 and 1997 were balanced. The evolution of the ESR, namely the increase in transmitter power and the start of the second antenna project, was brought on its way. Proposals for the evolution to replace instrumentation in Kiruna, Sodankylä and Tromsø, which was bought in the early 1980s or before, were specified as required. Financial resources were allocated and saved for this purpose, but man-power had been lacking to start this evolution at an earlier instance.

As this is my final Director's report I would like to express my thanks and recognition to the Council for its guidance and control during my term as Director of EISCAT. It was a challenging time for me. Some particular assignments and engagements, out of very many, I will particularly recollect and not forget: First to get the VHF radar in Tromsø into reliable operation and assure proper experiment performance, and thereafter the demanding EISCAT Svalbard Radar project, including the realisation of Japan joining the EISCAT Scientific Association.

The performance of all my tasks would not have been possible without the intense contributions and the potent collaboration of the staff of EISCAT. I owe my deep appreciation and sincere acknowledgement to many individuals, as well as the Council, the Committees and the EISCAT Associates. I have made many good friends during my time with EISCAT, with whom I wish to continue a pleasant friendship and healthy communication in the years to come. In particular I will miss the pleasant collaboration with the staff at Headquarters in Kiruna.

Figure 9: The staff of EISCAT Headquarters in November 1997 (from left to right): Eva Tartu, Henrik Andersson, Jürgen Röttger, Ingvar Keskitalo, Anette Snällfot, Olli Vertanen, Carmen Kroll, Gunnar Isberg, Gudmund Wannberg and Peter Collis.

The EISCAT Scientific Association has gained world-wide recognition and its operation has contributed to increase our knowledge of ionospheric, magnetospheric, plasma and atmospheric physics. The design of modern instruments, signal modulation and processing techniques has further contributed to raise the standard of research using the incoherent scatter radar technique. The statistics of papers published in well-known journals, books and magazines, which is found on a following page, proves this development.

My thanks are also addressed to the Council, the Scientific Advisory Committee, the Administrative and Finance Committee and particularly to all the EISCAT staff for the special farewell celebrations done on the occasion of the completion of my affiliation as EISCAT Director.

It is my sincere desire that the standard of EISCAT, built up over the years, can continue and I wish the Association and my successor Dr. Tauno Turunen a successful future.

Jürgen Röttger

44th Meeting of the EISCAT Council on 17/18 November 1997 in Kiruna (from left to right): Lower row: Cesar La Hoz, Birgit Benterud, Jürgen Röttger, Tauno Turunen, Wlodek Kofman, Tor Hagfors. Centre row: Graham Brooks, Asgeir Brekke, Takeo Hirasawa, John Gustavsson, Denis Alcaydé, Hermann Opgenoorth, Henrik Andersson. Upper row: Gudmund Wannberg, Susumo Kokubun, Ryochi Fujii, Jorma Kangas, Tudor Jones, Michael Lockwood, Tony van Eyken.

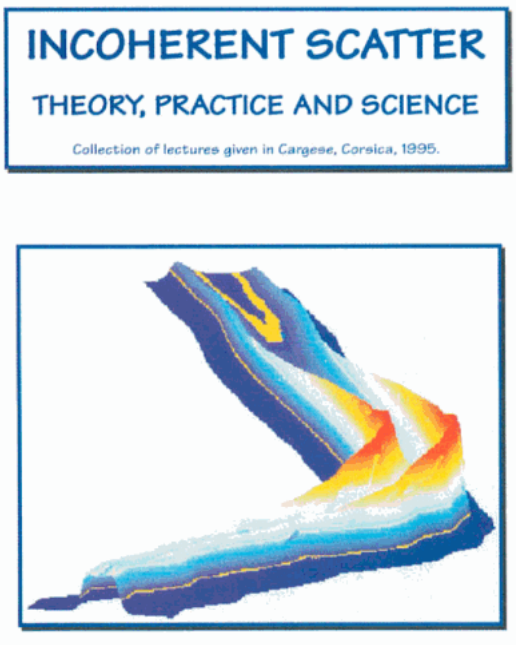

Denis Alcaydé - Editor

Technical Report 97/53
EISCAT Scientific Association

Table of Contents

Table of Contents	i
Author's Vademecum	iii
Editor's Foreword	v
Acknowledgements	vi
Tor Hagfors Plasma Fluctuations Excited by Charged Particle Motion and their Detection by Weak Scattering of Radio Waves	1
Wlodek Kofman Plasma Instabilities and their Observations with the Incoherent Scatter Technique	33
Asko Huuskonen and Markku Lehtinen Modulation of Radiowaves for Sounding the Ionosphere: Theory and Applications	67
Kristian Schlegel The Use of Incoherent Scatter Data in Ionospheric and Plasma Research	89
Mike Lockwood Solar Wind - Magnetosphere Coupling	121
Yoshuke Kamide Aurora/Substorm Studies with Incoherent-Scatter Radars	187
Arthur D. Richmond Ionosphere-Thermosphere Interactions at High Latitudes	227
Jürgen Röttger Radar Observations of the Middle and Lower Atmosphere	263

An EISCAT Technical Report 97/53 was published end of 1997, containing lectures given at the International EISCAT School, which was held in Cargese, Corsica, in fall 1995. Copies of this book are available through EISCAT Headquarters

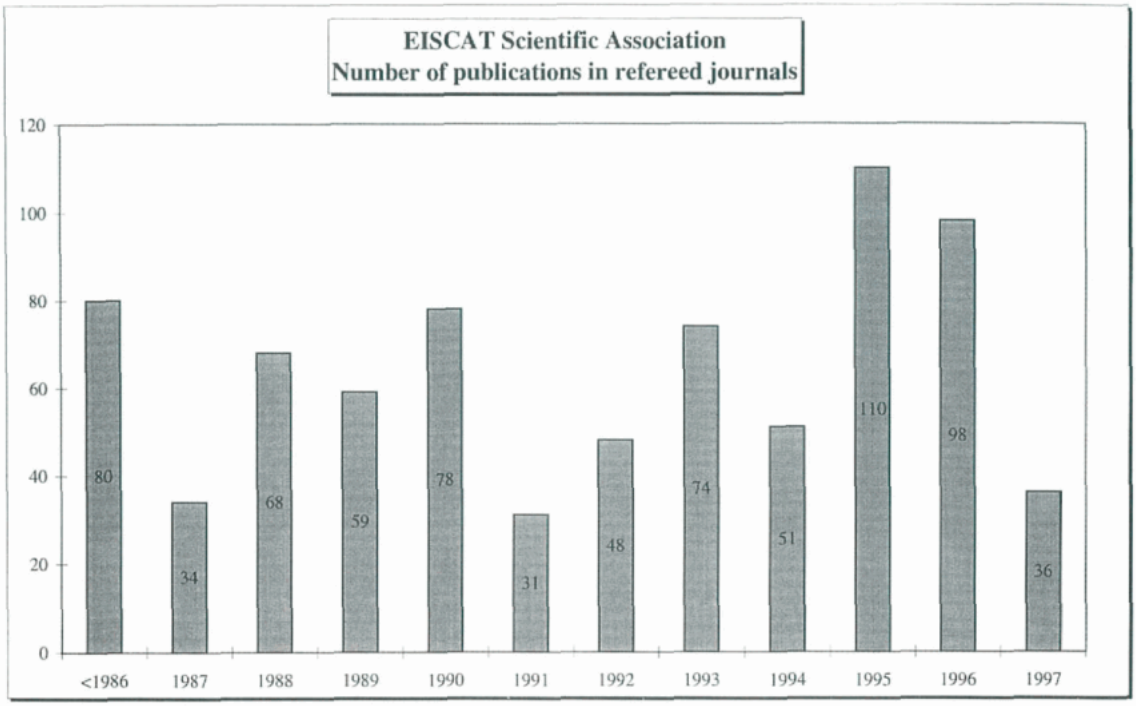

The number of papers published in refereed journals, which deal with EISCAT science.
In the period 1986-1997 the total number of publications accumulated to 767.

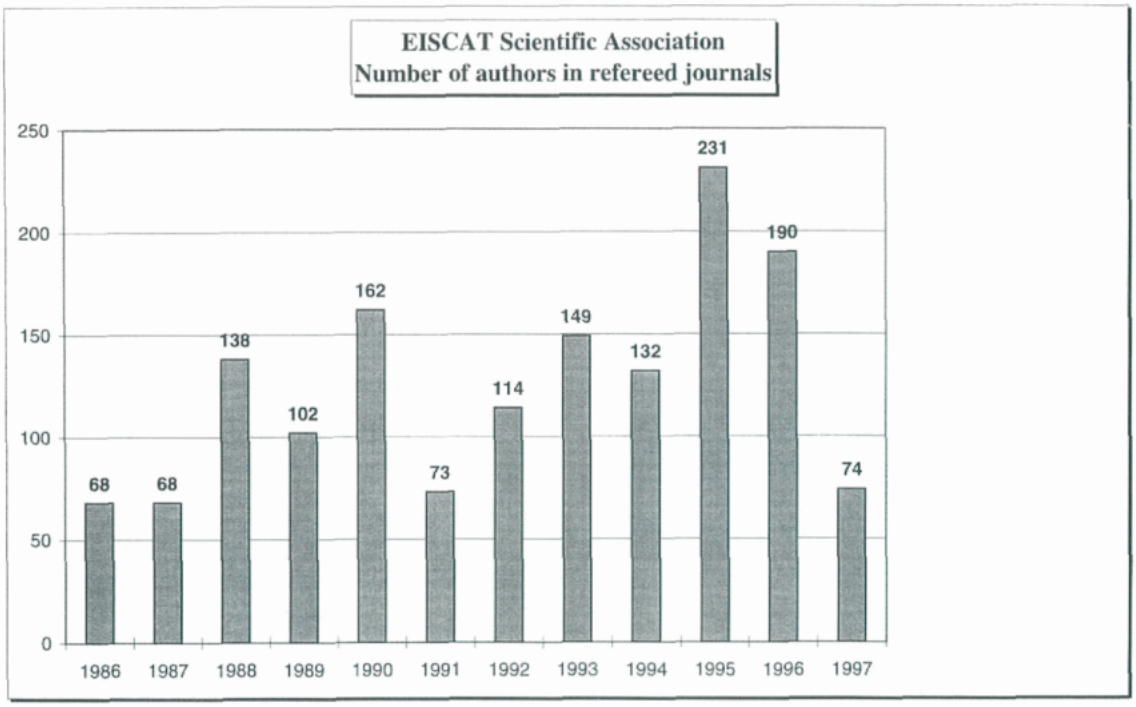

The number of authors on papers published in refereed journals
The total number of individual authors was 609.

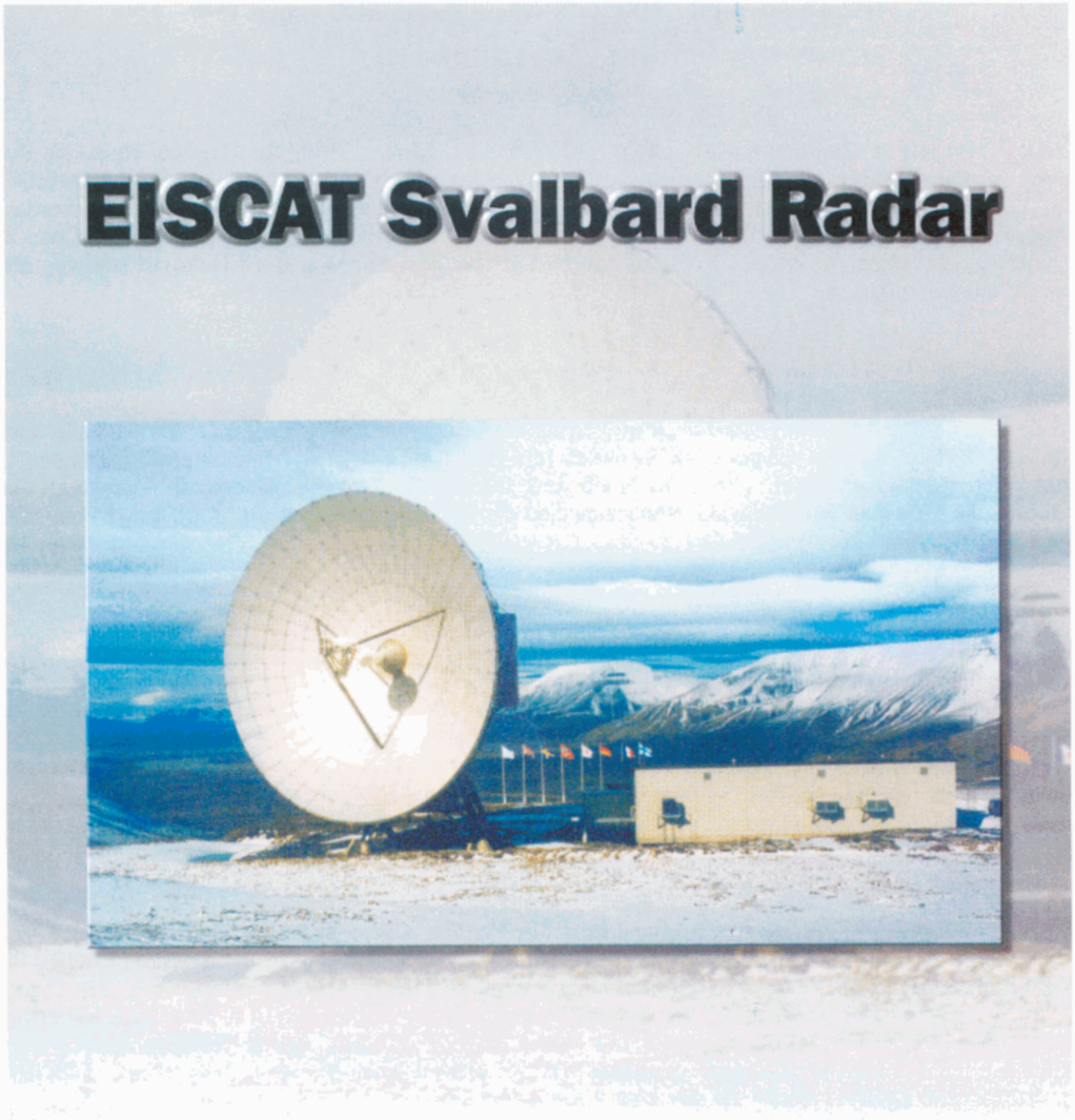

The evolutionary step into EISCAT´s future

The cover page of the EISCAT Svalbard Radar leaflet, which was published in spring 1997. It shows the EISCAT Svalbard Radar site on the day of its inauguration on 22 August 1996.
This leaflet was preceded by a new edition of a 24-page EISCAT brochure, which was published on the occasion of the inauguration of the EISCAT Svalbard Radar.

Inauguration of the EISCAT Svalbard Radar on 22 August 1996

Photos page 19

Photos from left to right and top to bottom: The Council Chairman, Prof. Tor Hagfors, observing the arrival of the charter plane; which brought 125 participants from Oslo to Longyearbyen; the Director, Dr. Jürgen Röttger welcoming Prof. Asgeir Brekke, Prof. Antti Siivola and Minister Reidar Sandal; Prof. Matuura; Dr. Ronald Woodman talking to Prof. William Gordon and his wife Elva; the Council Chairman welcoming Dr. Wlodek Kofman; Prof. Bengt Hultqvist and Mrs. Gurli Hultqvist studying the inauguration program.

Photos page 20

Arvid Øvergård and Dr. Tony van Eyken overseeing the inauguration ceremonies; Dr. David Willis and Mr. Jan Hyfödt; the Sysselmannen på Svalbard, Mrs Ann-Kristin Olsen, welcoming the participants; Prof. Bengt Hultqvist, Prof. Henry Rishbeth and Deputy Director Dr. Gudmund Wannberg; the Ambassador of Japan Mr. Tadayuki Nonoyama and Prof. Takeo Hirasawa; Dr. Tony van Eyken and Prof. Phil Williams.

Photos page 21

Minister Reidar Sandal giving the opening speech; Dr. Jürgen Röttger thanking the minister for opening the EISCAT Svalbard Radar; Prof. Tudor Jones addressing the ESR on behalf of the UK; Mr Christian Hambro on behalf of Norway; Prof. Guy Aubert on behalf of France; Dr. Röttger thanking for the addresses and expressing his high appreciation to the EISCAT staff and many others for their dedicated contribution to this project; Prof. William Gordon holding the inauguration speech.

Photos page 22

A project information meeting was held and Prof. Tor Hagfors addressed the participants; a dinner was served at the Svalbard Polar Hotel; Dr. Kari Kveseth donated a scholarship of the Research Council of Norway to EISCAT; Dr. Murray Baron presenting a picture of the Sondreström observatory; Dr. Tauno Turunen congratulating on behalf of the Sodankylä Geophysical Observatory; Dr. Tove Bull delivering a present of the University in Tromsø; our ladies staff: Eva Tartu, Anette Snällfot, AnnChristin Aittamaa and Carmen Kroll (Ingrid Storhaug was not present when the photo was taken); EISCAT staff relaxing at a private dinner the day after the inauguration.


BRAATHENS SAFE

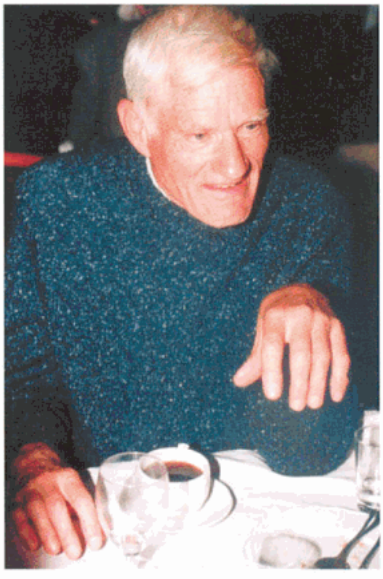


c Association


EISCAT Scientific Association


EISCAT Scien c Ass
Svalb dar
gurati gus


Scientific
lbard R
on 22

EISCAT Operations 1996-1997

Common Programme One, CP-1, uses a fixed transmitting antenna, pointing along the geomagnetic field direction. The three-dimensional velocity and anisotropy in other parameters are measured by means of the receiving stations at Kiruna and Sodankylä (see map, inside front cover). CP-1 is capable of providing results with very good time resolution and is suitable for the study of substorm phenomena, particularly auroral processes where conditions might change rapidly. The basic time resolution is 5 sec. Continuous electric field measurements are derived from the tristatic F-region data. On longer time scales, CP-1 measurements support studies of diurnal changes, such as atmospheric tides, as well as seasonal and solar-cycle variations. The present scheme uses alternating codes and long pulses for ACF measurements, as well as short pulses for power profiles.

Common Programme Two, CP-2, is designed to make measurements from a small, rapid transmitter antenna scan. One aim is to identify wave-like phenomena with length and time scales comparable with, or larger than, the scan (a few tens of km and about ten minutes). The present version consists of a four-position scan which is completed in six minutes. The first three positions form a triangle with vertical, south and south-east positions, while the fourth is aligned with the geomagnetic field. The remote site antennas provide three-dimensional velocity measurements in the F-region. The pulse scheme is identical with that of CP-1.

Common Programme Three, CP-3, covers a 10° latitudinal range in the F-region with a 17-position scan up to 74°N in a 30 minute cycle. The observations are made in a plane defined by the magnetic meridian through Tromsø, with the remote site antennas making continuous measurements at 275 km altitude. A power profile and long pulse ACFs are measured. The principle aim of CP-3 is the mapping of ionospheric and electrodynamic parameters over a broad latitude range.

Common Programmes One, Two and Three are run on the UHF radar. Three further programmes are designed for use with the VHF system. The UHF and VHF radars were often operated simultaneously during the CP experiments in 1994 and 1995. Such observations offer comprehensive data sets for atmospheric, ionospheric and magnetospheric studies.

Common Programme Four, CP-4, covers geographic latitudes up to almost 80°N (77°N invariant latitude) using a low elevation, split-beam configuration. CP-4 is particularly suitable for studies of high latitude plasma convection and polar cap phenomena.

Common Programme Six, CP-6, is designed for low altitude studies, providing spectral measurements at mesospheric heights. Velocity and electron density are derived from the measurements and the spectra contain information on the aeronomy of the mesosphere. Vertical antenna pointing is normally used.

Common Programme Seven, CP-7, probes high altitudes and is particularly aimed at polar wind studies. The present version uses both of the VHF klystrons and is designed to cover altitudes up to 2500 km vertically above Ramfjordmoen.

Common Programme modes are being developed for the EISCAT Svalbard Radar and prototype equivalents of CP-1, CP-2, CP-3 and CP-4 have been operated in conjunction with the corresponding modes on the mainland. All modes use a common pulse scheme using four long pulses to cover approximately 80 to 900km in range. Data below 150km range are contaminated by ground clutter. CP-1L is directed along the geomagnetic field (81.6° inclination). CP-2L uses a four position scan with spacing matching CP-2. CP-3L is a 30 position elevation scan with southerly beam swinging positions overlapping those of CP-3. CP4-L combines observations in the F-region viewing area of the two beams of CP-4 with field-aligned and vertical measurements.

The following table provides an overview of EISCAT Common Programme experiments in 1996 and 1997. ESR operations are only tabulated where a substantial continuous data set exists. WD indicates a co-ordinated 'World Day' incoherent scatter experiment, * indicates multiple radar operation for some or all of the interval.

The remaining tables show the accounted hours on the various facilities for each month and for each Common Programme mode (CP's) or Associate (SP's).

UHF Common Programmes during 1996

96-01-22 09UT 01-24 09UT CP-3-G WD
96-02-13 10UT 02-14 16UT CP-1-K WD
96-03-19 10UT 03-22 16UT CP-2-E WD
96-06-17 08UT 06-19 16UT CP-1-K WD
96-07-16 10UT 07-17 16UT CP-2-E WD
96-08-13 10UT 08-14 16UT CP-3-F WD
96-10-08 14UT 10-12 22UT CP-2-E WD *
96-11-14 16UT 11-15 16UT CP-1-K *
96-11-16 06UT 11-16 09UT CP-1-K *
96-11-17 18UT 11-17 22UT CP-1-K *
96-11-18 21UT 11-19 01UT CP-1-K *
96-11-21 20UT 11-21 24UT CP-1-K *
96-11-22 20UT 11-22 24UT CP-1-K
96-12-09 04UT 12-09 09UT CP-1-K
96-12-10 10UT 12-11 14UT CP-1-K WD

VHF Common Programmes during 1996

96-05-14 11UT 05-15 16UT CP-4-B WD
96-09-17 12UT 09-18 16UT CP-4-B WD
96-09-24 14UT 09-26 15UT CP-6-B
96-09-28 10UT 09-29 16UT CP-4-B *
96-11-06 16UT 11-07 08UT CP-4-B
96-11-14 17UT 11-15 16UT CP-7-F *
96-11-16 05UT 11-16 09UT CP-7-F *
96-11-17 18UT 11-17 22UT CP-7-F *
96-11-18 21UT 11-19 01UT CP-7-F *
96-11-21 16UT 11-21 24UT CP-7-F *
96-12-17 11UT 12-18 10UT CP-6-B

ESR Common Programmes during 1996

96-09-28 07UT 09-28 21UT CP-1L WD
96-09-29 06UT 09-29 19UT CP-1L WD *
96-10-10 06UT 10-10 15UT CP-1L WD *
96-11-15 00UT 11-15 08UT CP-1L WD *

UHF Common Programmes during 1997

97-01-01 16UT 01-02 08UT CP-1-K
97-01-06 11UT 01-10 16UT CP-2-E WD
97-02-10 13UT 02-12 16UT CP-1-K
97-03-11 10UT 03-12 16UT CP-2-E WD *
97-04-08 15UT 04-09 14UT CP-3-F WD *
97-04-09 14UT 04-10 22UT CP-1-K WD *
97-05-14 14UT 05-15 22UT CP-1-K *
97-06-23 10UT 06-27 16UT CP-1-K WD
97-09-02 10UT 09-03 16UT CP-3-F WD *
97-10-21 10UT 10-23 20UT CP-2-E WD *
97-12-02 15UT 12-04 08UT CP-2-E WD *

VHF Common Programmes during 1997

97-03-11 09UT 03-12 16UT CP-4-B WD *
97-05-14 14UT 05-15 22UT CP-6-B *
97-06-03 11UT 06-06 16UT CP-7-F WD *
97-08-13 10UT 08-14 16UT CP-6-B
97-08-27 22UT 08-29 06UT CP-4-B *
97-11-04 09UT 11-05 16UT CP-6-B WD *
97-12-09 10UT 12-10 16UT CP-6-B

ESR Common Programs during 1997

97-02-17 22UT 02-19 02UT CP-1L
97-03-11 09UT 03-12 16UT CP-1L WD *
97-03-14 16UT 03-15 04UT CP-1L
97-04-08 11UT 04-10 16UT CP-1L WD *
97-04-25 07UT 04-25 21UT CP-1L
97-05-09 06UT 05-09 14UT CP-1L
97-05-15 08UT 05-15 23UT CP-1L *
97-06-03 12UT 06-06 18UT CP-1L WD *
97-08-27 21UT 08-29 07UT CP-4L *
97-09-02 16UT 09-03 14UT CP-3L WD *
97-10-22 14UT 10-23 20UT CP-2L WD *
97-11-04 10UT 11-05 24UT CP-1L WD *
97-11-07 09UT 11-07 20UT CP-2L

TOTAL OPERATING HOURS 1996

1996	Jan	Feb	Mar	Apr	May	Jun	Jul	Aug	Sep	Oct	Nov	Dec	Total
UHF	54	177	110	41		56	29	61		148	173	98	**947**
VHF	5	54	45		29	16	31	6	106	24	198	53	**567**
Dual	5	49	22	31				6			133	35	**281**
Passive				180	52	5		10	18				**265**
Heating			5		33			12	1		32	20	**103**
ESR				10				19	3	27	8	13	**80**

TOTAL OPERATING HOURS 1997

1997	Jan	Feb	Mar	Apr	May	Jun	Jul	Aug	Sep	Oct	Nov	Dec	Total
UHF	159	112	88	165	32	129	75	1	31	104	129	44	**1069**
VHF			81	89	32	91	41	97		16	72	35	**554**
Dual			81	25	32	13	18	1		13	33	5	**221**
Passive			16	11	31	26	4	5	27				**120**
Heating		8	10	39		8		35	13	22	57		**192**
ESR	5	28	41	74	23	78	40	36	22	30	75	37	**489**

COMMON PROGRAMMES (UHF and VHF) 1996

1996	Jan	Feb	Mar	Apr	May	Jun	Jul	Aug	Sep	Oct	Nov	Dec	Total	%
CP1		30				56					39	28	153	22
CP2			78				29			104			211	31
CP3	49							27					76	11
CP4					29				58		8		95	14
CP6									47	8		24	79	12
CP7											72		72	10
Total	49	30	78	0	29	56	29	27	105	112	119	52	**686**	100%
%	7	4	11	0	4	8	4	4	15	16	17	8	100%	

SPECIAL PROGRAMMES (UHF and VHF) 1996

1996	Jan	Feb	Mar	Apr	May	Jun	Jul	Aug	Sep	Oct	Nov	Dec	Total	%
3rdP		2									14		16	2
EI		5		17			7			8			37	4
FI										37	16	1	54	7
FR		24	57							2	92	4	179	22
GE		30		20			18	1		25	17	55	166	20
NI							2			1	22	17	42	5
NO		15					16	9		9	2	7	58	7
SW	8					16				2	26	2	54	7
UK		88	10	56	13	5		30	4	10	4		220	27
Total	8	164	67	93	13	21	43	40	4	94	193	86	**826**	100%
%	1	20	8	11	2	3	5	5	0	11	23	10	100%	

COMMON PROGRAMMES (ESR) 1996

1996	Jan	Feb	Mar	Apr	May	Jun	Jul	Aug	Sep	Oct	Nov	Dec	Total	%
CP1L			10				19	3	27	8	13		80	100
CP2L													0	0
CP3L													0	0
CP4L													0	0
Total	0	0	10	0	0	0	19	3	27	8	13	0	**80**	100%
%	0	0	13	0	0	0	24	4	34	10	16	0	100%	

There were no Special Programme operations on the ESR in 1996.

COMMON PROGRAMMES (UHF and VHF) 1997

1997	Jan	Feb	Mar	Apr	May	Jun	Jul	Aug	Sep	Oct	Nov	Dec	Total	%
CP1	15	51		36	16	102							220	30
CP2	99		14							58		39	210	28
CP3				20					31				51	7
CP4			28					32					60	8
CP6					32			33			31	30	126	17
CP7						78							78	10
Total	114	51	42	56	48	180	0	65	31	58	31	69	**745**	100%
%	15	7	6	8	6	24	0	9	4	8	4	9	100%	

SPECIAL PROGRAMMES (UHF and VHF) 1997

1997	Jan	Feb	Mar	Apr	May	Jun	Jul	Aug	Sep	Oct	Nov	Dec	Total	%
3rdP											15		15	2
EI				10		6				12	3		31	3
FI	15		2			6		4	1	2	14		44	5
FR	10	13		111			35			8	18		195	22
GE	4	22	6	14	2	2	4	31	11	16	43	6	161	18
NI	2	7	10				50						69	8
NO	1	6	12	10						6	32		67	8
SW	7	10	14				18	25		5	47		126	14
UK	4	13	45	51	5	30	1	1	4	19	5	3	181	20
Total	43	71	89	196	7	44	108	61	16	68	177	9	**889**	100%
%	5	8	10	22	1	5	12	7	2	8	20	1	100%	

COMMON PROGRAMMES (ESR) 1997

1997	Jan	Feb	Mar	Apr	May	Jun	Jul	Aug	Sep	Oct	Nov	Dec	Total	%
CP1L	5	28	41	74	23	78					31	9	320	83
CP2L								3		30	11		44	11
CP3L									21				21	5
CP4L								31					0	0
Total	5	28	41	74	23	78	0	34	21	30	42	9	**385**	100%
%	1	7	11	19	6	20	0	9	5	8	11	2	100%	

SPECIAL PROGRAMMES (ESR) 1997

1997	Jan	Feb	Mar	Apr	May	Jun	Jul	Aug	Sep	Oct	Nov	Dec	Total	%
3rdP													0	0
EI													0	0
FI													0	0
FR							13						13	13
GE								2	1		13	19	35	34
NI							14						14	13
NO											14		14	13
SW													0	0
UK							13				6	9	28	27
Total	0	0	0	0	0	0	40	2	1	0	33	28	**104**	100%
%	0	0	0	0	0	0	38	2	1	0	32	27	100%	

Scientific Research and Developments

Geomagnetic pulsations and ULF waves

ULF pulsations are oscillations of the magnetic field with periods lasting from seconds to minutes. When observed from the ground, they appear to originate from currents in the ionosphere. These currents are in turn induced by processes in the Earth's magnetosphere. Measurements by satellites at geostationary orbits have revealed that the ring current is an important source of such magnetic pulsations. This electric current flows around the Earth in the equatorial plane at about 4-6 Earth radii distance from the ground. It is carried by particles that are trapped in the geomagnetic field. The current can become unstable and modulate itself. This mechanism also "untraps" electrons and scatters them into a region in the velocity space called the loss cone. Electrons in the loss cone reach the Earth's atmosphere while they are moving along the geomagnetic field line. There they collide with neutral particles, causing ionisation.

Simultaneously magnetic pulsations are seen with IMAGE. The pulsations are partly caused by waves, which are probably also emitted by the unstable ring current, and partly due to the varying conductivity of the ionosphere. In the latter case the ionosphere acts like a transistor modulating the auroral electrojet. Figure 10 shows the ground magnetic field, the electric field, and the height-integrated Hall conductivity Σ_H. One can see that Σ_H is anti-correlated with the electric field, suggesting, that the ionospheric conductivity gradients cause polarisations. Although Σ_H varies strongly, by a factor around two, the ground magnetic field responds more to the electric field (Buchert, Fujii, and Glassmeier).

Since the middle of 1995, an HF Doppler sounder has been running almost continuously in northern Norway. The Doppler Pulsation Experiment (DOPE), which consists of a receiver at Ramfjordmoen and a transmitter at Seljelvnes, facilitates high spatial and temporal resolution

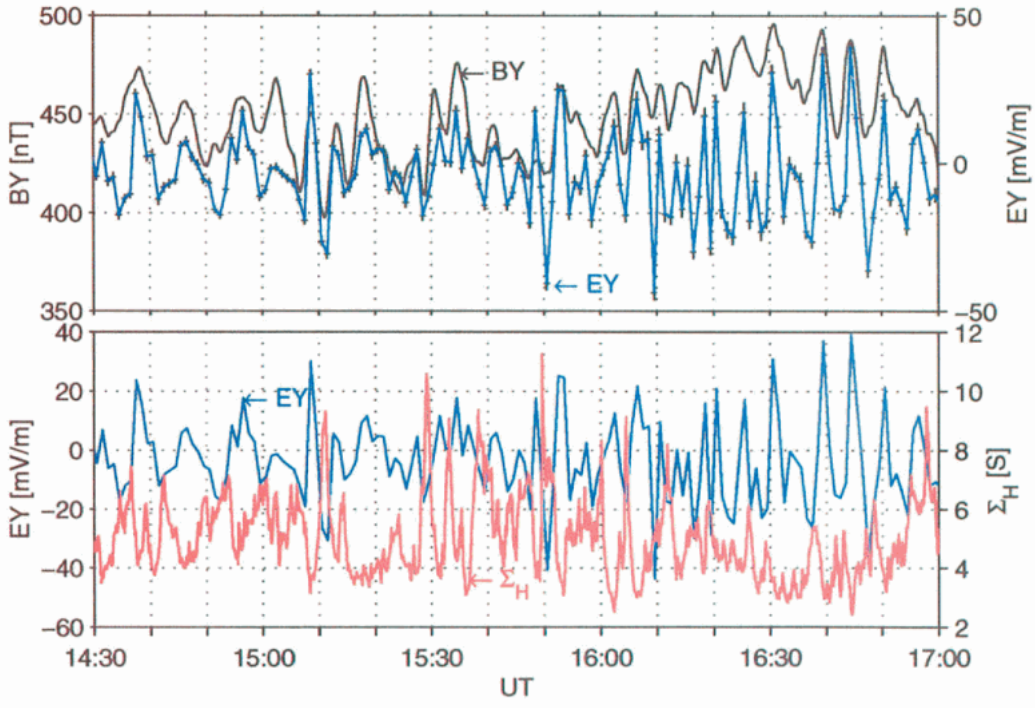

Figure 10: Time series of the east-west (Y) geomagnetic field (black curve), the electric field (blue curve), and the height-integrated Hall conductivity (red curve) on October 18, 1993.

The effects of such "pulsating" (oscillatory) electron precipitation into the ionosphere can now be seen with the help of the UHF radar and the IMAGE magnetometer array. Collisional ionisation increases the charge carrier density and conductivity in the E-region quasi-periodically. observations of the ionospheric signatures of ULF waves at high latitudes. Simultaneous operation of the EISCAT UHF radar in CP-1 mode has made it possible to study the ionospheric signature of a magnetospheric ULF wave. These are the first results of such wave signatures

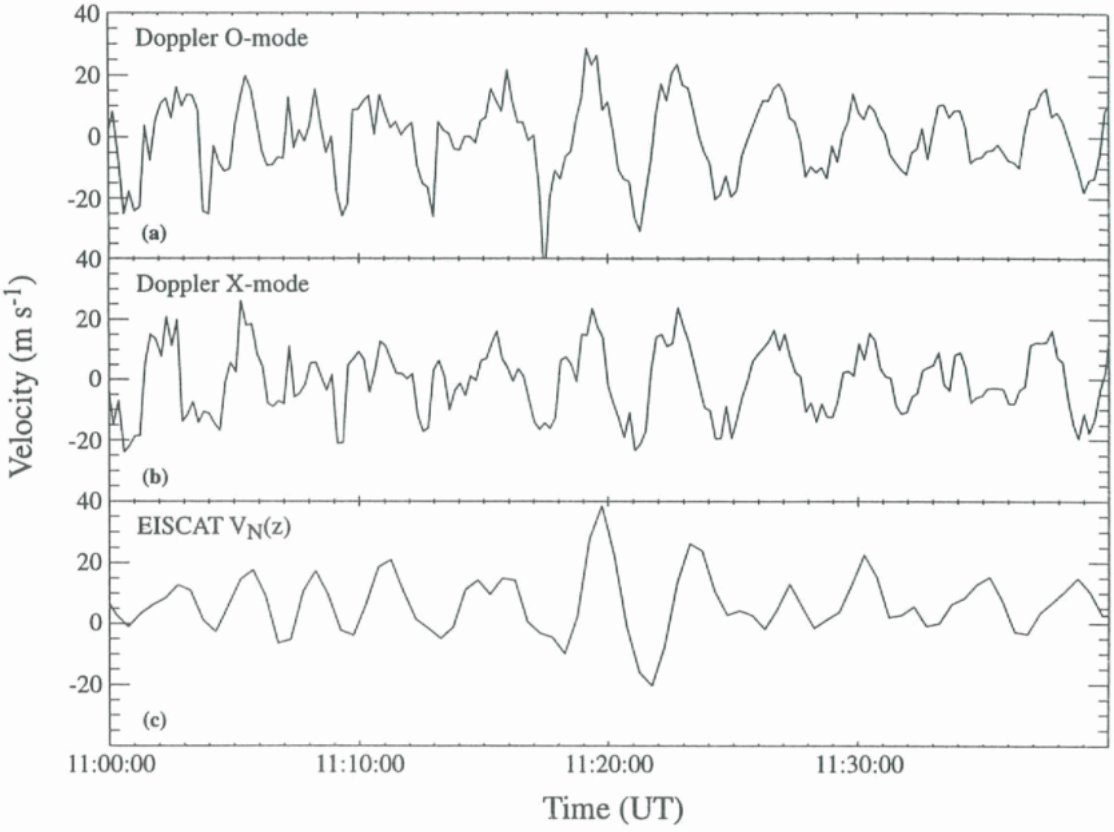

Figure 11: Velocities derived from DOPE (a) O-mode and (b) X-mode signals and (c) the vertical component of the northward field-perpendicular velocity measured by EISCAT for the interval 11:00-11:40 UT on 13th February 1996. Data have been filtered to exclude periods outside the range 30-400 s (a, b) and 120-400 s. In each case the ordinate axes display relative scales.

observed simultaneously in both instruments. Figure 11 demonstrates that the observed Doppler signature was mainly due to the vertical bulk motion of the ionosphere caused by the electric field perturbation of the ULF wave, thus achieving the first direct observational confirmation of a numerical simulation. The wave, which was Alfvénic in nature, was detected by the instruments eight degrees equatorward of the broad resonance region. The implications for the deduced wave modes in the ionosphere and the mechanism producing the HF Doppler variations have been evaluated (Wright et al., 1997).

Mesosphere and D-Region

A major new addition to the instruments available to support EISCAT observations of hard particle precipitation has been the IRIS imaging riometer facility, which has been carrying out continuous observations of cosmic noise absorption in a region surrounding EISCAT since its inception in 1994. The range of topics which can be investigated by joint use of IRIS and EISCAT has been reviewed. Most of the effort in comparative studies has been directed into four case studies of energetic precipitation events. These have each produced new scientific results and illustrated new possibilities for combining data from the two systems. Particular use was made of the technique of inverting observed electron density profiles to precipitating particle fluxes (Collis and Hargreaves, 1997).

In daylight conditions on May 4, 1995, the spatial distribution and dynamics of the radio absorption showed a morphology similar to that of visible aurora at substorm onset, including spectral hardening. The VHF radar was pointed vertically, with the UHF tilted to intersect the D-region above Kilpisjarvi. The data from the two beams, separated by about 80 km in the D-region, showed some similarities, but also some differences, see Figure 12. The IRIS data allowed the EISCAT observations to be set in a proper spatial context with respect to the dynamical changes in the particle precipitation. These results gave further impetus to the need to combine IRIS and optical observations, ideally in combination with EISCAT data (Collis and Hargreaves, 1997).

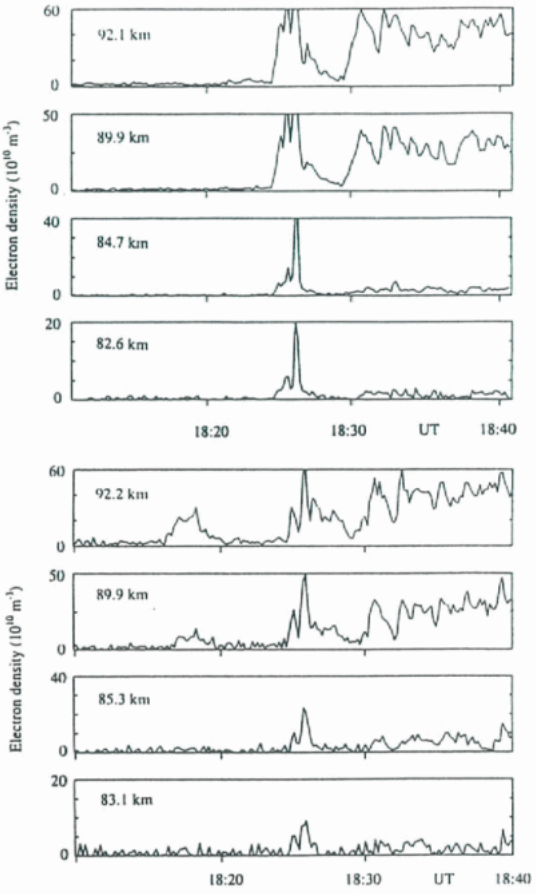

Figure 12: Time series of EISCAT VHF data from the May 4th 1995 sharp onset event (upper panel). The VHF antenna was pointed vertically. Lower panel as above but for the EISCAT UHF radar. The altitudes differ slightly from because of the geometry. The radar was pointing at an elevation of 46.8° and azimuth 135°.

An isolated region of energetic electron precipitation observed near local noon on March 1, 1995 was investigated using IRIS and EISCAT. IRIS revealed that the absorption event was essentially co-rotating with the Earth for about two hours. The spatial and temporal variations in the D-region electron density seen by EISCAT were interpreted in a consistent way when compared with the IRIS data. EISCAT detected significant increases in electron density at altitudes as low as 65 km as the event drifted through the radar beam. The altitude distribution of incremental radio absorption revealed that more than half of the absorption occurred below 75 km, with a maximum at 67 km. The energy spectrum of the precipitating electrons was very uniform throughout the event, and could be described analytically by the sum of three exponential distributions with characteristic energies of 6, 70 and 250 keV, Figure 13. A profile of effective recombination coefficient that resulted in self-consistent agreement between observed electron densities and those inferred from an inversion procedure was deduced. The observations suggest a co-rotating magnetospheric source region on closed day-side field lines. However, a mechanism is required that can sustain such hard precipitation for the relatively long duration of the event (Collis et al, 1996).

By itself, EISCAT furnishes spot measurements of the energy input within the radar beam. Broader-scale estimates require information on

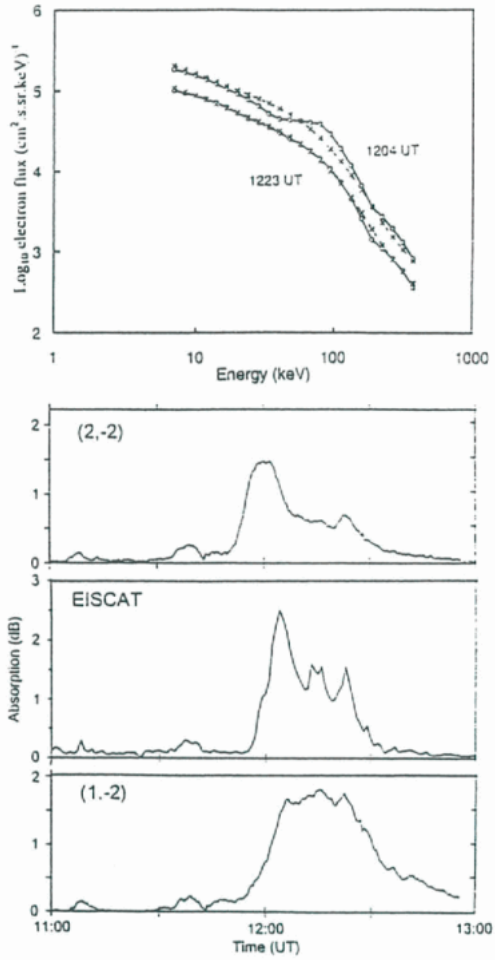

Figure 13: Upper panel: Electron energy spectra inferred from EISCAT D-region electron density profiles. Full lines with circles correspond to spectra fitted to two measured profiles with the photo-ionisation removed (i.e. precipitation only). Analytical fits corresponding to a three-component distribution are shown by broken lines with crosses. Lower Panel: Radio absorption measured by four IRIS beams at the longitude of EISCAT. The separation between the beams is about 30 km in the N-S direction at 90 km altitude

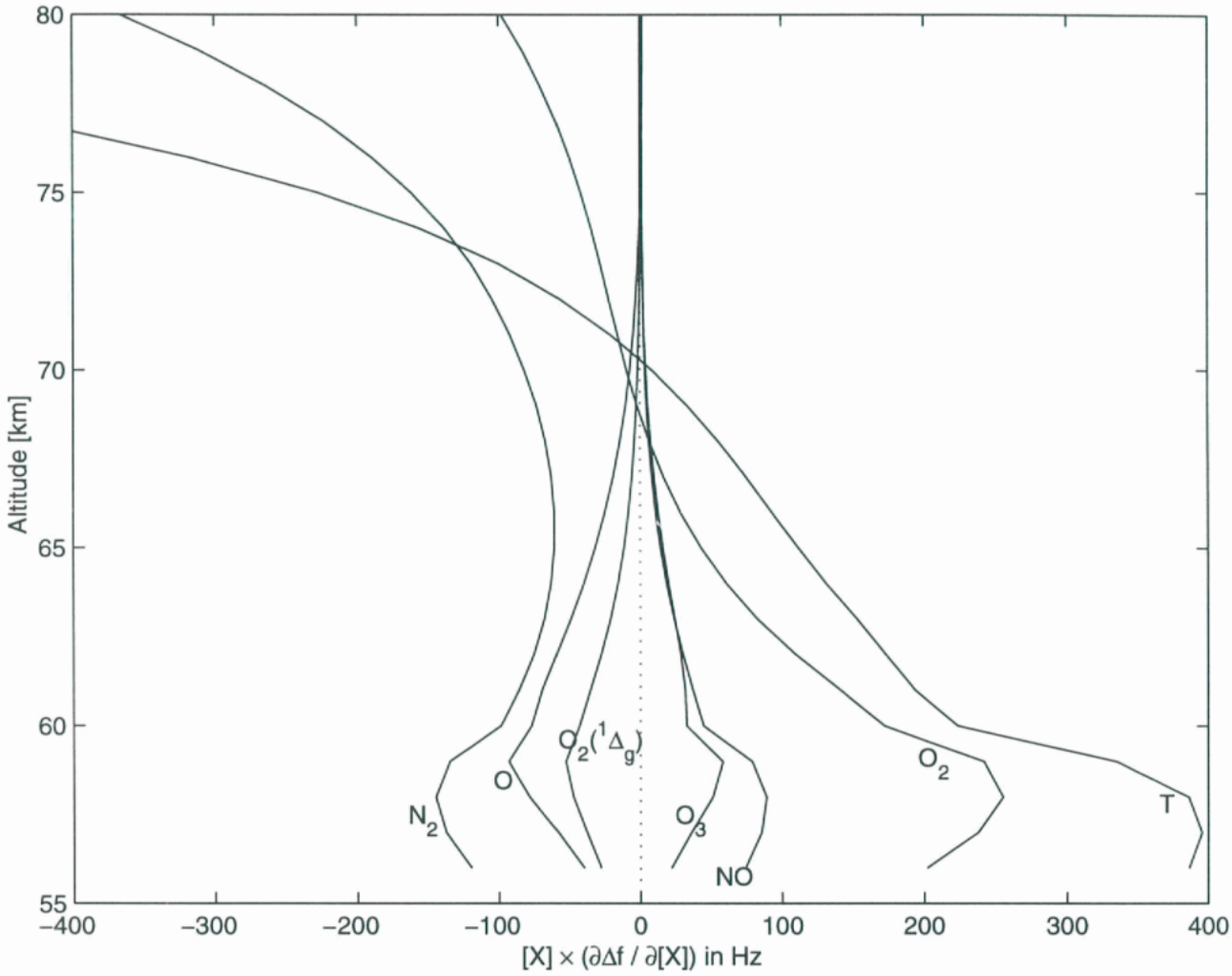

Figure 14: Effect of concentrations of various neutral constituents and temperature on spectral width

the spatial extent and lifetimes of the precipitation features, which is provided by IRIS. The daytime event occurring on May 31 1995 was rather weak. Although the radar detected this feature for about 10 minutes, the IRIS observations revealed that it was actually a long-lived, slowly equatorward-moving patch that drifted through the radar beam. More accurately, the precipitation showed co-rotating characteristics similar to those reported in the example above. With the assumption that the particle spectrum did not change significantly with time, which seems a reasonable inference based on the observations, the IRIS data could be readily converted into space-time maps of energy input for this event. Preliminary estimates for the main precipitation region were of order 106 Js^{-1}.

The night-time substorm onset was very different from the daytime event. The precipitation expanded rapidly polewards across the IRIS field-of-view and showed very dynamic changes on time scales of a few seconds with very localised structure. The most intense absorption was slightly east of EISCAT, so the measured electron densities underestimated the maximum energy input. Knowing the absorption recorded by the IRIS beam closest to EISCAT, it was possible to estimate the maximum energy deposition by simply scaling the observed electron densities by the ratio of the two absorption measurements (implicitly assuming that the electron energy spectrum was the same). In this case the ratio was about five, implying electron densities at the maximum some five times larger than observed by EISCAT. The implied peak energy was of order 108 Js^{-1}, which is considerably more than for the daytime event described above. The integral effects over event lifetimes are comparable because of the persistence of the daytime event (Collis et al, 1997).

A study of the above event is underway using data from all-sky TV, IRIS and EISCAT. For the first time, the positions of the 49 IRIS beams have been accurately mapped onto the all-sky TV image, so that the auroral light intensity in each

beam can be recorded as a time-series for cross-correlation with the IRIS data. During one experiment, three auroral intensifications occurred in the TV zenith, separated by about 45 minutes each. The first of these did not break up, but the latter two did so. EISCAT showed an electric field enhancement during the first and third event, but not during the second one. The second and third events expanded polewards, passing through the EISCAT beam and allowing examination of the particle spectra. One topic in particular that is being addressed with these data is the co-location, or otherwise, of the visible aurora and the absorption regions. Preliminary results suggest that these are co-located during the pre-break-up phase, but that there is a delay (or spatial displacement) during the poleward expansion phase, with the absorption located in the wake of the visible forms.

Velocities observed by EISCAT UHF in the mesosphere during a strong PCA event 12-15 August 1989 were used to study late summer conditions in this height region. In addition to the EISCAT data, lidar temperatures from the Na lidar at Andenes were used. One of the results was that the dynamic state of the mesosphere appears to change over rather abruptly from the summer state to the winter state, but at high altitudes first. A rather intriguing result is the similarity of the average vertical wind structure in this observation to that observed by EISCAT VHF and by SOUSY in summer 1987: Increasing from 0 to 0.3 ms^{-1} from ~88 km to ~92 km, downward between ~83 km and ~88 km (the major PMSE height region), and increasingly upward below ~83 km (Hansen and Hoppe, 1996)

A detailed re-analysis of D-region EISCAT data during the PCA event of 23 October, 1989 was made by using the 55-ion Sodankylä Geophysical Observatory ion-chemistry model. The EISCAT data showed increasing spectral widths at altitudes from 55 to 70 km during sunset. Using the EISCAT electron density data to constrain the model calculations, it was shown that the spectral width variation is most probably explained by a rapid change in the concentration of neutral atomic oxygen. Figure 14 shows scaled partial derivatives of the spectral width with respect to the concentration of the neutral constituent, for those neutrals which affect the spectral width. The scaling is done by multiplying the derivative by the concentration of the neutral species. The largest effect is seen from variations of temperature and the major neutrals, through changes in collision frequency. Variations of nitric oxide cause changes in spectral width, but rapid changes in NO concentration are not expected. Atomic oxygen on the other hand, is known to have a large day-to-night variability below 80 km, and could thus explain the spectral width variations. For sunlit conditions, it would be possible to fit the experimental spectral width at higher altitudes by adjusting the temperature by a reasonable amount (~20 K, relative to MSIS90). It would also be possible to fit the concentration of atomic oxygen during sunset if the variations of other minor constituents could be regarded as known (del Pozo et al, 1997).

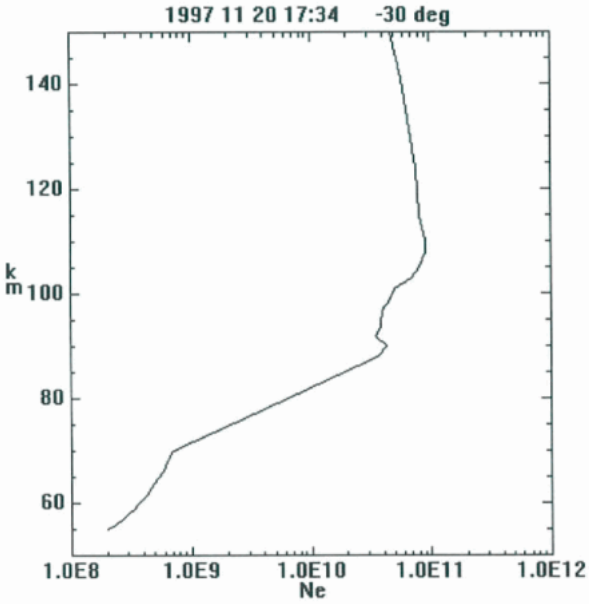

Figure 15: Combined electron density profile using ESR data and in situ measurements made by the Isbjørn payload.

The SAMPEX satellite measures the most energetic part of the electron population (above 150 keV). These electrons should reach very low altitudes (~90 km) and EISCAT measurements made at these altitudes have been inverted to recover an estimate of the integral flux of the energetic particles which should have been measured at the satellite. The inversion was the first attempt to make use of a complex D-region chemical model developed for a comparison which would otherwise have been rendered impossible. Some very good agreements between the derived fluxes and the SAMPEX measurements have been found, particularly for close conjunctions. Data from the IRIS riometer system have also been used to investigate the structure of the regions of hard precipitation in order to validate the comparisons (del Pozo et al, 1998).

In November 1997, the ESR was used in conjunction with the first sounding rocket launches from the SVALRAK facility at NyÅlesund. Figure 15 shows the ESR electron density profile, normalised to local ionosonde

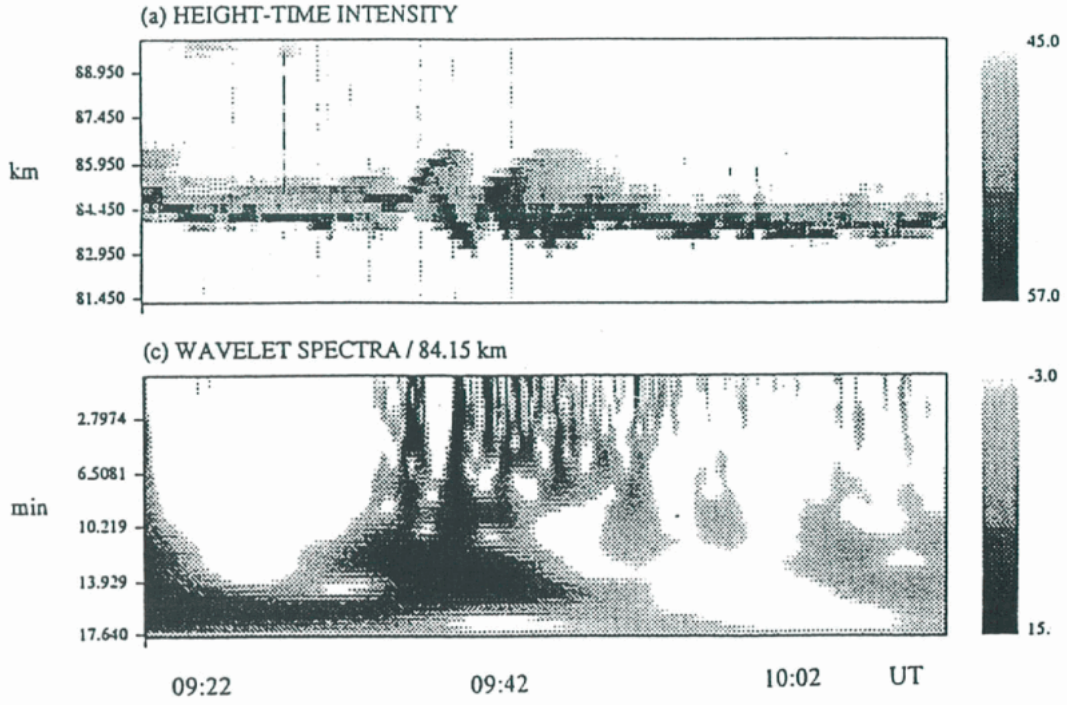

Figure 16: Height-time-intensity plot (upper panel) of a PMSE layer, observed on 16 June 1994 with the EISCAT VHF radar, with wavelet spectra (lower panel) showing the power density, of velocity variations in the range gate 84.15 km

measurements and extended into the lower mesosphere using positive ion probe data from the ISBJØRN campaign.

The relative usefulness of CP-1 versus CP-2 for determination of lower thermosphere neutral wind has been investigated using an MF system at Tromsø. The EISCAT estimates agree well with the MF results when large numbers of profiles are averaged, but for case studies, EISCAT indicated large departures on occasion. It would appear that the classic means of determining the neutral wind in the E-region via an F-region-determined E-field is more difficult than hitherto believed because of the latter's either non-stationarity, non homogeneity or both.

Considerable advances have been made in utilisation of VHF data. While much interest has centred on PMSE and related phenomena, vertical velocity information from CP-6 has been used to derive characteristic vertical wave numbers and thus information on the upper limit for turbulent energy dissipation rate in the mesosphere. The results show good agreement with corresponding MF-derived values and in-situ measurements.

Polar Mesospheric Summer Echoes (PMSE)

A significant new theory to explain the existence and phenomenology of Polar Mesosphere Summer Echoes (PMSE) has been developed. This theory has produced predictions which can best be tested by combined UHF and VHF experiments during the period of changing conditions at either the beginning or the end of the PMSE season. Experiments aimed at confirming these theoretical predictions were carried out in June 1997. The ideas underlying the theory are being developed and tested with a simple model of the ice-forming behaviour in a summer mesopause with tidal or other temperature oscillations present (Chaxel, 1997, Chaxel and Aylward, 1997).

Wavelet analysis has been applied to the interpretation of data deduced from the Doppler spectra of PMSE signals. For clarification of the procedure we note that first the raw data time series of the complex data is Fourier transformed. From the corresponding Doppler spectrum the first moments are deduced, namely the power, the Doppler shift and the spectrum width. One could also deduce these parameters from the complex auto-correlation function. To get the velocity spectrum or wavelet spectra one uses the velocity time series, which is deduced by standard fitting procedures from the Doppler. This was done for the event of 16 June 1994 (Pan and Röttger, 1995). There was a rapid vertical variation of the PMSE layer around 09:40 UT, which was not an artefact due to spectral aliasing but a real jump in velocity. The echo power time series shows that the signal was about 3-5 dB over the noise level during this event, allowing significant velocity estimates to be deduced. Figure 16shows the

original height-time-intensity and the corresponding wavelet spectra for the range gate at 84.15 km

The wavelet spectra may be interpreted as follows: until about 09:30 UT a long-period oscillation dominated while smaller velocity fluctuations increased the spectral power density

Significant high frequency components can be seen in the wavelet spectra after 09:30 UT. There are indications of some interconnections from period ranges around ten minutes to higher frequencies, which occur after 09:40 UT. Also the long-period power density around 14 minutes fades away during this period, when there is a strengthening of power density at higher

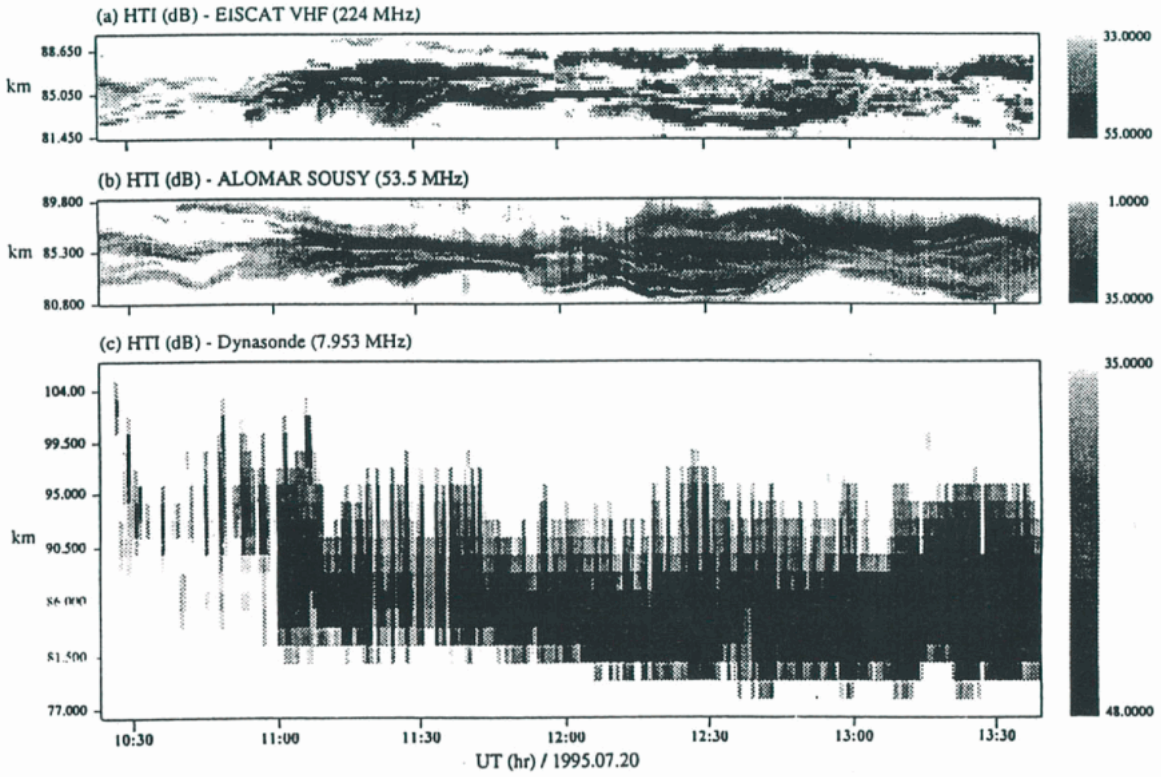

Figure 17: Height-time-intensity plots of echoes observed on 20 July 1995 with the EISCAT 224 MHz radar (upper panel), ALOMAR SOUSY 53.5 MHz radar (centre panel) and the EISCAT Dynasonde/Heating 7.953 MHz radar (lower panel).

for a few minutes. After 09:30 UT, a shorter period variation additionally occurred around 12 minutes, which slowly changed to longer periods around 15 minutes and then faded out around 09:50 UT. After 09:30 UT there were strong higher frequency components. Two dominant contributions, stretching from about ten minutes to two minutes period, are obviously caused by the velocity jumps at 18 minutes and 22 minutes relative time. This cannot be interpreted as a decay of spectral power from longer to shorter periods, since this just results from the sudden jumps from positive to negative, followed by one from negative to positive a few minutes later. This is also seen in the vertical displacement of the layer, as seen in Figure 16 (upper panel). Spatial interferometer analyses shows that the PMSE layer was broken into pieces due to turbulence, which was created after this wave steepening event, when the velocity jumps had occurred (Pan and Röttger, 1997).

frequencies. The total power density of the velocity fluctuations within the whole frequency range is nearly constant. These observations are interpreted as a redistribution of fluctuation energy from low to high frequencies. In other words, the energy in long-period velocity variations decays into shorter period energy ranges. This is consistent with the decay of wave and turbulence energy in the inertial subrange. After about 09:55 UT the high-frequency fluctuations have ceased, or at least decreased significantly in their spectral energy density (Röttger, Pan, Liu, Chien and Chen).

On 20 July 1995 the VHF radar, operating on 224 MHz, was run simultaneously with the EISCAT Dynasonde, operated on the fixed frequency 7.953 MHz using part of the Heating facility transmitter, operating with one transmitter at 50 kW peak power and 23 dBi antenna gain, to increase the available signal to noise ratio.

These concurrent observations show that relatively strong echoes were detected on 7.953 MHz between 80 km and 90 km during times when PMSE were observed on 224 MHz and 53.5 MHz. Figure 17shows the height-time-intensity (HTI) plots from the three radars.

Figure 17 illustrates a significant similarity in the HTI-occurrence of these echoes. The 224 MHz PMSE are well correlated with the 53.5 MHz PMSE, although the locations are separated by 130 km in zonal direction. There is a small time shift between certain 224 MHz and 53.5 MHz structures. This was earlier observed by Kelley et al. (1990) and Bremer et al. (1996) and explained by a horizontal advection of the PMSE structures. When comparing the collocated 224 MHz and 7.953 MHz observations, it must be remembered that the height resolution on 7.953 MHz (about 2-4 km) is intrinsically more than an order of magnitude coarser than on 224 MHz. This does not allow the investigation of potential similarities in the fine structure, but it still allows an overall comparison. It is obvious that until about 11:00 UT the 224 MHz PMSE and the 7.953 MHz echoes are relatively weak, and both increase in strength almost simultaneously. Both echoes occur above 81 km. It is most likely that the extension of the 7.953 MHz echoes above the top height of the 224 MHz PMSE is due to the pulse width of the Dynasonde transmitter. However, the 7.953 MHz echoes occurring at altitudes 85 km and 100 km before 11:00 UT are a new observation, which needs further study. An initial attempt to estimate the effective cross sections of the irregularities at 0.67 m and 18.8 m indicates that on the average the cross section at the longer scale (7.953 MHz) is at least two orders of magnitude stronger than that at the shorter scale (224 MHz).

Simultaneous occurrence of these echoes suggests a relation of the irregularities at the corresponding Bragg wavelengths of 18.8 m (7.953 MHz) and 0.67 m (224 MHz). Investigating the PMSE Doppler spectra at 224 MHz for turbulence intensity and comparing that with the echo power on 8 MHz would give an indication whether the 8 MHz echoes are caused by scatter from turbulence induced irregularities, or possibly caused by partial reflection from the gradients of electron depletions. Partial reflection at 224 MHz cannot be excluded but it is assumed that it could occur at the spatial scale of some 20 m, as it applies for the 7.953 MHz observations. If there would be increased turbulence, the 224 MHz spectra would widen, and the 7.953 MHz signal would increase in strength. To check this spectrograms of the echoes on 224 MHz and 7.953 MHz have been inspected. When PMSE occurs on 224 MHz the spectra are broad, which means enhanced turbulence. The spectral width of the 7.935 MHz echoes is dominated by beam-width broadening and not consider it here. The intensity of the 7.953 MHz echoes, however, is used to compare with the spectral width, i.e. the turbulence intensity, seen with the 224 MHz system. Some events of spectral broadening can be found on 224 MHz coinciding with intensity increases on 7.953 MHz. Since the opposite also appears, it may argued that partial reflection also occurs (Röttger, Rietveld, Pan, Liu and Chen).

Another study of low-altitude scattering has examined mesospheric echoes recorded by the Dynasonde systems at Tromsø and Halley Bay, Antarctica. The study sought to obtain more information on the Dynasonde echoes by comparing the occurrence statistics of the echoes seen at the two sites. It is clear that unlike PMSE, mesosphere echoes seen by both Dynasonde systems maximise in the winter months (Jones and Davis).

Mesosphere echoes do occur in the summer months at Tromsø, though their occurrence frequency is reduced. No mesosphere echoes were seen at Halley Bay during the summer, possibly due to the lower sensitivity of the Halley system. There was no statistical evidence that the echoes seen in the summer were any different from those seen at other times of the year. However, only an intensive campaign of Dynasonde observations in conjunction with other radars which can observe PMSE would be capable of establishing whether the two phenomena are related.

Meteor Studies

The interest in meteor studies with radar has increased remarkably in recent years, mainly due to the expected Leonid meteor storms in November 1998 and 1999, but also as a consequence of major improvements in data collection and signal processing techniques at incoherent scatter radar facilities. The 33-year period parent comet (Tempel-Tuttle) of the Leonids will be at perihelion on February 28, 1998. Thus debris left from this and earlier solar passages is expected to cause meteor storms in middle November during the few following years as the Earth passes the comet orbit.

A series of measurements to observe Leonid meteors started in 1997 and will continue until 2000. For the first time the tristatic UHF system was used to observe meteors within a common interaction volume where the plasma generated by disintegrating meteoroids is simultaneously observable from three look directions. Given sufficient signal-to-noise ratio in all three UHF

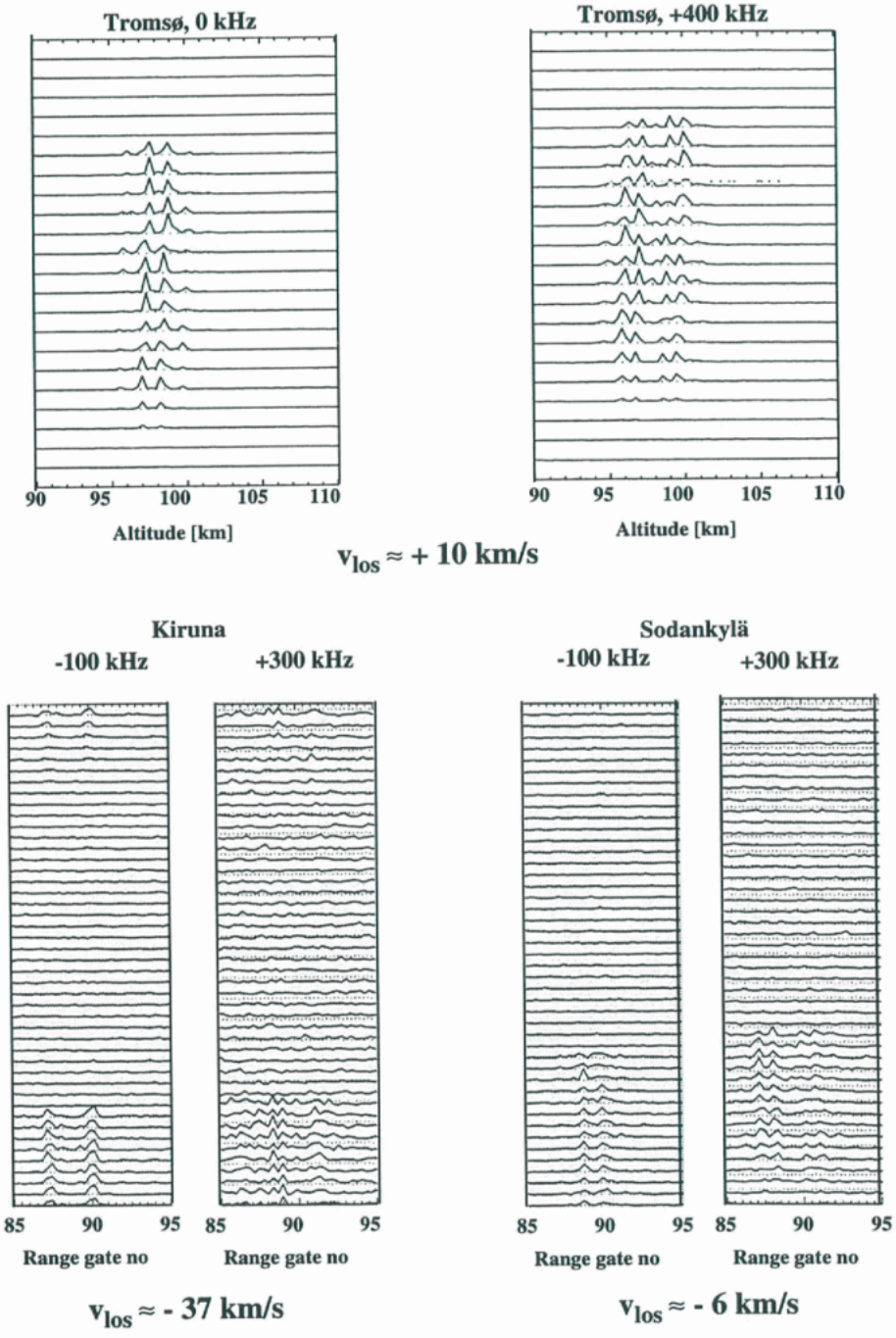

Figure 18: An example of a meteor observed from three sites (1997-11-17 18:33:20 UT) during the 1997 Leonid shower

receivers, the full target velocity vector can be determined. Thus even the origin of the meteoroid can be determined. There are three interesting possibilities. The target might belong to the solar system, be of shower (originating from a known comet) or of sporadic origin, or come from the interstellar space with a velocity larger than the solar system escape velocity. Figure 18 shows raw data from the three EISCAT sites Tromsø, Kiruna and Sodankylä. The modulation used in this experiment is a simple 13x2 μs Barker coded pulse, repeated at 4 ms intervals. The data are shown in stack plot format with each curve representing the received signal from a single radar pulse as a function of height (Tromsø) or range (Kiruna, Sodankylä). Time progresses from the top of the frame downwards. Due to the recording technique used, the number of 4 ms time slices is less in Tromsø than in the remote site data and the event does not appear at the same relative position in the remote data dumps as in Tromsø. The target velocity components along the three scattering **k** vectors are derived using an ambiguity function inversion

technique. At each site, two receiver channels with different frequency offsets relative to the transmitter frequency are used in order to remove the Doppler ambiguity which otherwise sets in above about 33 ms^{-1} due to spectral mirroring. The actual offset values are indicated above each data panel while the fitted velocities, v_{los}, are listed below each pair of panels belonging to a particular data set. Combining the velocities yields a total apparent target speed (with no corrections for proper motion) of ~62 kms^{-1} and an origin at ~(22h, -9°). This meteor has a planetary orbit, bit it is clearly not a Leonid (Wannberg et al., 1996).

Particle Precipitation and Auroral Processes

The EISCAT radars can monitor ions in the partially ionised ionosphere but optical instruments, like Fabry-Perot Interferometers (FPI), are often used to observe the neutral atmosphere. Along the geomagnetic field the motions of ions and neutrals should be closely related. In fact, the ions should be almost completely dragged along with the neutrals. Therefore, the field-aligned velocities of ions, measured by EISCAT, and of neutrals, measured by an FPI, can be compared directly with each other, EISCAT measures the ion velocity with a

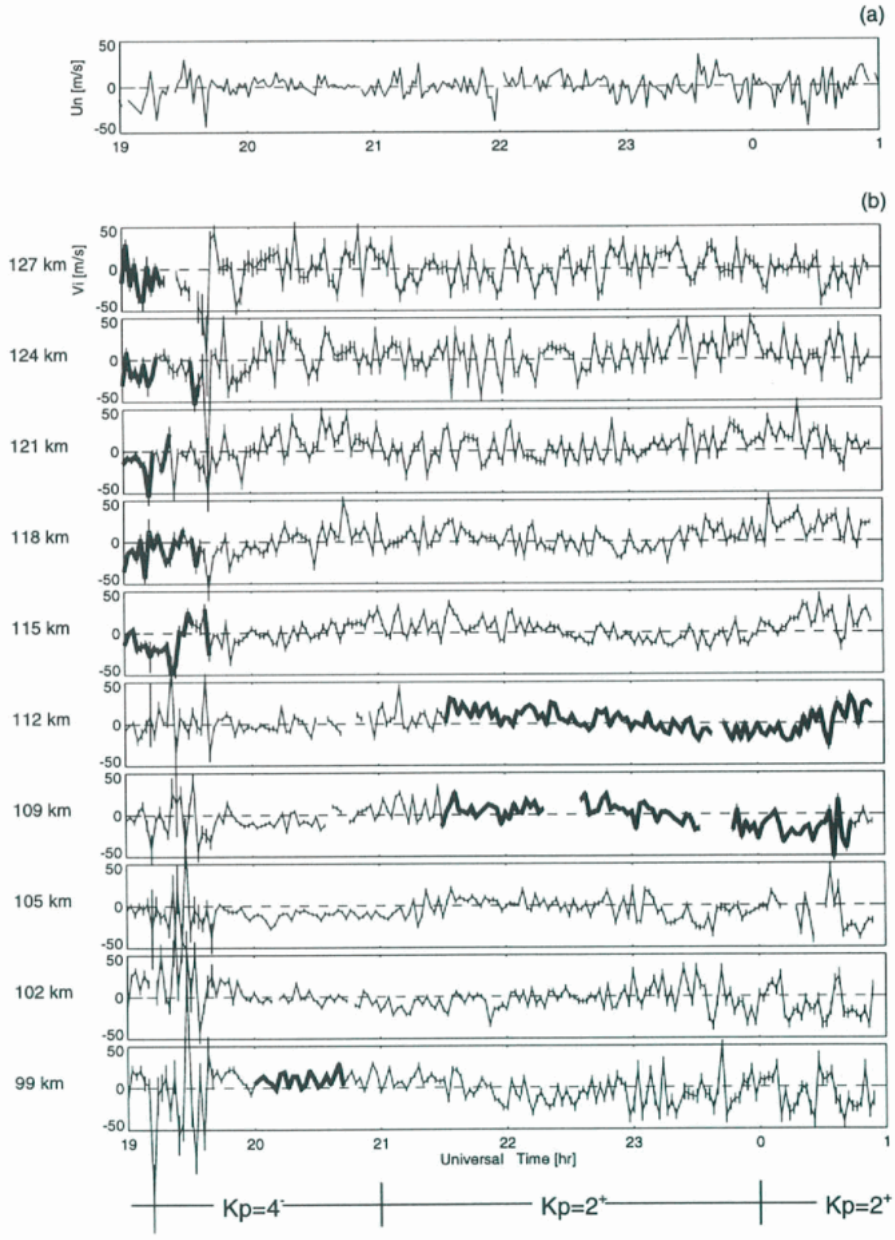

Figure 19: Time series of the field-aligned Doppler velocity of the green line seen with the FPI (top panel), and the ion velocity measured with the UHF radar at different altitudes from 99 to 127 km (lower panels). The thick curve indicates the altitude where the best agreement between the ion velocity and the green line observation was found

good height resolution of a few kilometres, while optical methods provide only a velocity that is averaged over a wider layer. The emission profile may vary considerably depending on geophysical conditions.

Simultaneous observations were conducted along the field-line using an FPI, which was relocated to Tromsø for the campaign, and the UHF radar, Figure 19. The analysis has concentrated on FPI data using the auroral green line (λ= 557.7 nm) emitted by atomic oxygen, O, predominantly in the E-region, in contrast to the more widely used red line (λ = 630.0 nm), also emitted by O, but typically around 240 km height. Comparison of the velocities from the green line and the ion plasma lines showed, that the emission layer of the green line strongly depends on the energy flux of precipitating electrons, whose characteristics were derived from the electron density profiles observed with the UHF radar. During a period of strong precipitation, accompanied by geomagnetic disturbances indicating substorm activity, a relatively good agreement between field-aligned ion and neutral wind velocities was found as low as 99 km altitude compared to 115-127 km in the quiet period before the disturbance. After recovery from the substorm a relatively quiet period followed again. Then the height of agreement went back up to 109-112 km. These variations suggest that the height range of the peak emission rate of the auroral green line shifts considerably up and down. Without knowledge of the electron density profile it would be difficult to determine the height at which the FPI observes, at least during geomagnetically active times (Oyama et al).

The drift velocity of an auroral arc with respect to the background convection flow, as indicated by F-region plasma velocity, has been a topic of interest for several years. It is not straightforward to measure a unique drift velocity for an auroral feature, which often changes rapidly in appearance and in orientation. Neither is it straightforward to measure the convection velocity, which also varies rapidly in magnitude and direction. A search was therefore made of the whole EISCAT database to study cases where a simple arc was observed, by the Finnish network of all-sky cameras, drifting steadily without any major change in appearance or orientation while EISCAT was making appropriate measurements of F-region plasma velocity.

In each case, the position of the lower boundary of the auroral arc was plotted in latitude and longitude at 1-minute intervals and a straight line was fitted to each plot where appropriate. An example is given for a simple arc observed drifting equatorward over EISCAT on January 25 1993, during the growth phase of the substorm cycle. Figure 20 plots the latitude of the fitted line versus time at four different longitudes. From these four curves it is possible to determine an average southward velocity with a standard error which automatically incorporates all errors introduced by changes in appearance or orientation of the arc.

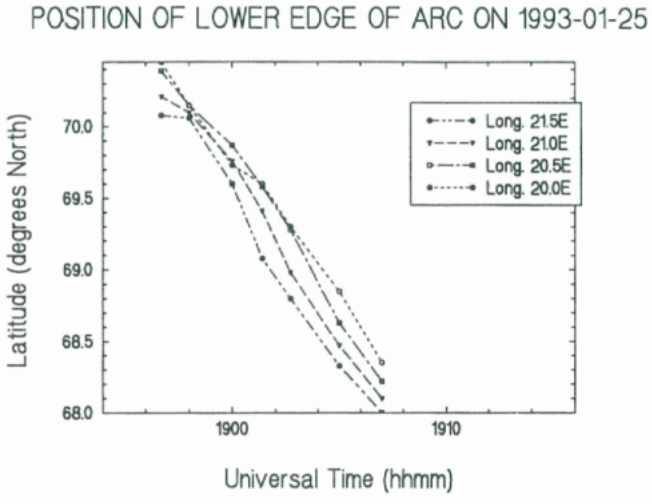

Figure 20: Drift in latitude of the lower edge of an arc at four different longitudes on January 25 1993 between 18:57 and 19:07 UT.

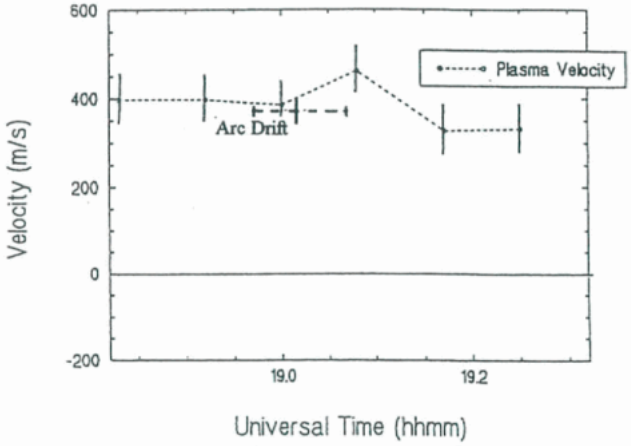

Figure 21: (a) Comparison of arc drift velocity (indicated by broken line) and plasma velocity in the same direction (indicated by a dotted line), January 25 1993

In Figure 21, the drift velocity of the arc is compared with the component of F-region plasma velocity in the same direction measured by EISCAT CP-1. It is clear that within the range of observational error there is no significant difference between the two velocities.

10 cases where the optical and EISCAT data allowed the comparison to be made with adequate precision were considered. The conclusion is that

during the growth and recovery phases of the substorm cycle the drift velocity of the arc is close to the average background convection velocity. However, during the two cases where a simple arc was observed during the expansion phase, drifting steadily equatorward without major change in appearance or orientation, the drift velocity of the arc was substantially greater than the convection velocity. This appears to resolve the contradictory results previously reported.

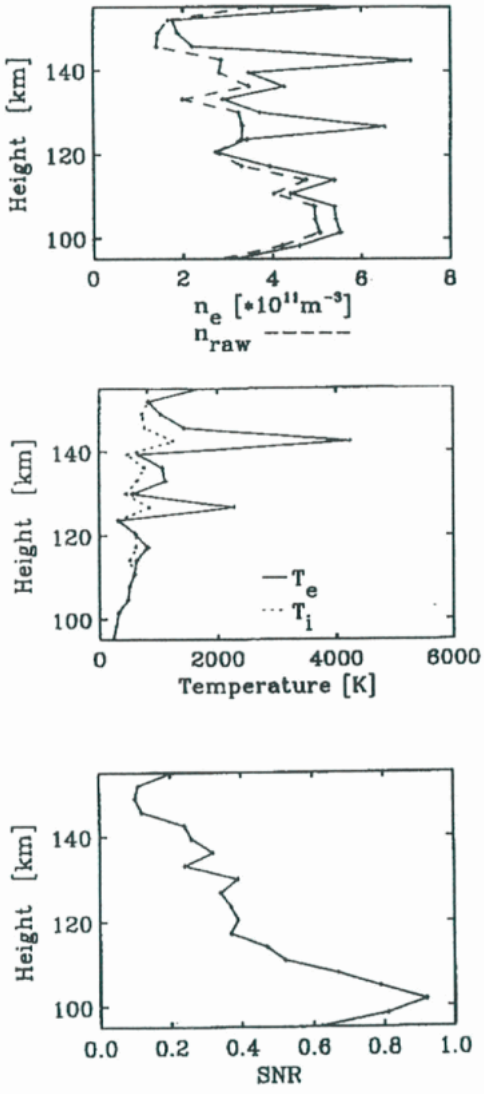

Figure 22: Electron density and electron temperature profiles for a five second interval measured on April 12, 1994 at 18:37:40 UT. Thin layers of both quantities, supposed to be signatures of a beam-plasma instability, can be seen. The signal-to-noise profile is also included.

Thin layers of auroral luminosity, so called 'enhanced aurora' cannot be explained in terms of collisional interaction of auroral keV-particles and neutrals. Instead, a new theory is based on collisionless beam-plasma interaction has been developed. This theory predicts narrow layers of enhanced ionisation and elevated electron temperatures in the height range of 120 to 150 km. A search conducted in the EISCAT CP-1 and CP-2 data base between 1985 and 1995 yielded 55 examples of such layers. One is shown in Figure 22. A detailed study of the single five second ACF's revealed that these layers are indeed significant and not artefacts or measuring errors. Several characteristics of the observed thin layers agree with predictions of the above mentioned theory including their width and height distribution, as well as the electron temperatures varying between 1000 K and 3500 K (Schlesier, Mishin, Schlegel)

High-resolution studies of the small scale structure associated with auroral arcs have combined EISCAT measurements, optical images and photometer measurements with theoretical work on auroral modelling. The auroral model incorporates the electron transport and ion chemistry that is involved in electron precipitation into the atmosphere. This continues to be refined to study the response of ion and electron temperatures to auroral precipitation. Parallel work has been concentrated on the mechanism in the inner magnetosphere responsible for the very narrow and dynamic elemental structures seen in the aurora.

Examples of the measurements that are combined in this work are shown in Figure 23. It contains two minutes of data when an 'arc' moved from south to north into the field of view of the radar and photometer (both aligned with the magnetic field), moved away again to the south, then advanced at a steady rate back through magnetic zenith and away to the north. This interval has been the subject of a detailed study, using modelling to investigate the changes in the electron density profiles as the precipitating flux underwent huge and sudden changes. It can be seen from the middle panel of Figure 23 that very large and variable electric fields were measured during this event. This is also seen in the images in Figure 24, in which the horizontal electric field vectors for the time close to each image are superimposed. The images start during the first passage of the arc system. The largest electric field vector occurs in the third panel, which is sampled from an interval of several seconds when the arc was not in the radar beam. The field points towards the brightest part of the arc, where a fold in its length is present. The directions of the electric field vectors throughout this event are well correlated with the direction of the brightest part of the arc. It must be remembered that the vectors are at three second resolution, in which time the aurora changes greatly. Without the

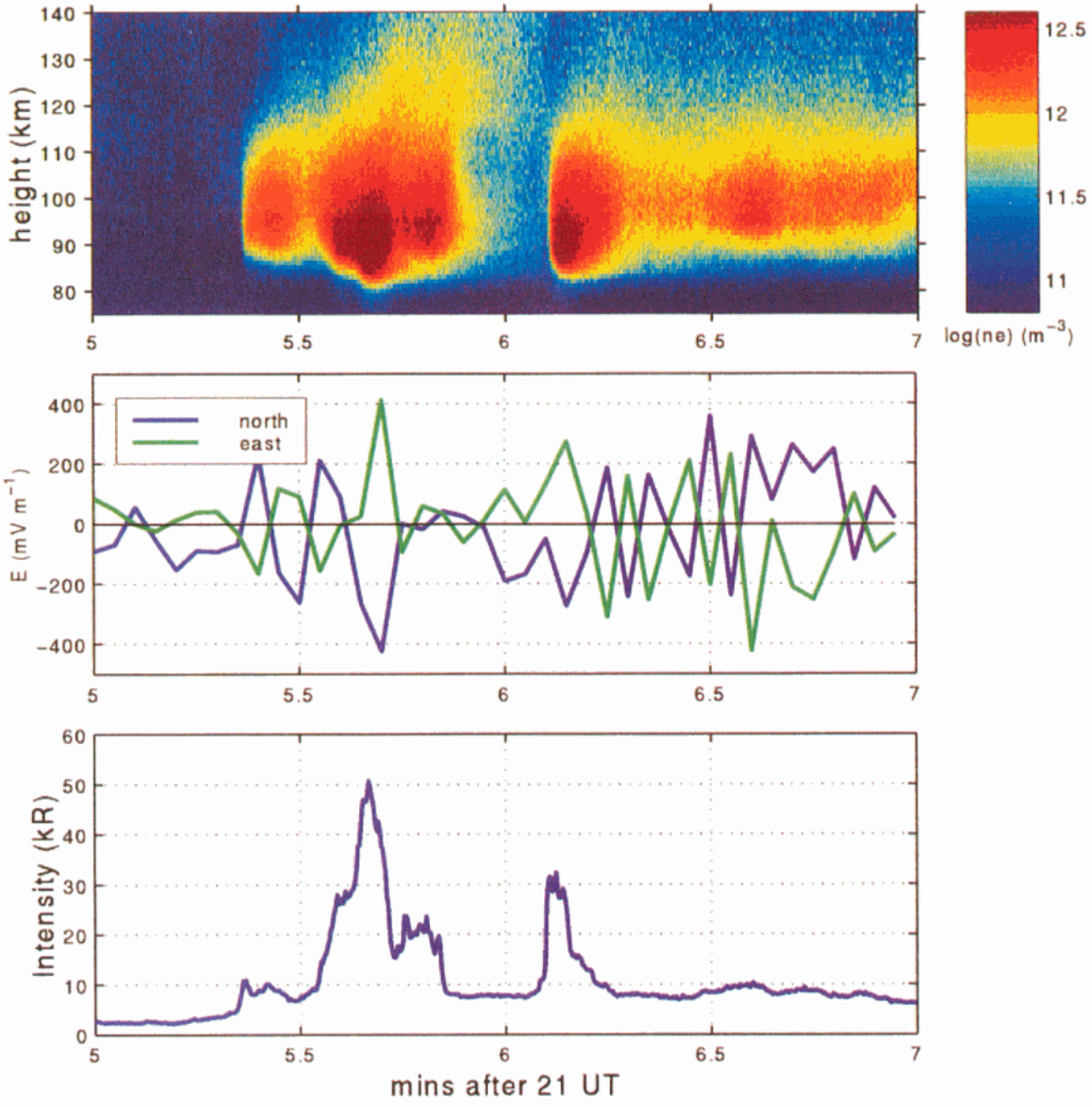

Figure 23: Top panel - Electron density profiles at 0.2 s resolution showing two passages of an arc system through the field-aligned radar. Middle panel - Horizontal electric field components at 3 s resolution measured at 278 km. The largest field at 21:05:42 UT is in SE direction. Bottom panel - Intensity of 427.8 nm emission rate in the field parallel direction

images, it would appear from Figure 23 that the largest field occurred inside an arc, at least judging from the electron density variations. Although the arc is not in the beam at this time, the electron density is unable to respond on these time scales. This work that the short term changes in electric fields were related to temporal variations within the nearby arc system (Lanchester et al., 1996).

It can be seen from the images in Figure 24 that the aurora in this case is not a single arc, but made up of two main bands, inside which there are several very fine elements. Figure 25 shows the results of a full model run for this event lasting 10 s. The modelled electron density (d) reproduces the measured density extremely well, but only by including as input an energy flux many times greater than the flux measured by the photometer (c). This verifies what is seen in the narrow angle images, that the elemental structures in the arc are much narrower than the photometer and radar fields of view, on average about 100 m in width. Contained in these are large energy fluxes, sometimes as great as 1 Wm^{-2}, which are found by modelling to be of mono-energetic electrons, within a wider region of Maxwellian precipitation (Lanchester et al., 1997).

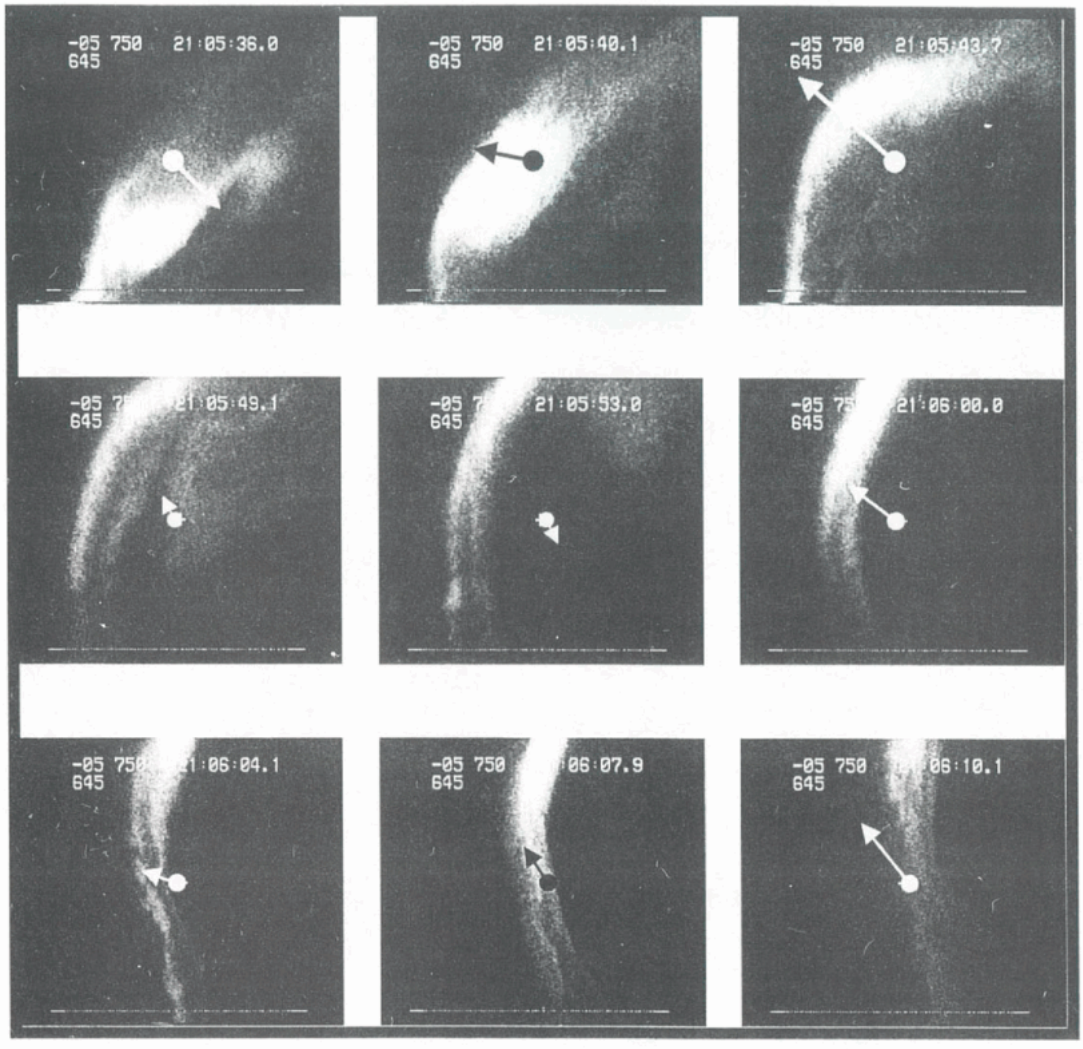

Figure 24: A sequence of images from the wide angle camera at 21:05:36.0, 40.1, 43.7, 49.1, 53.0, and 21:06:00.0, 04.1, 07.9, 10.1 UT. North is to the right and east at the top. The horizontal electric field vectors (3 s resolution) are superimposed. The largest field (panel 3) has magnitude 600 mVm^{-1}.

This discovery has direct consequences for the theoretical understanding of the origin of structured auroral arcs above the ionosphere and the mechanisms that produce field-aligned currents with such fine structure within the larger current system. The theoretical model of Otto and Birk (1994) is capable of producing thin arcs. The 3-D simulation of magnetic shear in the lower magnetosphere generates the time evolution of the field-aligned potential drop in two seconds and the simulation is able to produce field-aligned currents associated with this type of feature, Figure 26, consistent with the broader region of precipitation shown by the ionospheric model and optical observations (Lanchester et al., 1997).

The dynamic characteristics of energetic particle precipitation that we observe in optical images and in the response of electron densities measured by the radar imply an equally dynamic response in the plasma temperatures. Work in progress is aimed at modelling the evolution of electron and ion temperatures in response to particle precipitation with different spectral characteristics. The results should substantially aid the interpretation of temperature data acquired by the radar.

The same data as was used for the high time resolution study of auroral arcs was also employed for a comparison of ground and satellite data. The aim has been to compare data sets from EISCAT and satellites during the closest approach of the satellite to Tromsø. This has been done using inversion algorithms by which the spectrum of precipitating particles could be recovered from the EISCAT data or the EISCAT profile could be derived from the satellite data. The comparison has enabled these inversion techniques to be validated and an assessment made of the circumstances under which it is appropriate to compare the two data

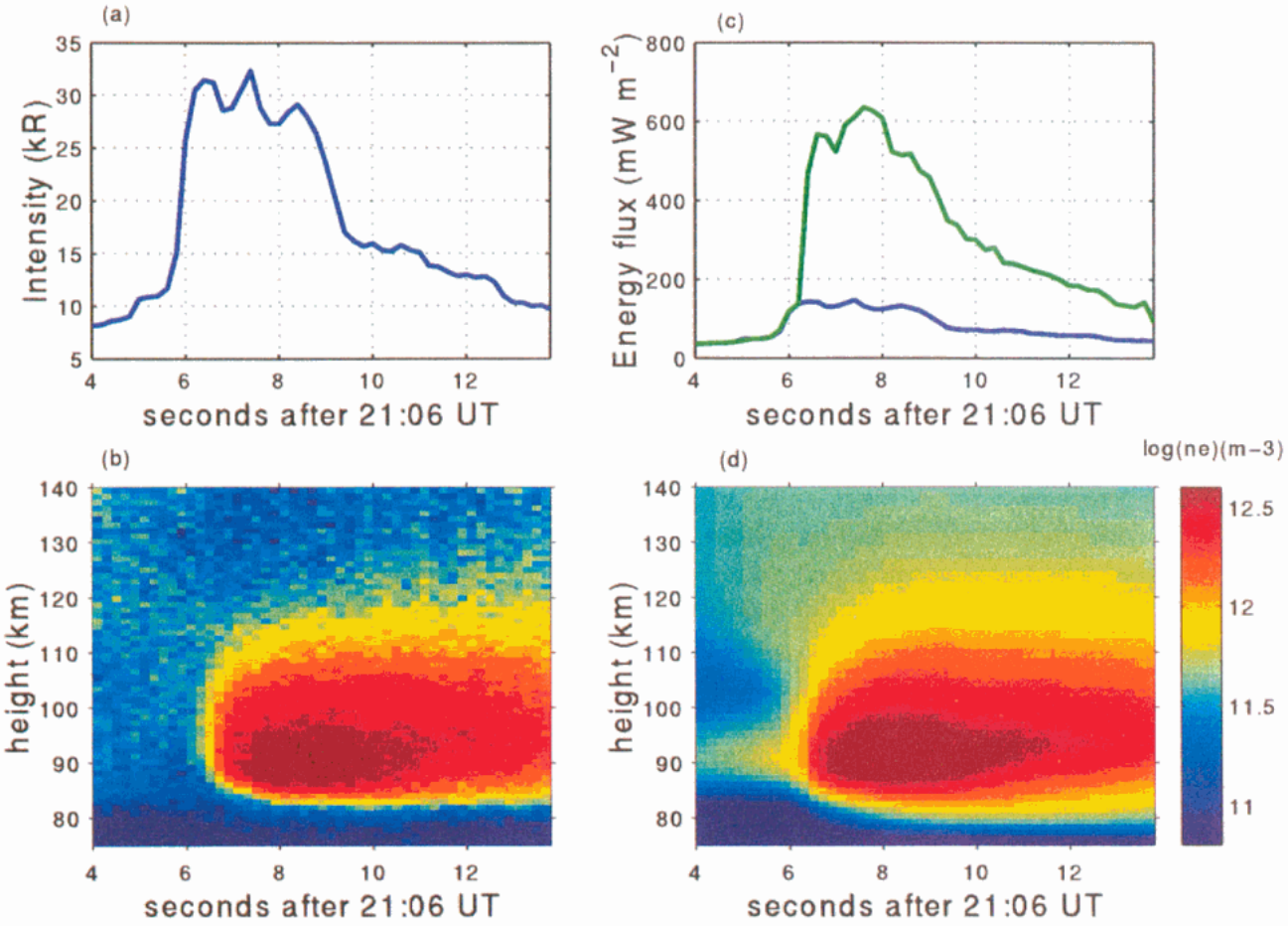

Figure 25 (a) Measured 427.8 nm emission rate for 10 s and (b) electron density at 0.2 s resolution during second passage of arc system. (c) Blue curve is the energy flux estimated from 427.8 nm emission rate as shown in (a). Green curve is the energy flux required to produce the electron density profiles shown in (d), which match the measured profiles well.

sets. The DMSP satellites (DMSP-F10 and F12) predominantly measure soft electrons in an energy range from 30 eV to 30 keV. An electron transport code was used to estimate the ionospheric density profile which would be expected given the electron flux measured at the

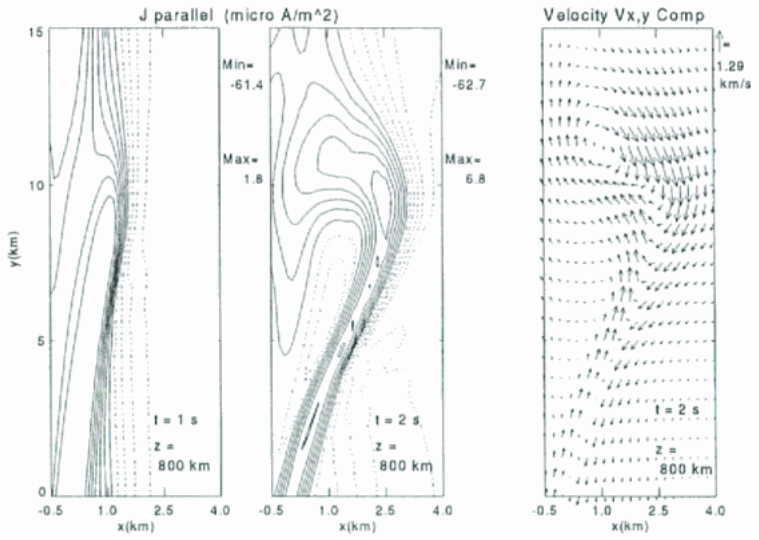

Figure 26: Contours of field-aligned current density for time t = 1 s and t = 2 s, and arrows indicating the plasma velocity in a horizontal plane directly above the ionosphere as a result of the simulation.

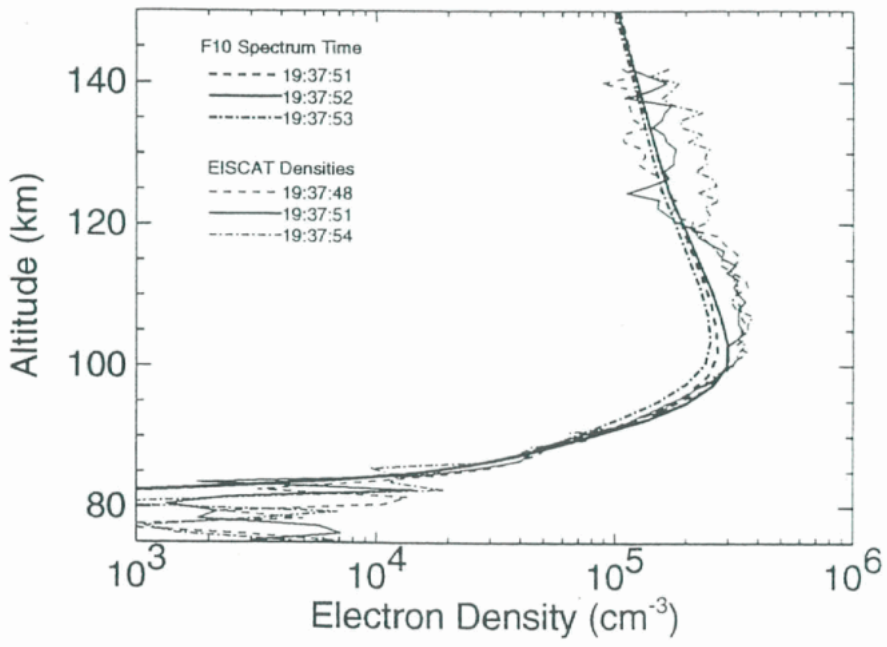

Figure 27: Upper panel: Comparison of electron density measured by EISCAT during a DMSP pass (normal lines) with the density reconstructed from DMSP particle measurements using an electron transport code (bold lines).

satellite. These estimates were compared with actual radar measurements and the results were found to be in close accord, particularly for periods such as that shown in Figure 27. when satellite imager data indicated that the precipitation was homogeneous and unstructured over a wide area (Anderson et al, 1997).

E-Region

In the Earth's ionosphere, electrons carry the current transverse to the electric field (Hall current), and ions carry the current along the electric field (Pedersen current). This arises because of the particular ratio of the geomagnetic field strength and neutral atmospheric density, which leads below about 130 km altitude to a demagnetisation of ions, but not of the electrons. Demagnetisation by frequent collisions between ions and neutrals renders the Lorentz force ineffective. In the lower E-region the ions move parallel instead of across the electric field.

Waves can have an effect similar to collisions. In the E-region such waves are excited when the electric field exceeds a certain threshold. Then the Hall current becomes unstable, generating waves with random phases. The wave-electron interaction also occurs randomly, producing heat. The heat production can be seen by the UHF radar as increases in the electron temperature at altitudes between about 100 and 115km, where the Hall current is strongest. According to the principle of energy conservation, this heat production must be due to an additional Pedersen current which is dissipative. It cannot be carried by the ions, which are almost frozen into the neutral gas. Thus we are able to derive from the data the electron Pedersen conductivity. It amounts to about 20% of the ion Pedersen conductivity, when the electric field is strong. We can also compare the three main heat sources of the E-region, namely those related to ionisation, and to ion and electron Pedersen currents. Figure 28 shows profiles of the electron and ion temperatures, the electron and ion Pedersen conductivities, and heating rates for a particularly strong event (Buchert and Saito).

Ionospheric conductivity is not easily measured directly. There are many instances where a real-time estimate of ionospheric conductivity over a large field of view is highly desirable at a high temporal and spatial resolution. Incoherent scatter radars offer the best method but can only measure at one point in the sky at any one time and are limited in their time resolution. Statistical models of average conductivity are available but these may not be applied to individual case studies such as substorms. All such models are essentially static except for some fairly crude range steps in Ae or Kp. Especially for nocturnal conductivities at high latitudes, local perturbations such as auroral precipitation may dominate making statistical conductivity models inappropriate for case studies. EISCAT can, with

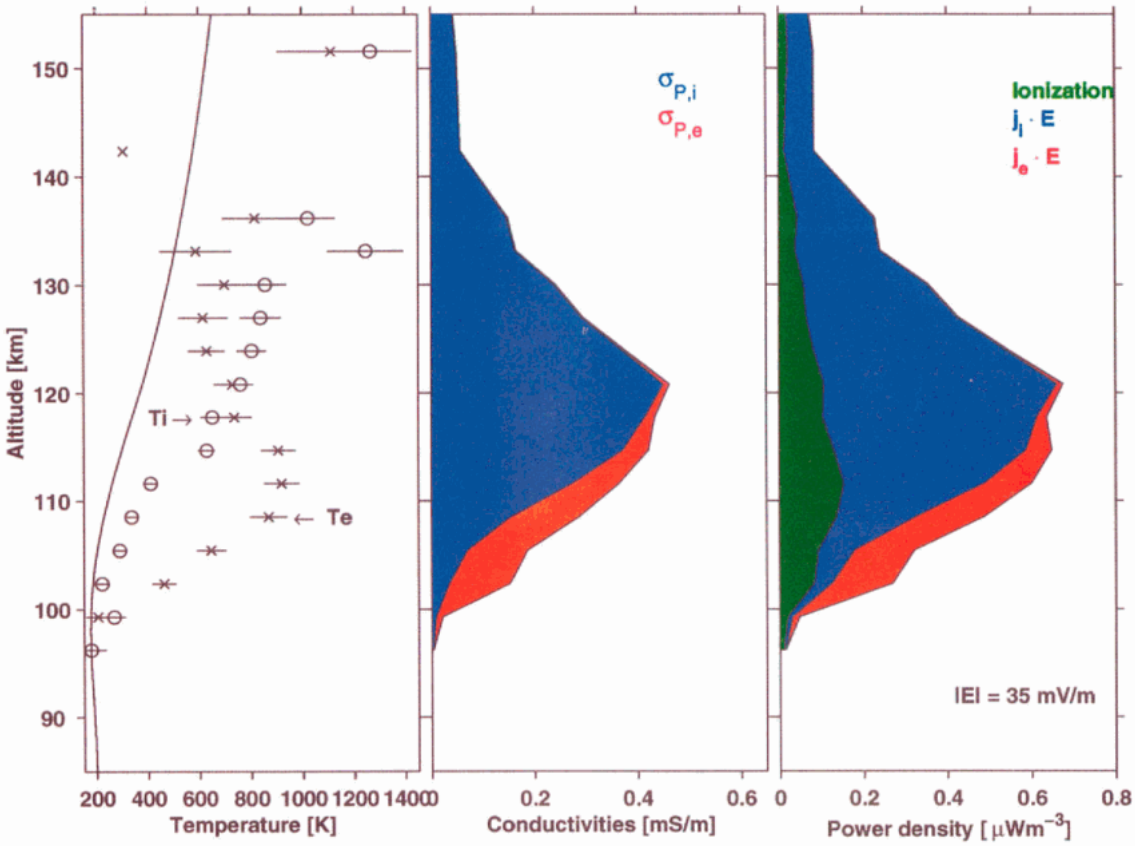

Figure 28: Profiles of T_e, T_i and T_n (left panel), Pedersen conductivities (middle panel) and Joule heating (right panel). The ion contribution to conductivity and heating in blue colour, the electron contribution in red. In the right panel the heating due to ionisation processes has been plotted in green. Tn is from the MSIS model.

the assistance of atmospheric models, make height-resolved estimates of both the ionospheric Hall and Pedersen conductivity.

It is possible to make a reasonable estimate of the nocturnal height integrated Pedersen conductivity, or conductance, with a single all-sky TV camera operating at 557.7 nm. However, this is not the case for the Hall conductance where at least two auroral wavelengths should be imaged in order to additionally estimate the energy of the precipitating particles.

EISCAT data show that main contribution to the Pedersen and Hall conductivities from precipitating particles comes from 120-150 km and 80-130 km altitudes, respectively.

High energy particles penetrate to lower altitudes in the atmosphere thereby contributing to both conductivities, whereas low energy particles do not penetrate so deeply and hence mostly contribute to the Pedersen component. It is for this reason that Hall and Pedersen conductivities are strongly and weakly, respectively, energy dependent. Of course, both conductances are equally flux dependent.

A Digital All-Sky Imager (DASI) has been designed for studies of the optical aurora and includes EISCAT within the field of view. The detector consists of a monochrome low-light-level TV camera fitted with an all-sky lens. An interference filter at 557.7 nm selects the strongest auroral emission. The camera has been calibrated, as well as flat-field corrected, in Rayleighs. The TV images are digitally integrated in real-time with a user-defined temporal resolution, transformed from all-sky format into any spatial grid and saved to disk for later analysis. The spatial orientation of the camera and lens is fixed through star observations. The frequent gain changes necessary are computer controlled and recorded by the software, thus permitting each processed image to be recalled in calibrated units. DASI has been located at Skibotn, Norway (69.35°N, 20.36°E), which is about 50 km from EISCAT because of the superior local night-sky viewing conditions there (Kosch, Hagfors and Nielsen).

EISCAT CP-1 and DASI data from the nights of 28 February through to 2 March 1995, the night of 28-29 March 1995 as well as the night of 13-14 February 1996 has been used for a specific study.

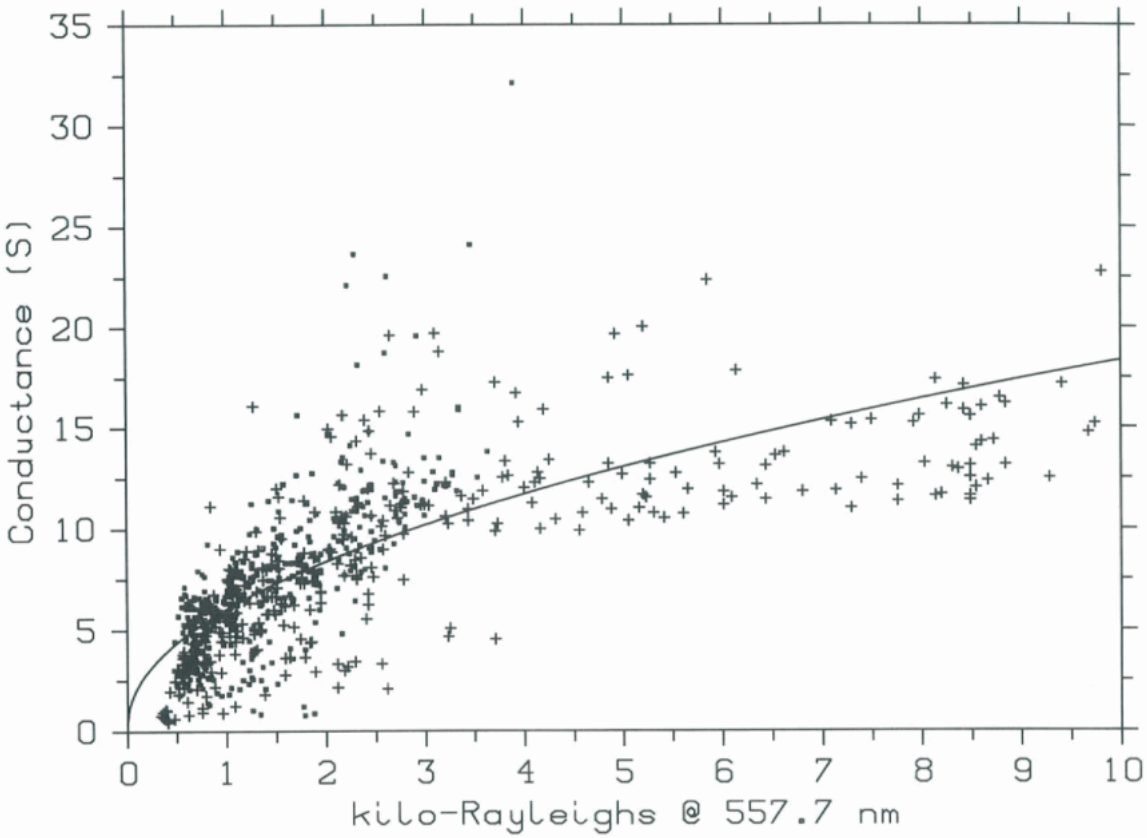

Figure 29: scatter plot of Pedersen conductance, from EISCAT, versus auroral optical intensity, from DASI.

Figure 29 shows a scatter plot of Pedersen conductance, from EISCAT, versus auroral optical intensity, from DASI.

Also shown is the least-squares fit to the data: $P=0.34+0.18\sqrt{I}$, where P is Pedersen conductance (Siemens) and I is Rayleighs at 557.7 nm. The accuracy of the curve fit is approximately 30-45% for lower auroral intensities (<4000 Rayleighs) improving to around 20-25% for higher intensities. Figure 30 shows an example of using this relationship together with a DASI auroral image (left panel) to achieve an instantaneous map of Pedersen conductance (right panel) throughout a large field of view (67.6-72.6°N, 13.5-26.0°E). The example is a ten second average taken at 18:47:30 UT on 13 February 1996.

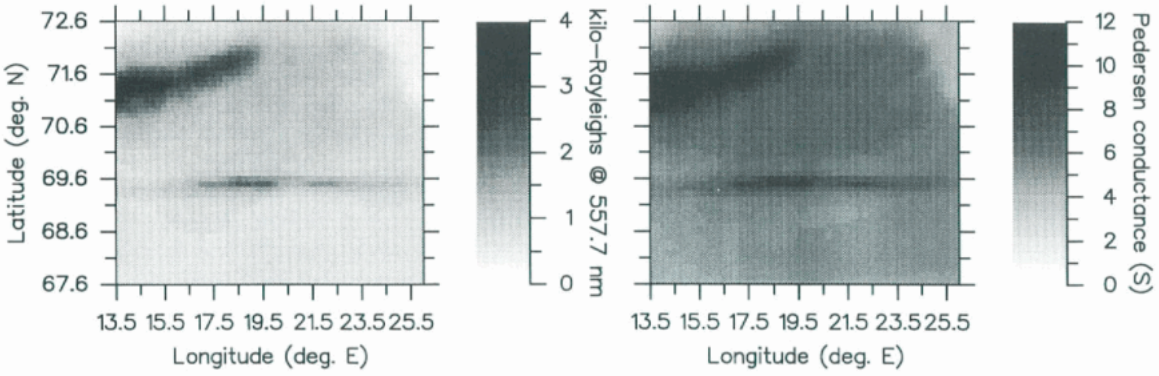

Figure 30: The DASI auroral image (left panel) is used to achieve an instantaneous map of Pedersen conductance (right panel).

Simultaneous measurements by EISCAT, optical and riometer absorption images have been studied to produce empirical maps of Hall conductance. It has recently been shown that it is possible to produce Pedersen conductance maps from optical images. This study will enable real-time global distributions of ionospheric conductivity to be constructed, and provide answers to questions involving the average energy and flux of precipitating magnetospheric particles. The optical emission measurements at 5577 nm made by DASI give estimates of the precipitation patterns of soft electrons, <10 keV. The recordings of the cosmic radio noise absorption made IRIS at 38.2 MHz provide estimates of the energy spectra of the precipitation patterns of hard electrons, >10 keV. With EISCAT measurements of the electron density profile, estimates of the energy spectra of precipitating particles can be made.

Estimates of the ion-neutral collision frequency are generally derived from the returned incoherent scatter signal through a spectral fitting technique, or equivalently from the autocorrelation function. An alternative method has been proposed which permits the derivation of two independent estimates of collision frequency based on the effect of ion-neutral collisions on the direction of the ion velocity vector and the ion velocity magnitude. The technique is demonstrated using EISCAT CP-1 observations from 3 April, 1992. During this period, the ionospheric electric field was enhanced over a five hour interval to values exceeding 100 mVm^{-1}. The effect of thermospheric motion is accounted for through the inclusion of a first-order estimate of the neutral wind derived from ion energy balance considerations. Derived values of the normalised collision frequency (the ratio of the ion-neutral collision frequency to the ion gyro-frequency) are consistent with predicted values, the latter being derived from the MSIS-86 model thermosphere and the IGRF magnetic field model. This method can provide estimates of the ion-neutral collision frequency to far higher altitudes than can be retrieved from a conventional fitting technique. Above 110 km the effect of collisions on the incoherent scatter spectrum ceases to be significant, whereas their effect on the ion velocity, particularly its direction, is manifest (Davies et al., 1997b).

A numerical code has been developed in order to describe the effect of the proton precipitation on the ionosphere. It solves a coupled set of multi-stream transport equations for the protons and neutral hydrogen. It has been first widely tested and successfully compared to other two-stream codes. Then, the effect of the angular redistribution has been studied, both due to magnetic mirroring and to elastic and inelastic scattering. The first source has been proved insufficient to explain observed red shift on H emission Doppler profiles along the magnetic zenith. This suggests that Doppler profile measurements with high spectral resolution may allow better quantification of the angular scattering in proton aurora (Galand et al., 1997, Galand, Lilenstein, Kofman and Lummerzheim).

This code has then been coupled with an electron transport code in order to investigate the effect of dual precipitation. A computed electron density profile and an EISCAT electron density profile during a co-ordinated DMSP/EISCAT experiment has been successfully compared. This comparison allowed the examination of the proton beam spreading. Then, using a statistical model for the composition of the precipitation above Tromsø and Svalbard, it was shown that the proton precipitation can play a key role as a source of ionisation. Below about 145 km, it can even become the major source. Therefore the hydrogen component of the precipitation cannot be neglected in studies dealing with the high latitude ionosphere (Lilensten and Galand).

Neutral Atmosphere

E-region neutral winds can be deduced from EISCAT experiments, in particular CP-2. A new method has been developed that includes the determination of the ion-neutral collision frequency directly from the measurements. The tidal parameters of the horizontal winds have been calculated for the two long CP-2 campaigns of October 1992 and January 1993 and compared with models. The vertical component of the neutral wind is also determined in two independent ways. During the disturbed day of the October campaign very large vertical winds are obtained, as well as a large increase of the tidal amplitudes (Kofman et al., 1996).

EISCAT E-region neutral winds have also been compared to measurements obtained by the WINDII interferometer on board the UARS satellite during co-ordinated campaigns. A very good agreement has been obtained. These comparisons are part of the validation processes of the WINDII green line winds (Gault et al., 1996).

In the F-region, previous work had shown that the meridional wind deduced from the EISCAT experiments compare well with ground optical measurements of the meridional wind and with models providing that they are averaged over two hours (Lilensten and Lathuillere 1995), leaving an open question: are the oscillations of periods smaller than two hours real? Two directions of

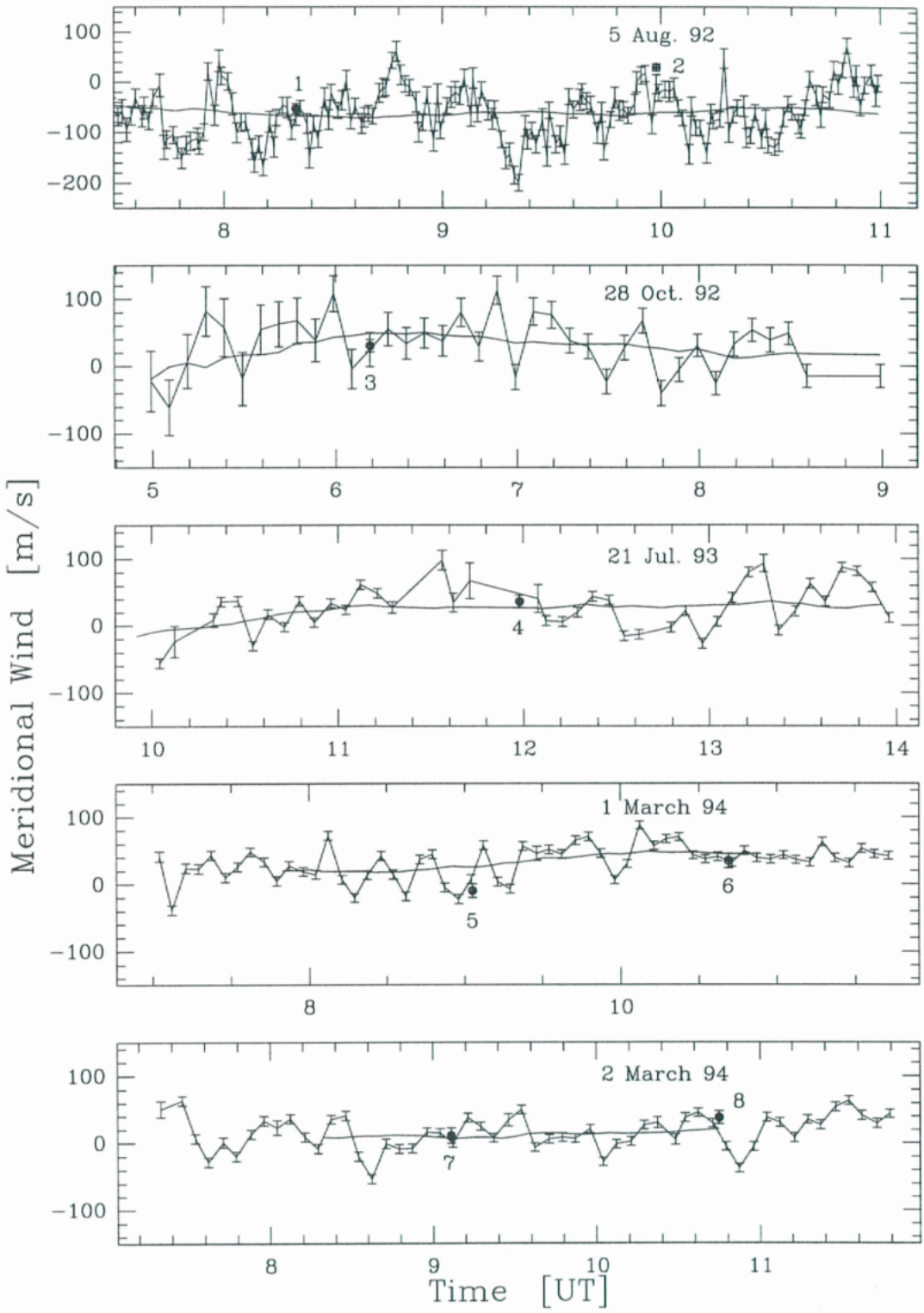

Figure 31: Time variations of the EISCAT meridional wind for quiet periods at 234 km altitude (1 March 1994) or 256 km (4 other days). The smooth line is a two hour running average. The WINDII wind values are superimposed and marked by reference numbers

research have been followed: first analysing different EISCAT experiments with several signal processing tools. That proved that some of the oscillations are noise, and some can be related to gravity waves (Lilensten and Amblard, 1996).

The neutral meridional wind calculated from EISCAT has also been compared with winds measured by WINDII interferometer in the O^{1}D emission during eleven passes of the WINDII fields of view near the radar facility. For the

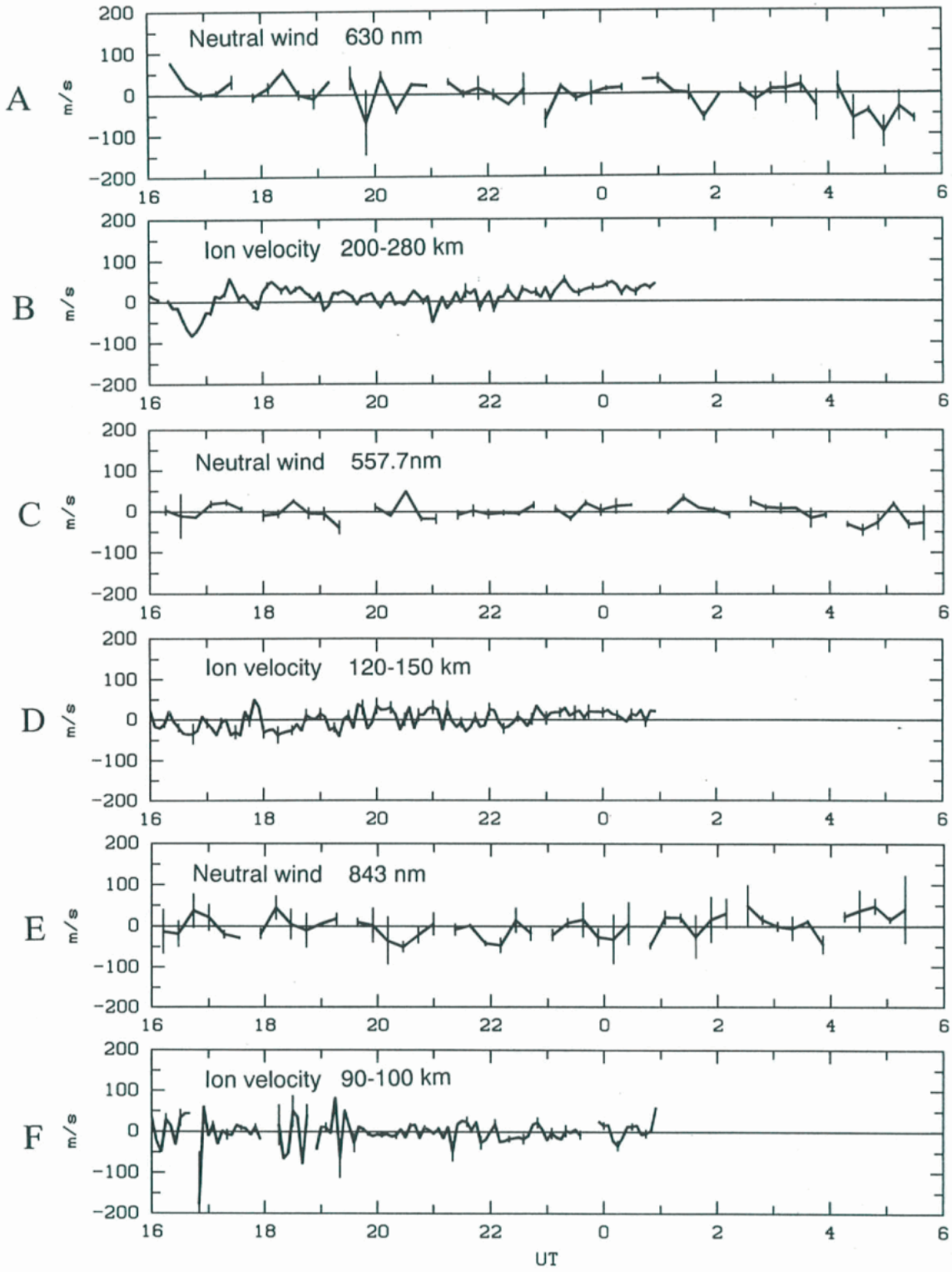

Figure 32: Thermospheric vertical neutral wind speeds and ion velocities measured by the FPI at Skibotn and the EISCAT UHF radar.

eight occasions when geomagnetic activity was low, the average difference in the meridional winds measured by the two methods is less than 10 ms-1. The EISCAT calculations were done with and without a "Burnside factor" of 1.7, and agreement with WINDII is somewhat better when the Burnside factor is not included. The three passes corresponding to disturbed conditions show poor agreement. In addition, agreement between EISCAT and WINDII is better when

unfiltered EISCAT winds are used, rather than the two-hour running mean used in earlier work, as shown Figure 31. This suggests that the short-term oscillations seen by EISCAT are real oscillations of the neutral atmosphere (Lathuillere et al., 1997).

Finally, EISCAT experiments over a full solar cycle between January 1984 and March 1995 have been used to construct a meridional wind model for magnetically quiet conditions at altitudes between 185 and 354 km. The diurnal, seasonal and solar flux variations obtained reflect that the thermospheric wind is driven by pressure gradients generated by solar radiation and auroral heating. The main result of the comparison with HWM model is the very good agreement obtained for the equatorial wind at night around 250 km altitude (Witasse et al., 1998).

Although the EISCAT incoherent-backscatter radar can make direct and accurate measurements of several ionospheric parameters, neutral atmospheric parameters have to be derived from the data by using various models or simplifying assumptions, which introduces uncertainty. Since the upper atmosphere consists of over 99% neutral atmosphere, there is a need to measure this component directly. Ground-based interferometers, when used for high resolution spectral analysis, are low-cost high-precision instruments capable of measuring two key upper-atmosphere parameters: neutral wind velocity and neutral temperature. This is done from observations of the Doppler shift and Doppler broadening, respectively, of suitable airglow and auroral optical emissions. Ground-based interferometers are the only reasonable way of making long-term continuous observations of the thermosphere and mesosphere. No other active or passive technique is readily available for the height range of 80 - 300 km.

On 8 February 1997, DASI was operated using a multi-wavelength sequence, namely, 630, 557.7 and 843 nm with assumed observing heights of 200-280 km (upper thermosphere), 120-150 (lower thermosphere) and 85-90 km (mesosphere), respectively. EISCAT was operated in the magnetic field aligned mode in the height range 90-583 km.

The thermospheric horizontal wind speeds derived using 630 nm were compared with the HWM90 neutral wind model. Generally, the horizontal winds are as expected. The meridional wind northward of Skibotn is in good agreement with the model, whereas southward of Skibotn the model predicts larger neutral winds. The zonal winds both eastward and westward of Skibotn are in good agreement with the model except for the evening hours where the observations show neutral winds of the opposite direction. The HWM90 model gives the statistically averaged expected neutral winds and therefore cannot be accurate in every instance. This is especially so for the auroral zone where strong localised effects are common. The measured neutral temperatures are in excellent agreement with the model. The neutral and ion (EISCAT) temperatures are also very consistent with ion temperatures being significantly larger at times. This is presumably due to ionospheric electric fields causing ion frictional heating.

Figure 32 shows vertical neutral wind speeds and ion velocities. Panels (a) and (b) show the upper thermospheric (630 nm) vertical wind and ion velocities in the height range 200-280 km, respectively. Panels (c) and (d) show the lower thermospheric (557.7 nm) vertical wind and ion velocities in the height range 120-150 km, respectively. Panels (e) and (f) show the mesospheric (843 nm) vertical wind and ion velocities in the height range 90-100 km, respectively. The positive direction is defined as upwards. Estimates of the errors of derived wind velocities are represented by vertical bars. In all cases, there is good statistical agreement in the amplitudes of the neutral wind speed and the ion velocities.

Neutral winds of the day-side lower E-region observed during quiet summer days were analysed using the CP-2 data to see whether the drag forces due to viscosity and/or ion-neutral collisions affected the balance between the pressure gradient force and the Coriolis force. Each term in the neutral momentum equation was calculated directly from measurements. The vertical profiles of the horizontal winds were used to estimate the viscous term. Since it was hard to calculate the time-dependent term and non-linear advection term from the present data set, these terms were included in pressure gradient force. The results indicate that below 110 km the winds were directed north-eastward, and that the estimated pressure gradient force was north-westward, suggesting that the Coriolis force balanced the pressure gradient force in this height region. The viscous drag increases greatly with increasing height, and became of the same order of magnitude as the Coriolis force above 116 km. The ion drag had a secondary effect on the momentum balance during the very quiet period. The contributions of the time dependent term and non-linear advection term on the momentum balance have been investigated (Maeda, Fujiwara and Nozawa).

Using data obtained by the UHF radar, E-region neutral wind characteristics between 95 and

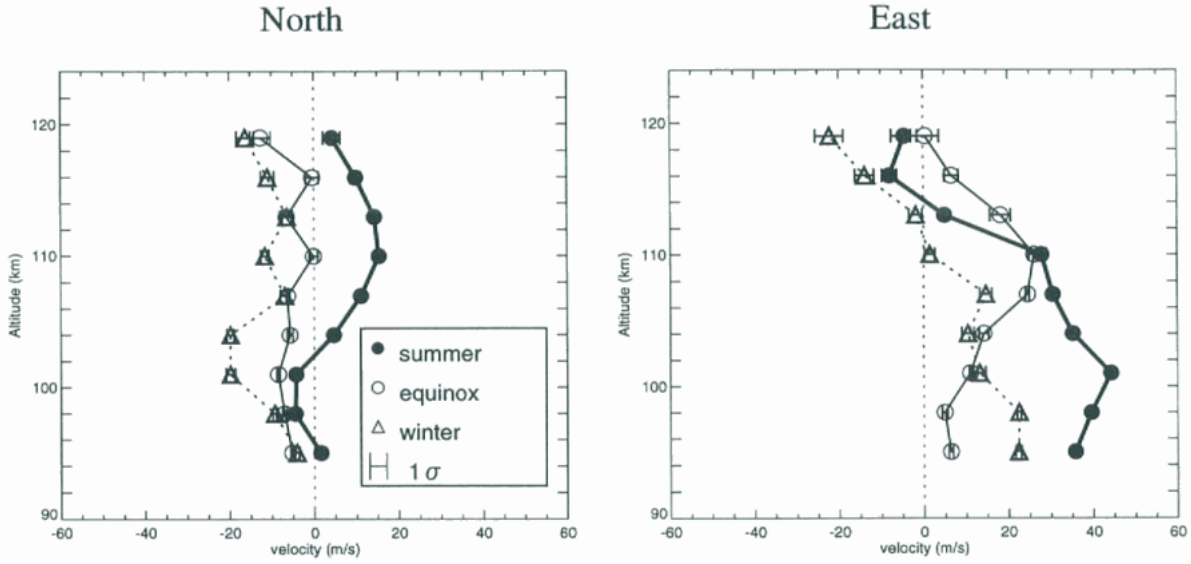

Figure 33: Seasonal variations in the horizontal mean wind. From winter to summer, the direction of the meridional mean wind changes from southward to northward, and the eastward amplitude of the zonal mean wind is enhanced.

119 km under geomagnetic quiet conditions (Ap<16) over a solar cycle between November 1986 and October 1996 have been studied. Data gathered over 56 days was analysed and grouped in order to investigate wind variations in different seasons and solar cycle conditions. Seasonal and solar cycle dependencies of mean winds as well as diurnal and semidiurnal amplitudes were found, Figure 33. Phase differences in the diurnal and semidiurnal components were less than two hours between seasons and solar activity conditions. Neither seasonal nor solar cycle dependence was found for the vertical component. Comparisons were made using model predictions and radar observations as well as UARS observations (Nozawa and Brekke).

Atmospheric Gravity Waves and TIDs

EISCAT VHF radar data (CP-6) on a total of 31 days between June 1990 and January 1993 have been used to investigate the vertical winds associated with gravity waves at mesopause heights. The data reveal a motion field dominated by quasi-monochromatic gravity waves with representative apparent periods of ~30-40 minutes, amplitudes of up to ~2.5 ms^{-1} and large vertical wavelength. Figure 34 presents a set of time-height vertical-velocity contours for 31 July 1992 which display these typical characteristics. In some instances wave activity appears to be confined to particular height ranges of ~10 km or less and to have approximately

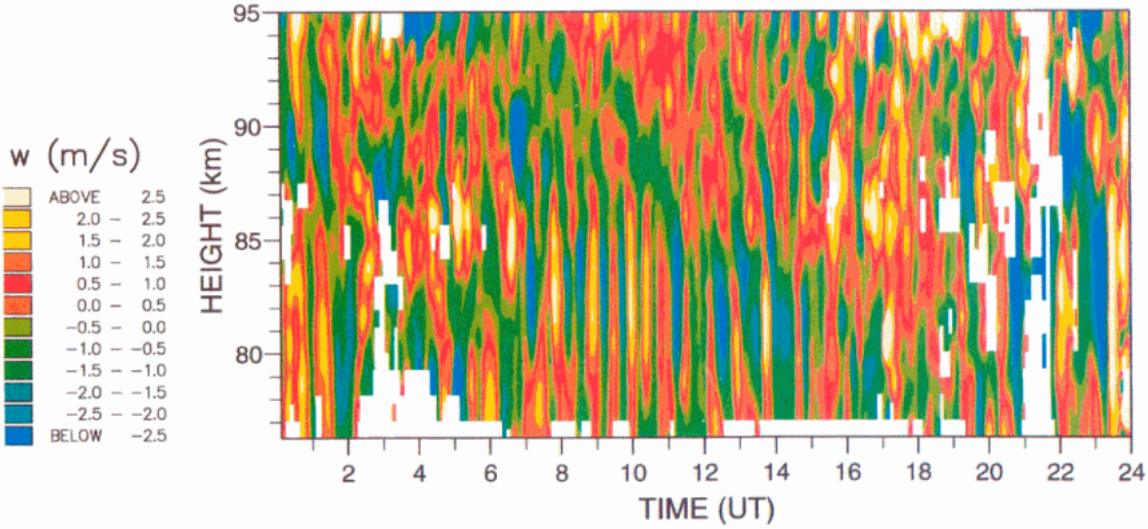

Figure 34: Time-height contours of vertical velocity for data recorded on 31 July 1992. The motion field is dominated by quasi-monochromatic gravity waves with periods from 30 to 40 minutes

Gaussian profiles of amplitude across that range - suggesting that the waves are ducted. An example of such a wave is evident at heights of ~78-88 km between about 0700-12:00 UT in Figure 34. Plausible ducting mechanisms include structures in horizontal wind and/or temperature which could not be addressed with the CP-6 data considered here, and so further studies are to be carried out in the hope of confirming the presence of such ducts (Mitchell and Howells).

Vertical profiles of the vertical-velocity variance display a great variety of forms suggesting the waves are propagating in a complicated and changeable environment. There is little indication of the systematic wave growth with height expected for simple energy-conserving ascending waves. However, daily-mean variance profiles evaluated for consecutive days of recording show that the general shape of the variance profiles often persists over several days, indicating that properties of the background atmosphere are involved in shaping the vertical structure of the wave field. The mean variance evaluated over a 10 km height range (used as a crude measure of total wave activity) has values from 1.2 m^2s^{-2} to 6.5 m^2s^{-2} and suggests a semi-annual seasonal cycle with equinoctial minima and solsticial maxima, in agreement with MF-radar studies of horizontal winds at middle and high latitudes.

The mean vertical-wavenumber spectrum provides a powerful diagnostic of a number of proposed theories of gravity-wave saturation. Such spectra evaluated for the EISCAT data at heights up to 86 km have a mean slope, k (spectral index), of -1.36±0.2, consistent with observations made in the troposphere and stratosphere by other techniques, but disagreeing with the predictions of the linear instability, diffusive filtering and saturated cascade theories advanced to explain gravity-wave saturation, which suggest k values near -3, +1 to +1.8 and +1 respectively. The possible presence of a population of ducted waves is suggested as an explanation for the differences between theory and observation. The spectral slopes evaluated for individual days have a range of values, and steeper slopes are generally observed in summer than in winter. The spectra also appear to be generally steeper on days with lower mean vertical-velocity variance.

Propagation characteristics of auroral TIDs have also been investigated with the help of CP-2 data. A newly developed technique using maximum entropy cross-spectral analysis allows the derivation of the apparent full wave number vector of the TIDs as a function of height. Figure 35 shows as an example for a TID in electron density with a wave period of about 72 minutes. It reveals a mean horizontal phase speed of about 180 ms^{-1} (corresponding to a horizontal wavelength of about 780 km) directed south-eastwards, and a vertical phase speed of 55ms^{-1} at an altitude of 300 km. This wave can therefore be characterised as a typical moderately large scale TID. The method turned out to be very successful for the determination of TID propagation parameters. (Ma and Schlegel)

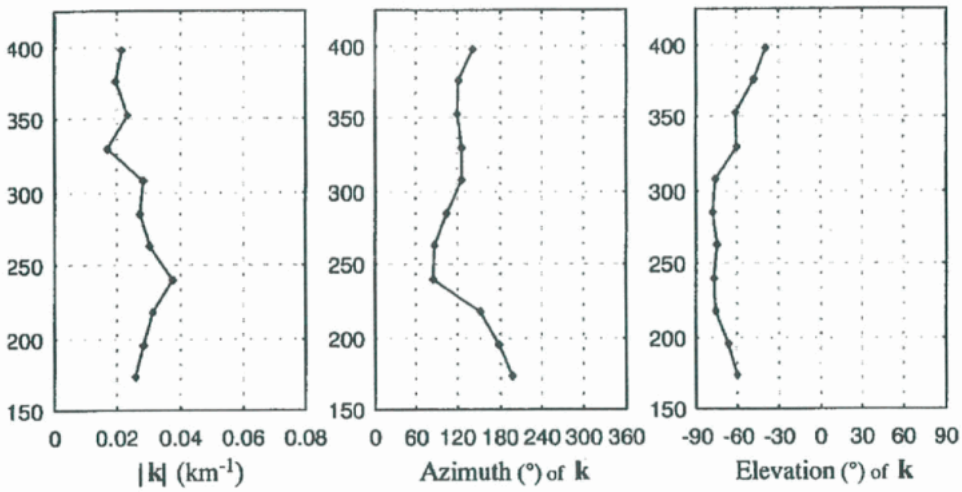

Figure 35: Height profile of the apparent wave vector of the TID in electron density of 14 Nov. 1990, having a wave period of about 72 minutes.

Quasi-periodic fluctuations in the ground-scatter returns from the SuperDARN network of auroral HF radars have been associated with the passage of medium-scale atmospheric gravity waves. Data from the CUTLASS Finland HF radar have been used to validate this capability experimentally. Variations in the range of the first significant power returns from the F-region have been shown to be a very sensitive indicator

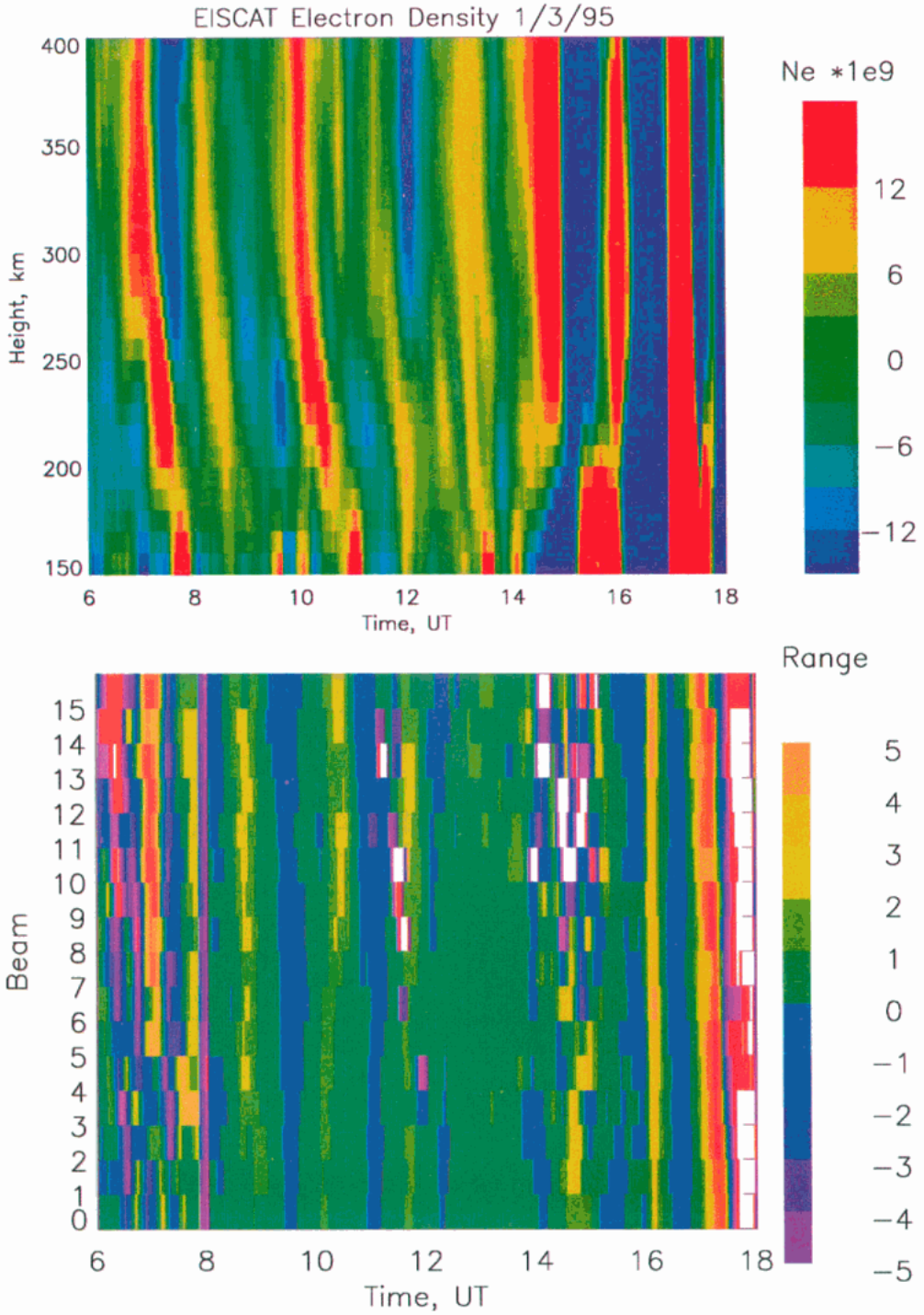

Figure 36: (a) Electron density profile from EISCAT CP-1 on March 1 1995 between 06:00UT and 18:00UT with a 15-60 minute band pass filter applied. (b) Variations in the distance to the first return from the Finland CUTLASS radar for the same interval applying a 15-60 minute filter. The beams rotate clockwise from west to east of Tromsø with beam 5 pointing directly towards it.

of gravity waves and this parameter has thus been adopted in the study. Figure 36 show a direct comparison of 15-60 minute waves in both the EISCAT and CUTLASS Finland radar data for March 1st 1995. Note that the former measures variations of electron density with height, whilst the path shape for the latter is the shallow horizontal arc made by beam number five pointing towards Tromsø. Excellent agreement was obtained for an effective reflection height of 235 km. Further improvements were obtained by introducing a delay to account for the propagation time from Tromsø to the CUTLASS first return. This allows the phase speed of the gravity waves in the EISCAT-CUTLASS direction to be inferred (Arnold et al. 1997).

Spectral and wavelet analysis of spatially and temporally coincident time series of CUTLASS ground scattered power and EISCAT measurements of electron density and line-of-sight velocity have also been undertaken.

This work has been supported by ray tracing simulations and has revealed a reasonable correlation between the observations from the two systems during the periods under consideration.

The CUTLASS Lomb periodogram of detrended ground scattered power and the Lomb periodogram of detrended EISCAT electron density are very similar with significant peaks centred on 0.07 mHz and 0.17 mHz. The cross-correlation function peaked at 0.83 with ground scattered power lagging electron power by six minutes. The wavelet maps show similarities in the wavelet level centred on 0.18 mHz but are distinctly different at higher levels.

Coupling Between the Thermosphere, Ionosphere, and Magnetosphere

Electromagnetic energy flows from the magnetosphere into the ionosphere and thermosphere. The flux is given by the product of current and electric field, **J·E** (Poynting's theorem). This energy gets partially dissipated in the thermosphere by resistive Pedersen currents. The corresponding Joule heating rate is **J·E′**, where **E′=E+U×B** is the electric field in the neutral frame. **U** is the neutral velocity, **B** the geomagnetic field. Often neglected is the transfer into mechanical energy by acceleration of the neutral atmosphere. In addition to this ion drag, the atmospheric gas experiences other forces like pressure gradients due to solar radiation or auroral heat sources, and the Coriolis force. Therefore the neutral atmosphere can sometimes also drive a ionospheric dynamo. The mechanical energy transfer rate, **U·(J×B)** is negative when the

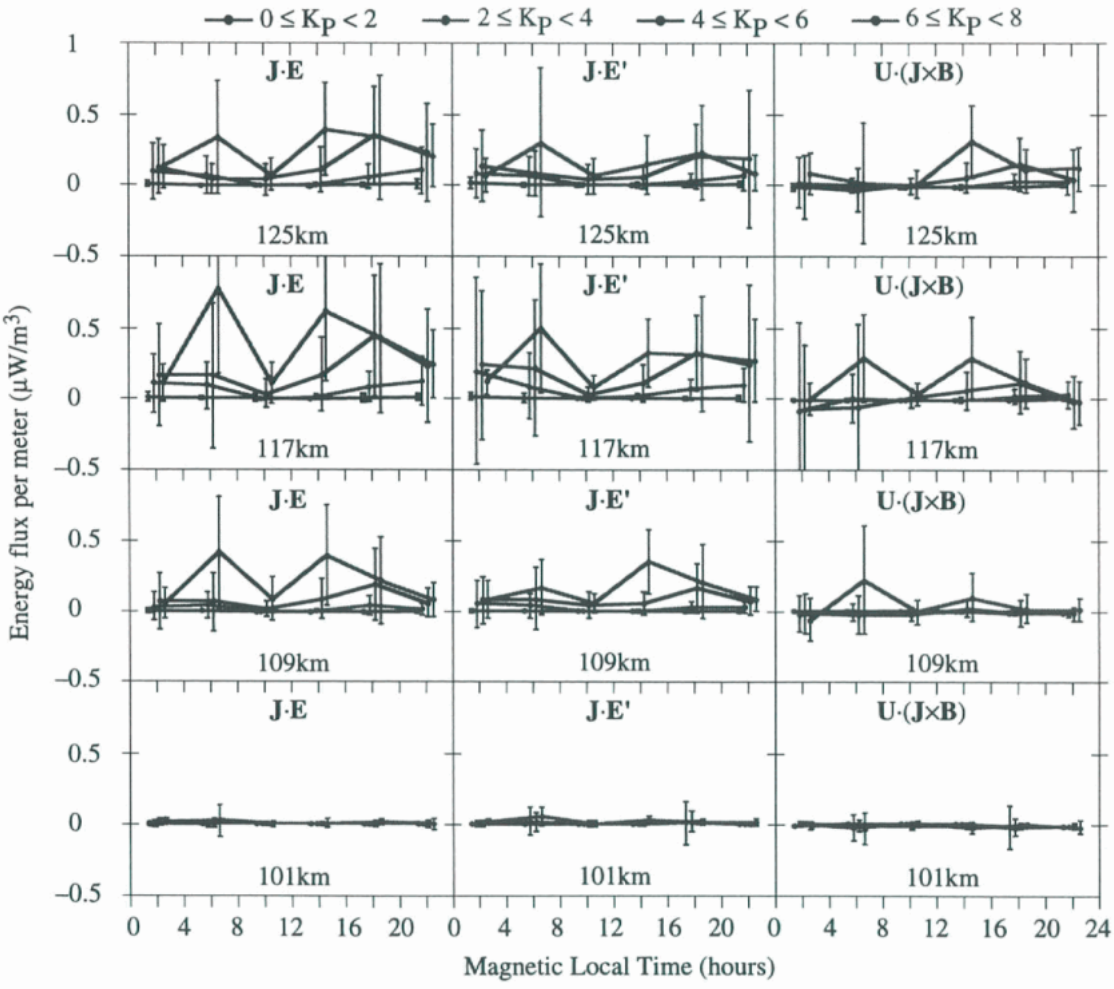

Figure 37: Electromagnetic energy flux, Joule heating rate, and mechanical energy transfer rate (panels from left to right) at four different altitudes, 101 km, 109 km, 117 km, and 125 km (panels from bottom to top). The curves in different colours indicate different levels of the Kp index.

atmosphere acts as a dynamo, and positive, if the neutrals get accelerated. These three energy rates, electromagnetic flux, Joule heating and mechanical transfer, are key parameters for establishing the energy balance between thermosphere, ionosphere, and magnetosphere.

Energy rates have been evaluated quantitatively using the CP-1-H experiment. This provided directly, or indirectly, all parameters at altitudes of 101, 109, 119, and 132 km. The results are shown in Figure 37:

1. At all altitudes the electromagnetic energy input was distributed to both Joule heating and mechanical energy. The energy going into Joule heating was greater than that transferred to the mechanical energy, but the latter energy is generally not negligible.
2. All three energy rates have maxima (two) in the dusk region relative to the midnight region.
3. The enhancements in all rates go together with an increase in geomagnetic activity represented by the Kp index.
4. The electromagnetic energy transfer rate was greatest at 117 km height and decreased at lower altitudes. It was usually positive but occasionally negative. At 117 km the mechanical energy transfer rate was lower than the electromagnetic energy transfer rate, suggesting that most of the electromagnetic energy at this altitude is converted to Joule heating and only a small portion goes into mechanical energy. At 125 km, the mechanical energy transfer rate was higher than at 117 km. On average, about 65% of the input electromagnetic energy was converted to Joule heating and 35% to neutral mechanical energy. At 109 and 101 km altitude the mechanical energy transfer rate became negative. There also the Joule heating rate was greater than the electromagnetic energy transfer rate, and not only the electromagnetic energy but also the atmospheric dynamo contributed to Joule heating (Fujii, Nozawa, Matuura and Brekke).

Ion frictional heating constitutes one of the principal mechanisms whereby energy originating in the solar wind is deposited into the Earth's ionosphere and ultimately the neutral atmosphere. A statistical study of ion frictional heating based on more than 4000 hours of observations from EISCAT CP-1 and CP-2 has been completed. The selection criterion adopted to identify intervals of frictional heating required an enhancement in the field-parallel F-region ion temperature exceeding 100 K over two or more consecutive integration periods. This corresponds to an ion velocity of approximately 500 ms^{-1}. The diurnal distribution of ion frictional heating observed by EISCAT established by this method is subsequently classified according to the prevailing interplanetary magnetic field (IMF) orientation and geomagnetic activity. The results are interpreted with reference to corresponding distributions of enhanced ion flow. The orientation of the IMF profoundly influences the occurrence distribution of ion frictional heating which is explained by an analogous effect on the distribution of enhanced ion velocities, i.e. those exceeding 500 ms^{-1}, Figure 38. The histogram represents the percentage occurrence of enhanced ion velocities (and hence frictional heating) as a function of universal time, with a bin width of 30 minutes, and the line plot indicates the number of observations of each half hour bin. Under conditions of negative z-component, the occurrence of frictional heating greatly exceeds that for a positive z-component. Further sub-classifying according to By reveals asymmetries in the proportion of ion frictional heating associated with the eastward and westward convection cells (Davies et al. 1997a).

The data set collected during the Ion-Neutral Dynamics Investigation (INDI) now contains many hundreds of hours of simultaneous EISCAT and FPI data spanning a period of 13 years. Recent work has shown the value of the O^+-O collision parameter calculated from such data is very sensitive to the statistical methods employed. The most accurate method, that of Maximum Likelihood Analysis, requires a detailed analysis of the errors in all the parameters involved (Daniell, Davis and Aylward).

Earlier works have studied quiet or moderately active auroral arcs, which are the basic feature of the three-dimensional current flow and particle exchange between the ionosphere and magnetosphere. The ionosphere behaves in a far more complex manner than just being a passive detector of magnetospheric precipitation. In response to localised primary magnetospheric particle precipitation a reaction of the ionospheric plasma leads to the build-up of strong electric fields adjacent to regions of high conductivity, thus allowing three-dimensional current systems to close. Indications for the extraction of cold ionospheric electrons as carriers of downward field-aligned current were found. In other cases instabilities were observed in the topside ionosphere, above auroral precipitation, which are responsible for an affective upward acceleration of ionospheric ions. Early observations of topside ionospheric turbulence and associated oxygen outflow to the magnetosphere were addressed in more derailed follow-up studies. It was shown that the backscatter cross sections in the EISCAT

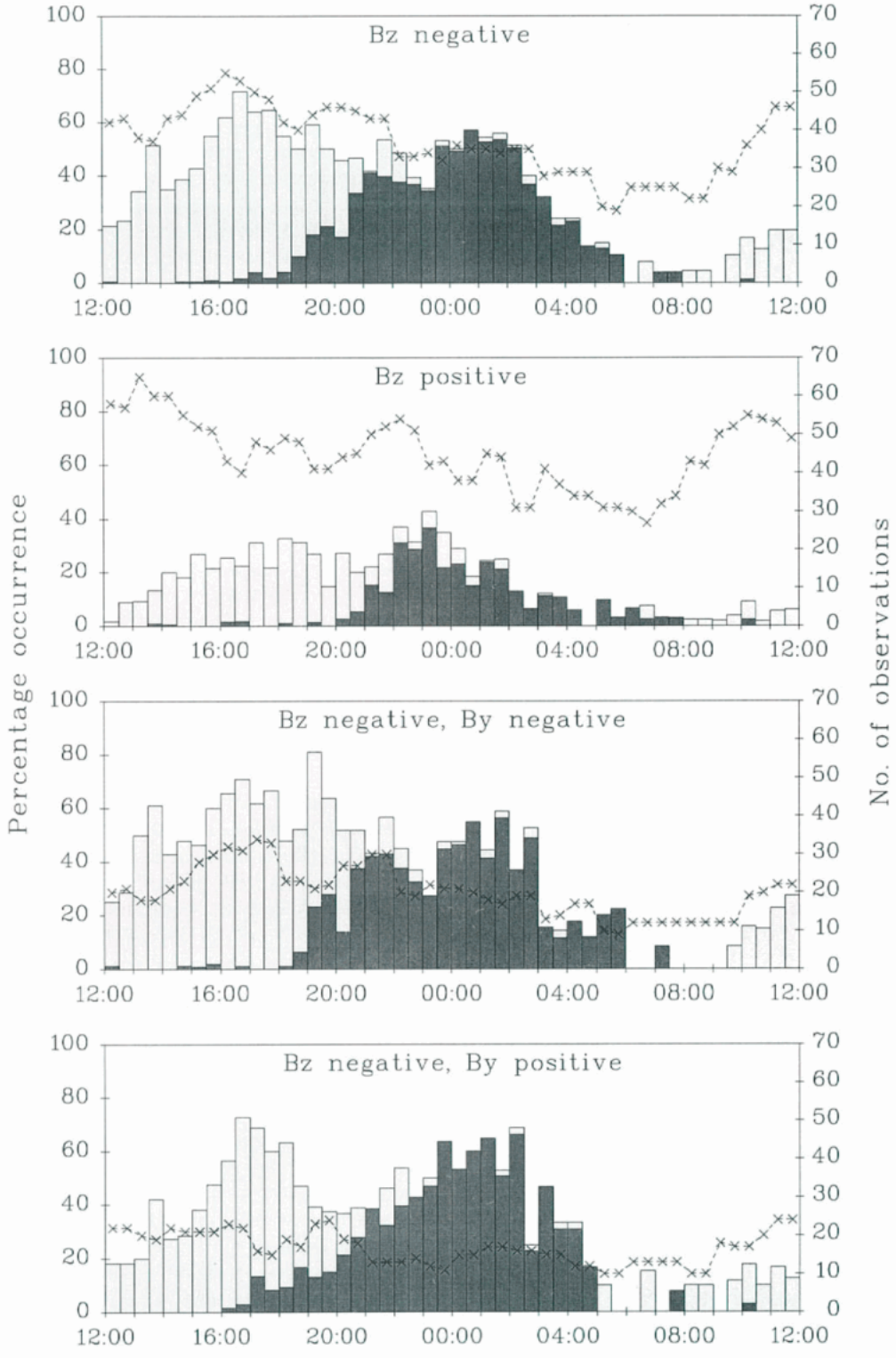

Figure 38: Variation of the diurnal distribution of enhanced ion velocities, with the orientation of the y and z components of the IMF.. Light grey shading indicates velocities with a westward zonal component, dark grey indicates those with an eastward zonal component

UHF and VHF radars were different during periods when anomalously enhanced topside ionospheric radar echoes were recorded and that anomalous echoes can also be produced by very strong perpendicular electric fields, possibly indicating standing Alfvén waves above auroral structures (Cabrit et al., 1996, Forme, Fontaine and Persson).

Storms and substorms

The geomagnetic storm of January 10, 1997 was remarkably in two ways. It was the first major storm of the new solar cycle no. 23 and it was for the first time successfully predicted, since the causing agent, a strong coronal mass ejection was observed four days earlier from instruments on the SOHO spacecraft. Fortunately EISCAT was running in the CP-2 mode until 16:00 UT on January 10, and captured the major part of this storm. Although the data quality was not very good because of the typical low ionisation during a winter day, many interesting results could be derived from the measurements. A composite showing conductivities, electric fields, current densities and ion and electron heating is shown in Figure 39. It shows the typical features of a strong but not exceptional storm. The conductivities in the first panel show enhanced values between 04:00 and 12:00 UT, typical for particle precipitation due to high energy particles between 04:00 and 09:30 UT as shown by the conductivity ratio in panel two. In the third and forth panels the electric field in magnitude and direction is displayed showing enhanced values in the afternoon. Before about 08:00 UT the Sodankylä station was not in operation, therefore tristatic measurements could not be performed. A few isolated values (because of poor snr) could be inferred from the three different beam directions applied in CP-2. The current density plotted in the fifth panel shows high values in the afternoon as the electric field does. The sixth panel shows enhanced ion temperatures (averaged between 120 and 135 km altitude) due to Joule heating during the same period. Also, the enhanced electron temperatures (averaged between 105 and 115 km height) shown in the lowest panel which originate from the two stream plasma instability, are well correlated with the electric field. An analysis of the solar wind parameters during the storm revealed that a total energy of 57000 TJ was transferred from the solar wind to the terrestrial magnetosphere. This number can be compared with the energy dissipated in the auroral zone over Northern Scandinavia (time integral over the derived Joule heating) of 6.5 TJ. This fraction of about 0.01% is lower than the global average. The storm effects were apparently stronger over North America (Schlegel and Collis).

The further development of quiet auroral arcs into auroral break-ups was addressed in quite a number of studies. Observations of initial activations ("pseudo break-ups"), the formation of unstable structures, characteristic auroral drifts and the exact location of the final break-up with respect to magnetospheric boundaries have given valuable information on the magnetospheric

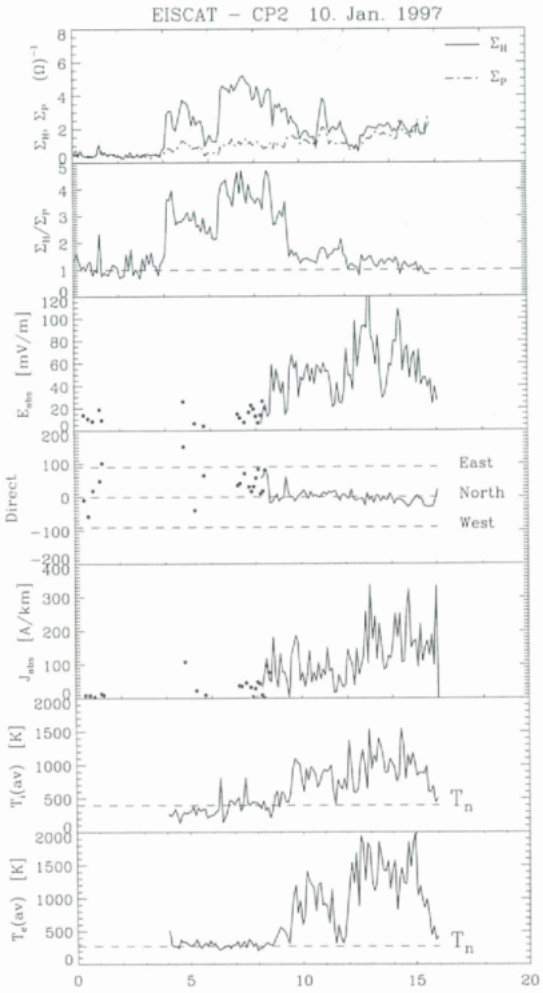

Figure 39: Electrodynamic parameters derived from EISCAT measurements during the January 10, 1997 storm.

source mechanisms of the observed processes. Using co-ordinated EISCAT and Freja data with observations from geostationary satellites, all-sky cameras and magnetometers, indications were found that the ionospheric ion outflow during the substorm growth phase could modify the near-Earth plasmasheet oxygen content. The search was continued for signatures of enhanced oxygen ion composition in the near-Earth magnetosphere during the substorm growth phase and during multiple substorm infections by using data from the CRRES and AMPTE satellites. More detailed studies of ion outflows from the relatively low altitude satellite Akebono have also been initiated. (Gazey. et al., 1996; Kauristie et al., 1996, 1997; Olsson et al., 1996a,b; Olsson, 1997; Andersson, Baker, Blomberg, Daglis, Eliasson, Fälthammer, Fox, Frank, Friis-Christensen, Gazey, Gjerloev, Grande, Greenwald, Huuskonen, Johnson, Karlsson, Kauristie, Kubyshkina, Lepping, Lester, Lindqvist, Marklund, Mukai,

Murphee, Nakamura, Opgenoorth, Pulkkinen, Reeves, Sergeev, Sigwarth, Singer and Zanetti).

Careful analysis of EISCAT data from the very rare times when the initial substorm onset takes place right overhead the radar has revealed characteristic differences in the energy of substorm precipitation during the early and later

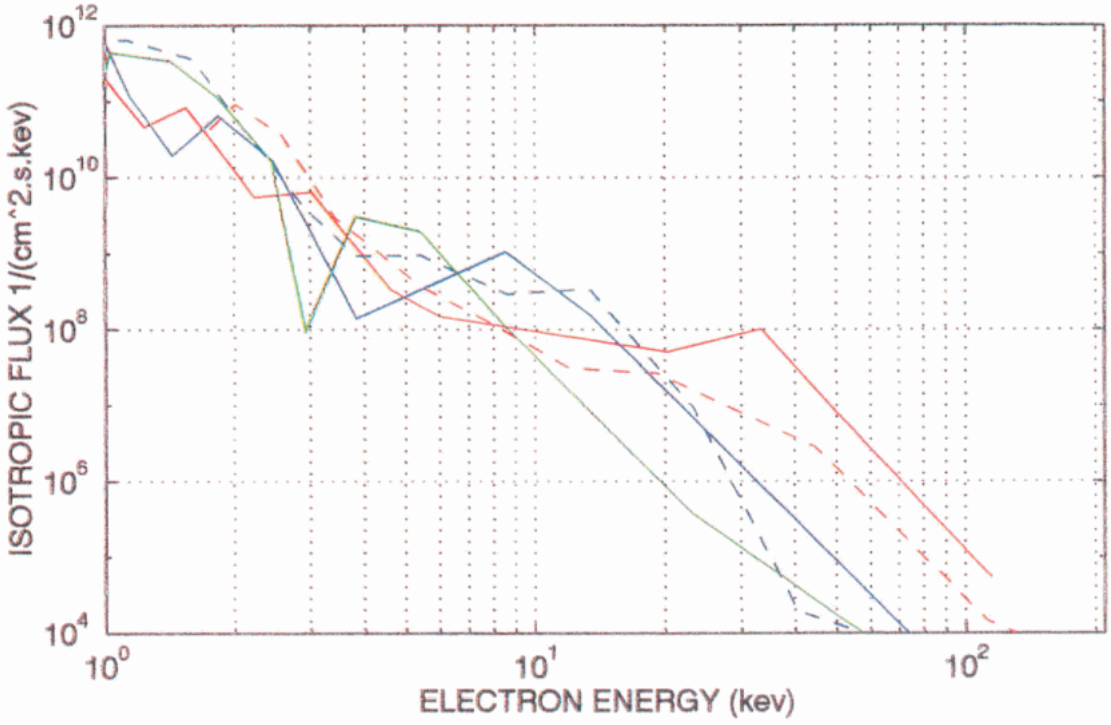

Figure 40: Electron spectra obtained using the SPECTRUM algorithm (Kirkwood and Osepian, 1995). Onset 861005 (red), onset 920127 (dashed, red), WTS 930124 (blue), WTS 930125 (dashed blue) and ARC 930125 (green)

phases of the substorm expansion. The electron density profiles observed by EISCAT have been converted into energy spectra of the precipitating electrons. The results indicate that the acceleration in the magnetospheric source region and along the magnetic field lines differs in westward travelling surges, i.e. later expansion phase features, and initial onsets. The magnetospheric plasma parameters such as source region electron density and temperature can be derived indirectly from the EISCAT data. Since the precipitating electron spectra can only be indirectly induced from EISCAT altitude profiles of electron density, Freja satellite data has been used during substorm onsets in a "space-truthing" follow-up study. Even in this data set, the so-called "current-voltage relation" which is typically observed in association with field-aligned accelerated electrons in auroral arcs still bolds for the very high energies (>20 keV) observed during onsets. In the resulting electron spectra, Figure 40, it is interesting to notice that although the intensity in electron density varies between the two onset events, the characteristic spectral precipitation pattern is the same. The same tendency can be seen in the two WTS case studies. This implies that the electron density is significant for the determination of the intensity of the flux while the characteristic shape of the flux-energy spectra depends on the depth of electron precipitation. The potential drop through which the precipitating electrons have been accelerated along the field line can be determined from the electron spectra and a large difference in acceleration energies between auroral break-ups and WTS is observed. In the onset events potential drops of the order of 20-30 kV are estimated while in the WTS cases it is around 10 kV. It was also found that the Hall and Pedersen conductance ratio in the onset events was twice as high as in the WTS events and also more than twice the maximum values found in earlier reports (Olsson et al., 1996a,b, 1997).

A multi-instrument study involving Wind, Geotail, Interball and a global network of ground-based stations showed that the influence of solar wind variations on magnetospheric processes is much more direct than previously anticipated, and that, for example, moderate changes in the solar wind density under conditions of southward directed IMF could not only initiate, but also

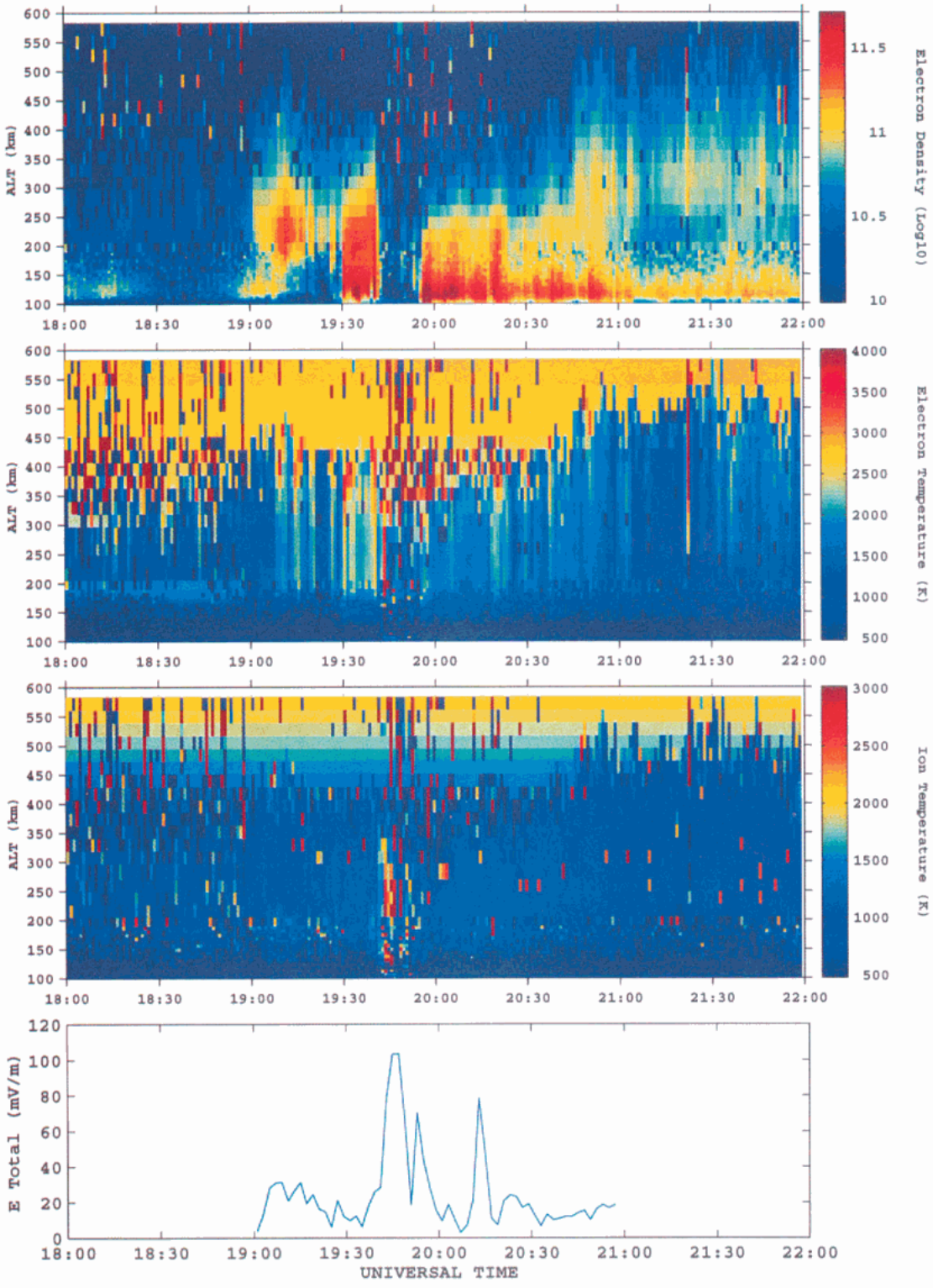

Figure 41: Ionospheric plasma parameters from 1800 to 2200UT, November 17, 1996, measured by the EISCAT UHF facility along the magnetic field at Tromsø

quench substorm expansion. Figure 41 shows that, after a southward turning of the IMF at around 18:45 UT, electron density enhancements near 120 km first become visible at about 18:50 UT and intensify around 19:00 UT when a faint southward drifting growth-phase arc enters the EISCAT UHF beam. After 19:30 UT some very energetic precipitation suddenly reaches the EISCAT beam, resulting in ionisation down to altitudes of 90-95 km. The implications of these

results on our understanding of the substorm mechanism has been further developed. (Eglitis, Karlsson, Kauristie, Lockwood, Nakamuru, Opgenoorth, Pulkkinnen, Syrjäsuo, Reeves and Romanov).

Three major ISTP campaigns for co-ordinated observations during interesting passages of the Interball, Geotail, Polar and Fast satellites over the northern Scandinavian ground-based networks took place in December 1995-January 1996, October 1996-April 1997, and October 1997-April 1998. In particular the operations in association with the Fast satellite were part of the International Auroral Study (IAS) for which a newly designed digital All-Sky camera was at installed Abisko and operated during the winters of 1996/97 and 1997/98. During these intense campaigns, utilising several 100 hours of special and common EISCAT operation time, a wealth of data bas been collected. Several events, amongst those two Solar coronal mass ejections on January 6-11 and April 6-11 have been selected for more detailed studies within international consortiums for initial studies of the complicated solar wind magnetosphere coupling in the forefront of one of these CME's. (Clemmons, Collier, Escoubet, Fairfield, Giles, Johnson, Laakso, Lepping, Lin, Maynard, Mozer, Opgenoorth, Pfaff, Phan, Scudder Sibeck, Singer, Tsuruda, and Wygant).

Most of the above studies dealt with the night-side magnetosphere, however, the day-side magnetosphere is another prime region for important satellite and ground-based co-ordinated observations which will gain more and more attention. The day-side magnetosphere and its boundary with the shocked solar wind flow (the magnetopause) is a very active system, where mass, momentum and energy is extracted from the interplanetary medium and transferred to the ionosphere and the upper atmosphere. The mechanism responsible for this coupling is believed to be a merging of interplanetary and geomagnetic field lines by magnetic reconnection, thereby establishing magnetic funnels in both polar regions (the polar cusps) where solar wind panicles may enter the magnetosphere and produce the day-side aurora. It should be noted that with the advent of Cluster four-point measurements (expected in the early part of the next century) our research will be able to contribute new and increased insight in one of the most interesting and poorly understood processes in plasma research, namely magnetic reconnection: this process is not only active in solar - terrestrial physics (both on the day and night-side of the magnetosphere) but also has implications and applications in other branches of physics (e.g. astrophysics and fusion research) (Opgenoorth and Lockwood, 1996).

In preparation for future Cluster/ESR/CUTLASS studies of the day-side cusp and very high latitude night-side substorm processes with such combined datasets, initial studies have been made using the Canadian/Icelandic SuperDARN radar pair and the Söndrestromfjord incoherent radar system on Greenland, during close passages of the Freja satellite. Very interesting relations between transient magnetic and radar disturbances were found in association with soft precipitation, which could be related to a total reorganisation of the magnetosphere in fast response to changes in the IMF By component. Initial data show that the response of the day and night-side ionosphere to global changes in the solar wind is very direct. Several initial studies using Geotail, Interball, ESR and the global SuperDARN network are under way (Persson et al., 1996; Eglitis and Pitout).

Day side phenomena, such as the above described transients in response to changes to the interplanetary magnetic field (IMF) By-component, but even more so very short-lived transients typically observed during periods of southward directed IMF, require high time resolution measurements with ground-based radars. Satellites often encounter either only one or none of these transients without possibilities to observe the repetitive nature of these phenomena. Considerable effort has been spent in improving the possibilities of making high time-resolution radar measurements in the very high latitude ionosphere. Similar measurements will in future be important when analysing the relative importance of small scale processes at the day-side magnetopause and in the vicinity of the exterior Cusps, as observed by Geotail, Polar and Cluster.

The most common concept of ground-based data is to gather similar data from many individual stations to form a network. However, different types of data can be complementary to each other, i.e. the combined scientific value of such data can be raised by combination in a proper and predetermined way. For this purpose, a co-ordinated multi-instrument ground-based array MIRACLE (Magnetometer, Ionospheric Radar, All-sky Camera Large Experiment) has been established, which comprises a magnetometer network, two coherent radar systems on HF (CUTLASS) and VHF frequencies (STARE), and a network of digital all-sky cameras, all surrounding the EISCAT facilities in Norway, Sweden and Finland. With the help of KVA grants in 1996 and 1997, parts of the Russian arctic magnetometer network in the Kara sea have been revived and now deliver data to MIRACLE from Heiss Island and three other remote locations in the Russian arctic. The idea of

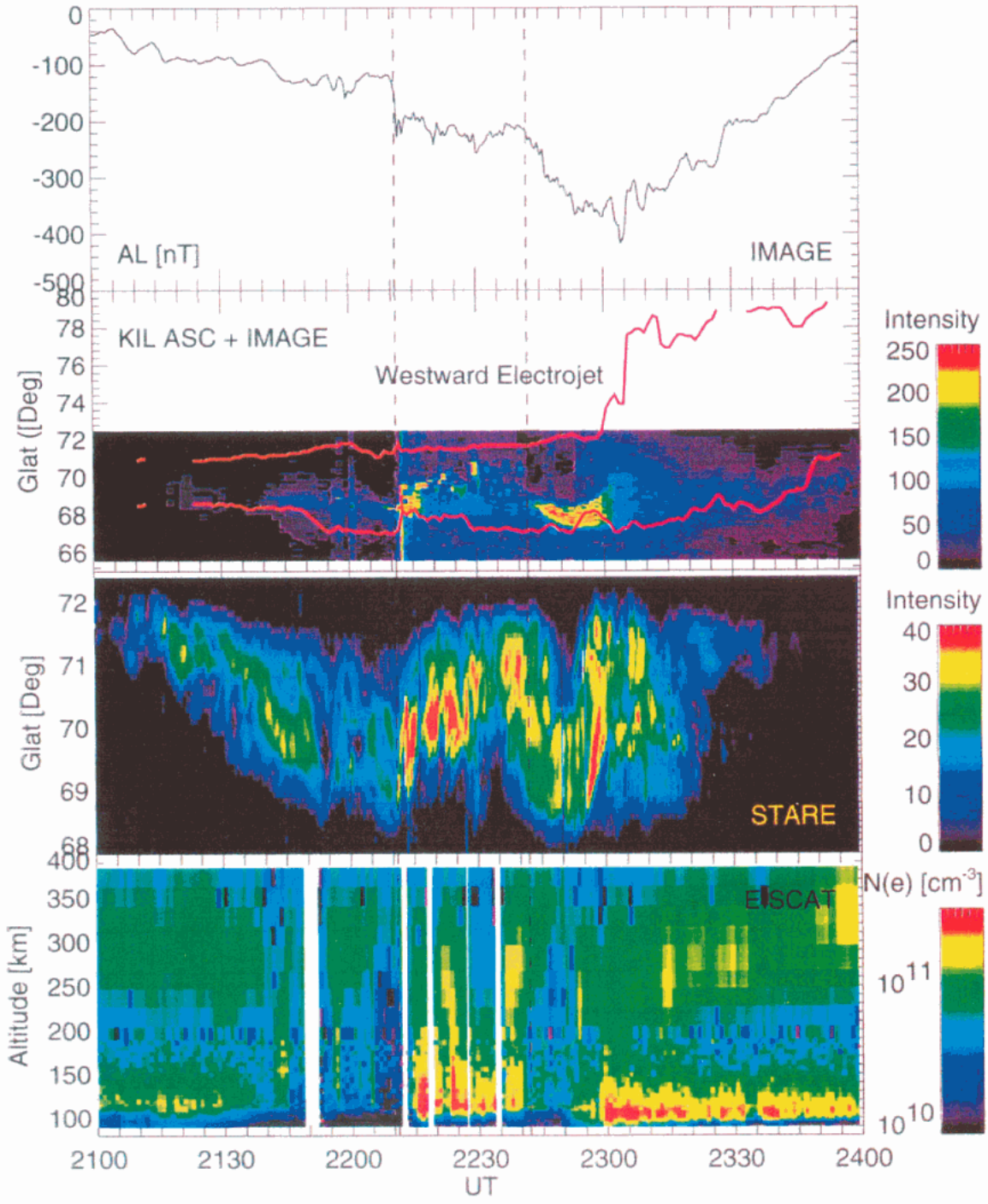

Figure 42: MIRACLE display for November 3, 1997. Panels from top to bottom show local AL-index constructed from IMAGE magnetometer data, keogram from KIL ASC (with westward and eastward electrojets indicated by solid lines), backscatter intensity v. latitude from the STARE radar in Norway and Electron density v. altitude from EISCAT

MIRACLE is to deliver multi-instrument data in a predetermined identical two-dimensional format to the international community via WWW. This will hopefully optimise the scientific application of such data even for non-specialist users, as e.g. the satellite community. With the help of two-dimensional magnetometer data (CURRENTS), two dimensional radar data (E-FIELDS), and two dimensional images (CONDUCTIVITY), this will provide a handle on all parameters of the two-dimensional Ohm's-law of the ionosphere. Based on a certain over-determination and the use

of proper two-dimensional data handling, this dataset will allow conclusions to be drawn concerning the true three dimensional coupling mechanisms between the ionosphere and the magnetosphere. MIRACLE, Figure 42, became fully operative in late 1997, and the first data is under investigation (Amm, Eglitis, Janhunen, Karlsson, Kauristie, Nielsen, Opgenoorth, Pellinen, Pulkkinnen, Syrjäsuo, Viljanen, Wallman and Thomas).

A major recent advance has been the theoretical prediction of a phenomenon which has become known as "substorm quenching". This prediction came from the realisation that changes in the solar wind density can increase or nullify lobe field increases caused by excess magnetopause reconnection voltage. The sum of the solar wind thermal and dynamic pressures acts to compress the tail and so influences the magnitude of the lobe field and the cross-tail current. As a result, compression of the magnetosphere can trigger onset of substorm expansion phases at almost any point in a growth phase. A major decompression of the magnetosphere can quench the expansion phase. Recent observations confirm that this quenching can indeed occur and the signatures have been identified in a variety of observations used to monitor substorms. These include a major solar wind density increase seen by WIND, IMP-8 and GEOTAIL which impacts the magnetosphere immediately after a substorm expansion phase onset, a decompression of the magnetosphere seen by GEOTAIL, a quenching of the expansion bulge aurora, an unusual sudden end to geostationary injections, an onset of rapid convection inside the quenched bulge seen by EISCAT, and a decay of the lobe field at X=-28 RE seen by INTERBALL which is quantitatively consistent with the solar wind density decrease. This newly identified phenomenon raises a host of interesting questions which will be addressed in future studies (Lockwood and Opgenoorth, 1997).

A key point about this effect is that it offers a means to differentiate between the two major mechanisms proposed for substorm onset, namely the current-disruption (CD) model and the near-Earth neutral line (NENL) model. The latter has recently been modified because onset signatures are now known to be considerably closer to the Earth than where the NENL has been seen to form. Figure 43 shows two schematics which illustrate these ideas and how the development of the decay in the aurora is different in the two models. For the CD model the aurora forms at the equatorward edge of the expansion bulge and

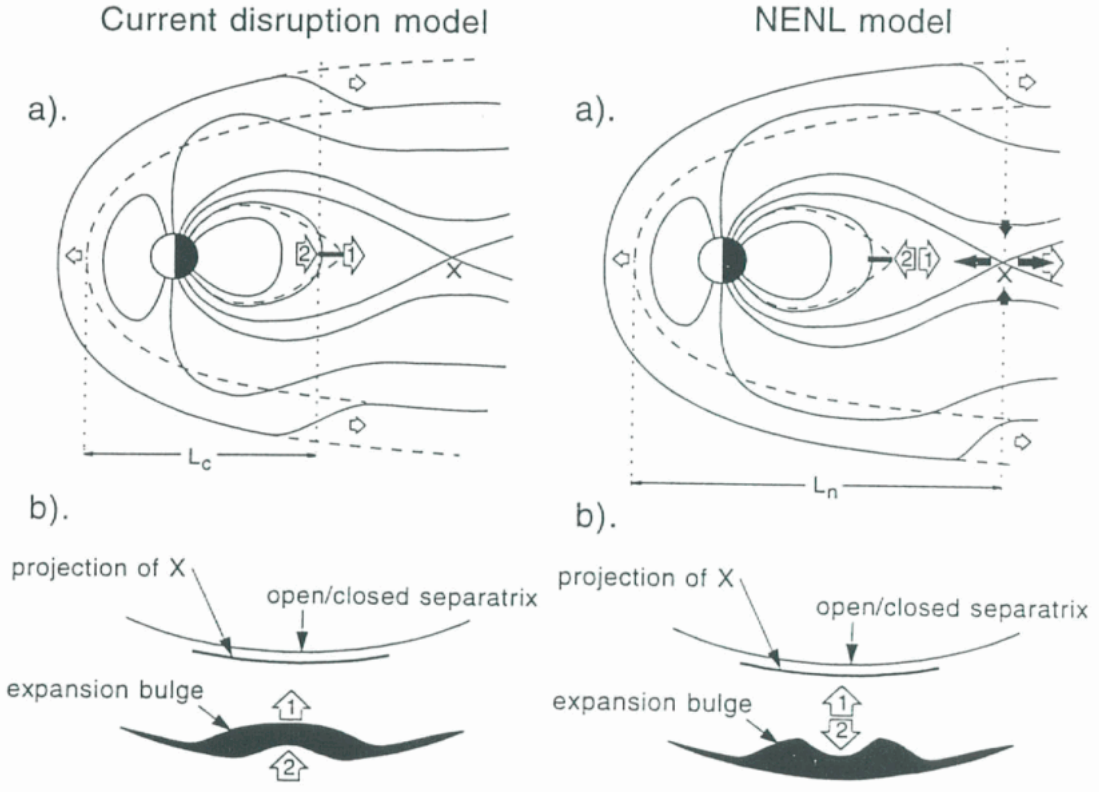

Figure 43: Schematic illustration of the concept of substorm quenching, applied to two rival models of substorm expansion onset, namely the synthesised current disruption model (CD, left) and the modified near-Earth neutral line model (NENL, right).

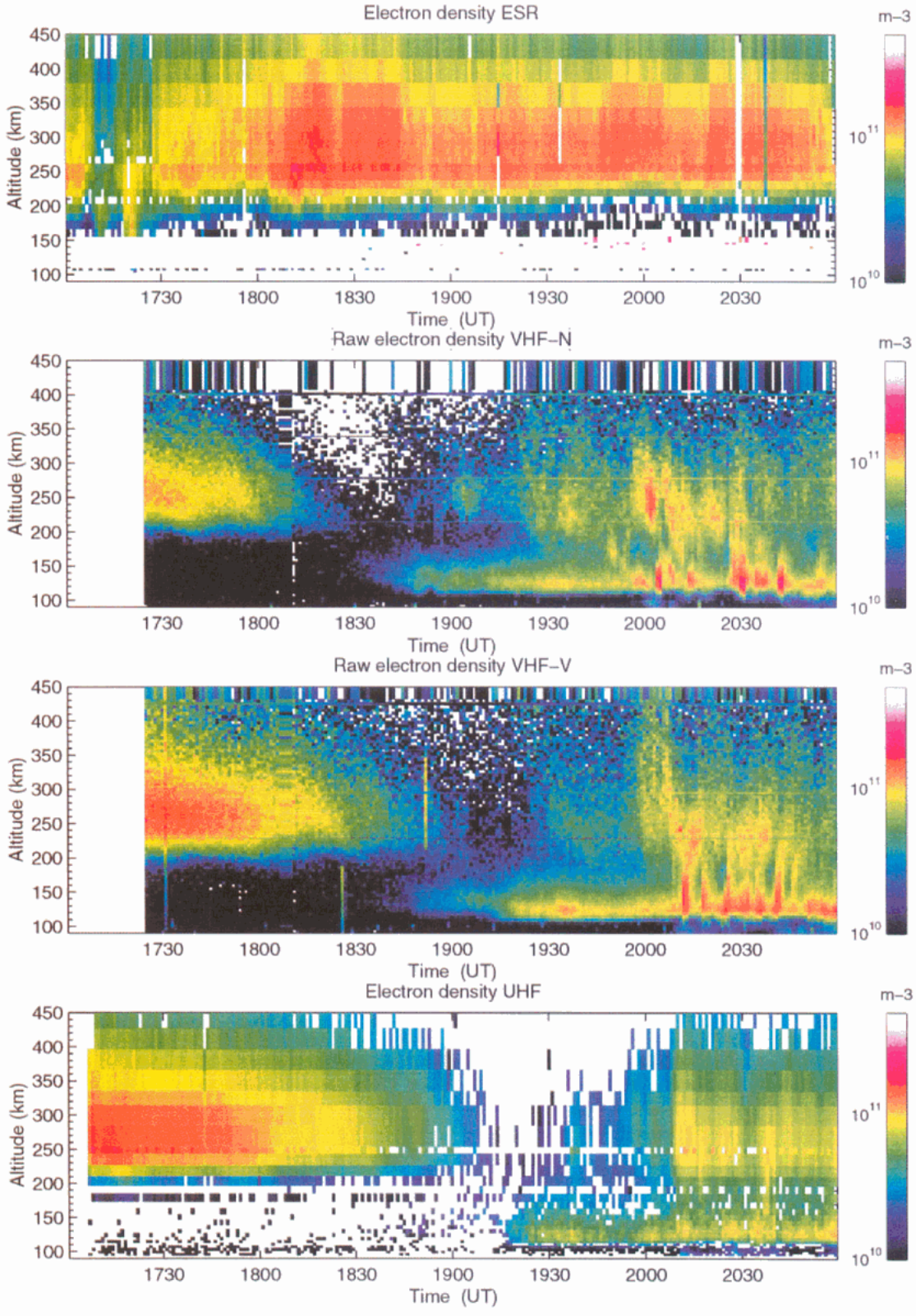

Figure 44: Ne profiles from the EISCAT Svalbard, VHF (two beams) and UHF radars, 14 March 1997.

propagates poleward as the decrease in the tail lobe field propagates away from the Earth down the tail. In the NENL model it forms at the poleward edge and propagates equatorward as the effect of the reduction in reconnection rate at the NENL propagates Earthward. The lag is longer for the NENL model and there are also differences in the predicted response of the ionospheric convection. The first identified set of observations of a quenching were consistent with the NENL model and inconsistent with the CD model (Lockwood and Opgenoorth, 1997).

The Ionospheric Trough

The International Auroral Study (IAS) created a broad observational activity all over the world, both ground-based and from space, in winter 1996/1997. One key element of the IAS was the FAST spacecraft, which is a part of the NASA Small Class Explorer program. As the footprint of this satellite passed close to Tromsø on March 14, 1997 at 17:41 UT, all the three EISCAT radars - the EISCAT Svalbard radar (ESR) located at the site Longyearbyen at Svalbard and the EISCAT mainland UHF and VHF radars in Kiruna, Sodankylä and Tromsø - in Northern Scandinavia were measuring. The ESR was running a common program test mode and the mainland radars were running in a configuration allowing three almost meridional power profile measurements from about 20° north, vertical and 13° south aligned along the geomagnetic field over Tromsø. In this experiment the VHF radar was divided into two 224 MHz sub-radars by pointing two of the four antenna sections north at 70° elevation and two of them vertically. For these beams electron density power profiles were measured from 80 to 400 km range and long pulse ACFs were measured from 200 to 500 km range. Figure 44 shows the electron density profiles for the ESR (uppermost) and UHF (lowest) radars and the raw electron densities for the VHF (mean panels) radar beams. A signature of the main ionospheric trough is observed passing through all the four radar beams. The ESR shows an electron density depletion throughout the altitude range starting at about 17:10 UT. Due to the long distance from Svalbard to the mainland radars, it takes about 50 minutes before the signature can be observed at the northward pointing VHF half-beam in the second panel. The distance between the two VHF radar beams at the trough observing altitudes in F-region is around 100 km and between the vertical VHF and magnetic field aligned UHF beam about 60 km. The trough signature appears in the two VHF beams with 30 minutes time intervals at 18:00 and 18:30 UT and 10 minutes later at 18:40 UT in the UHF beam.

Research on the geophysical mechanisms responsible for trough formation has been carried out using observations made at a time of extreme geomagnetic quiet. The results demonstrated unambiguously that the structure of the poleward wall of the trough is related to energy input from localised, transient soft-particle precipitation, characterised by latitudinally narrow, field-aligned bursts of enhanced electron temperature. The apparent equatorward advance of the trough wall follows as a dynamic response to the movements of the edge of this structured precipitation. This study demonstrated conclusively that the boundary blob surmounting the trough wall is not simply a reconfigured polar-cap patch, as had been suggested by a previous modelling study. The field-aligned nature of both the poleward wall seen in plasma concentration and the localised enhancements in electron temperature measured by the radar enable estimates to be made of the inclination of the geomagnetic field at F-layer heights above EISCAT. Values were obtained in agreement with those predicted by the IGRF90 model to within the error estimates (Jones et al., 1997).

A study has been carried out in which the EISCAT Common Programme data has been searched systematically in order to find the simultaneous occurrence of high ion temperature and depleted electron density characteristic of a high latitude trough. These features are believed to arise when frictional heating in a narrow convection channel acts to increase the recombination rate, which in turn depletes the F-region density.

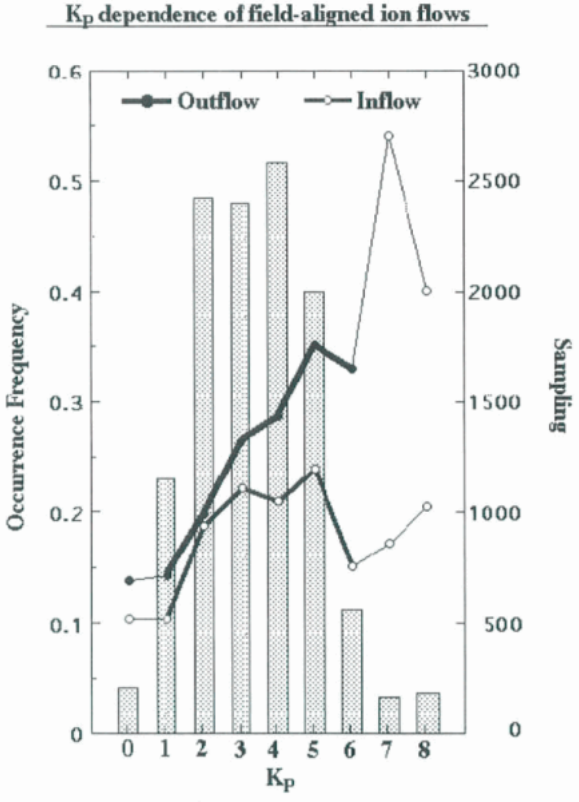

Figure 45: The KP dependence of the ion outflow and inflow for all MLTs.

Topside Ionosphere

Ten experiments co-ordinated with passes of the Akebono satellite in July 1997 were used in a project aimed at understanding the driving mechanisms of ion outflow and the characteristics of the electrodynamics in the polar ionosphere.

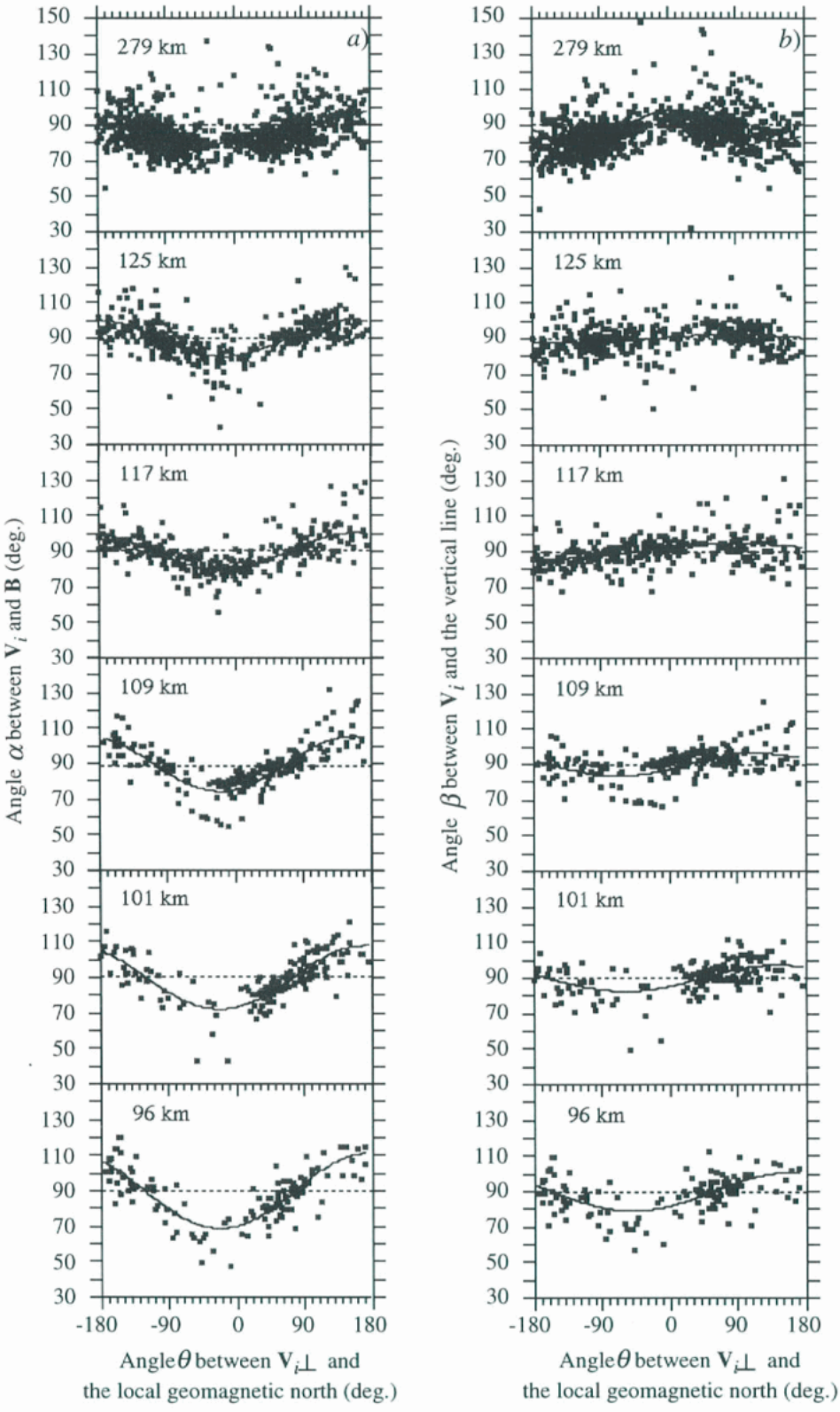

Figure 46: Scatter plots of the angles between the ion velocity V_i and the B vs. the geomagnetic azimuth of $V_{i,\perp}$ (left panels), and between Vi and the vertical direction vs. the geomagnetic azimuth of $V_{i,\perp}$ (right panels). Panels from bottom to top show increasing altitudes. If the ions move horizontally, the right panels should show no dependence on the azimuth angle. This is the case in the E-region at 96-125 km altitude. If they move perpendicular to B, the left panels should be close to the 90° line. For weak electric fields, which is the case that is shown here, even at 279 km in the F-region the ions move horizontally rather than perpendicularly.

These simultaneous observations enabled spatial and temporal variations of several electromagnetic parameters such as the electric field and particles to be distinguish (Susuki, 1998).

One of the most striking phenomena occurring in the topside ionosphere is the so-called ion outflow by which considerable mass is supplied to the magnetosphere from the Earth's atmosphere. The MLT distribution and Kp dependence of ion outflow and inflow events have been determined based on data analysis using CP-7 data from the EISCAT VHF radar. Both the ion outflow and inflow events can be observed at any local time (MLT), irrespective of day-side and night-side, and under any magnetic disturbance level, irrespective of quiet and disturbed levels. Both, outflow and inflow events are more frequently observed in the night-side than in the day-side. The outflow events are more frequently observed than the inflow events at all local times except midnight and at all Kp levels. The difference in the occurrence frequencies between the outflow and inflow events is less around midnight. The occurrence frequencies of both the ion outflow and inflow events appear to increase with increasing Kp level, while the occurrence frequency of the inflow appears to level off at some Kp level, see Figure 45 (Endo, Fujii, Ogawa, Buchert, Nozawa, Watanabe and Yoshida).

Large Scale Electrodynamics and Convection

The ions in the ionosphere are mainly affected by electric fields and neutral wind drag. In which direction the ions then move is a rather fundamental question. The ion motion relative to the local magnetic field line and the horizontal plane depends greatly on altitude and the magnetospheric electric field strength. One would expect that in the E-region the drag is more dominant because the high ion-neutral collision frequencies, while in the F-region the electric field makes the ions move perpendicular to the geomagnetic field **B**.

Using CP-1-H data, a large number of ion velocity vectors from both E and F-region were examined. When a strong electric field, $|\mathbf{E}|>25 mVm^{-1}$, is present, ions move perpendicular to the local magnetic field line both in the F-region and also in the upper part of the E-region (above 117 km). This suggests that ions move according to the E×B drift, just as expected, when the ion-neutral collision frequency is much lower than the ion gyro-frequency. At lower altitudes, the ions no longer move perpendicular to the magnetic field line, but rather horizontally as expected due to the stronger interaction between the ions and neutrals. However, under weak electric fields ($5 mVm^{-1}<|\mathbf{E}|<10 mVm^{-1}$), shown in Figure 46, the ions tend to move horizontally throughout the E-region and even in the F-region, which must be due to neutral winds. The main reason for the dependence of the ion motion on altitude and electric field strength is the varying relative importance of the magnetospheric electric field and the large-scale neutral wind drag (Fujii, Nozawa, Martuura and Brekke).

The large scale ionospheric convection is coupled to the magnetosphere by the region two field aligned currents, the auroral precipitation and the mapping of the electric field along the magnetic field lines between the ionosphere and the magnetosphere.

EISCAT has the capability to provide auroral observations of the convection ionospheric electric field and the density and the temperature of the ionospheric plasma from which the distribution of the ionospheric horizontal currents can be inferred. Three years of observations have been used to build a statistical model of the field aligned currents as a function of the Kp index from the divergence of the horizontal currents (Fontaine and Peymirat, 1996).

The Ionosphere-Magnetosphere-Model (IMM) self-consistently simulates the magnetospheric convection coupled with the ionosphere in the domain where the field lines are closed. One of the main inputs to the model is the distribution of the electric field along the polar cap equatorial boundary which can be partially inferred from the EISCAT radar. The region two field aligned currents predicted by the IMM are in agreement with the observations but show a poleward displacement probably due to the dipolar magnetic field model used (Fontaine and Peymirat, 1997).

The magnetospheric and ionospheric convection in the auroral zone depend on the polar cap convection. An empirical model of the polar cap convection electric field has been built using as boundary conditions the distributions of the field aligned currents and the electric field observed by EISCAT in the auroral zone. These electric field patterns will be useful in understanding the signature of fast events that are observed for strong magnetic activity by ESR (Peymirat and Fontaine, 1997).

The analysis of the 2D version of the time-dependent Petschek-type reconnection model has been extended to include the reconnection rate self-consistently, rather than as an input parameter. This model serves as a prototype for

the more realistic (3D) geometries needed to describe the magnetopause and magnetotail current sheet. This has proved successful to the extent that this parameter now only needs to be specified during an initial short (dissipation-dominated) interval. This 'kick' is necessary because, during the short initiation phase, Petschek's magnetohydrodynamic (MHD) wave mechanism has not yet come into effect; the MHD waves need a short period to propagate beyond the confines of the small diffusion region. Several case studies have been analysed with different 'kicks' and with the plasma conductivity held constant (an unrealistic assumption, but one imposed to simplify the computations). First results suggest that the most efficient energy release is through a series of pulses with asymmetric shapes. This tentatively confirms that reconnection is inherently time varying, with an initial rapid increase of the reconnection rate followed by a much slower decrease, as implied from observations of reconnection-associated phenomena in the solar and magnetospheric context.

To provide empirical data, which are essential to these investigations, the Sussex database of all-sky camera observations of the night-side auroral ionosphere has been searched. Several intervals have been identified containing rapid poleward-moving auroral arcs, and a technique which allows indirect measurements to be made of the reconnection rate from the observed arc velocity has been applied. The optical data were analysed in conjunction with simultaneous EISCAT observations, to determine the plasma properties of the ionosphere (in particular the bulk plasma velocity) through which the arcs were moving. Significant differences were observed between the arc motion and the background plasma velocity, conforming to expectations of the arcs mapping to a near-Earth (<30 RE) magnetotail reconnection line. With the reconnection rate variations inferred from the poleward-moving arcs as input, the newly extended reconnection model has been used to calculate the corresponding behaviour of the plasma conductivity. Although the intervals of poleward arc motions were often short (a few minutes or less), in several instances it was possible to discern an initial rapid decrease in the conductivity, followed by a slower increase.

Analysis has continued of the physics of Flux Transfer Events, which are one of the most exciting phenomena discovered by EISCAT to date. The analysis has been done by fitting ion data measured by satellites during FTE events with the two-Alfvén-wave version of a cusp model. In this case the model was applied to much shorter distances from the X-line appropriate to the day-side magnetopause. The fits were found to work extraordinarily well in all plasma parameters and also to predict the field line rotations and the FTE in the correct places. In effect, these fits have shown that FTE signatures are simply partial passages of the satellite into an open low-latitude boundary layer (LLBL). This could be explained as either a temporary compression of the reconnecting magnetopause so that the LLBL is moved over the satellite or because a bulge in the reconnection layer has passed over the satellite: such bulges are expected to result from transient reconnection pulses. There has been considerable controversy about which of these two mechanisms causes FTE signatures. This is important because the statistics of FTE occurrence are such that the reconnection pulse theory leads to the conclusion that FTEs are responsible for the majority of the observed transpolar voltage, hence pulsed reconnection must be the dominant form. By careful analysis of the reconnection rate, it has been possible to resolve this controversy and show that there is indeed a pulsed reconnection rate variation associated with each FTE. In addition the work has provided the answer to a major puzzle about magnetopause FTEs, namely why they sometimes exhibit a core of excess particle pressure. This high-pressure core is well explained by the model; it results from the fact that field lines at the core have been opened for much longer than those draped over the core, so that there has been time for higher densities of magnetosheath ions to reach the satellite. Thus events without a core are simply those seen closer to the reconnection site that produced them.

Recent years have seen a great increase of interest in the modelling of processes occurring at high-latitudes in the cusp and cleft regions. In part this is undoubtedly due to the advent of the ESR as a major tool for the observation of this part of the ionosphere, and an appreciable amount of work has been directed at simulating the kinds of phenomena, such as soft particle precipitation, which the radar should observe. A two-dimensional model of cusp precipitation has been used to investigate pulsed reconnection signatures and how they will appear to satellites following meridional and longitudinal orbits. The model is found to be capable of explaining previous observations which, although very different, arise from pulsed reconnection at the magnetopause under the same conditions, the differences arising from the direction of the satellite path. The reconnection events were revealed to be sporadic in time, but not patchy in space, events being necessarily more extensive than the three hours of local time that the satellite was in the cusp region during the longitudinal pass. This initially controversial result has been confirmed though

later work. The ability of the technique to measure an accurate reconnection rate was also confirmed. The model is currently the only one that can predict time-dependent changes in the cusp, and also reproduces observed ion steps seen simultaneously in both up-going and down-going ions by the POLAR satellite, leaving no doubt that the steps are caused by variations in reconnection rate and indicating that the open model of solar wind injection and transport in the cusp region, is correct and that the reconnection rate is indeed pulsed when these stepped or saw-tooth signatures are seen in the cusp dispersion ramp (Lockwood, 1996, Lockwood and Davis, 1996a, 1996b, Lockwood et al, 1997).

An alternative explanation of poleward-moving events seen in radar data proposed that such events are caused by changes in the Y-component of the magnetosheath field induced by

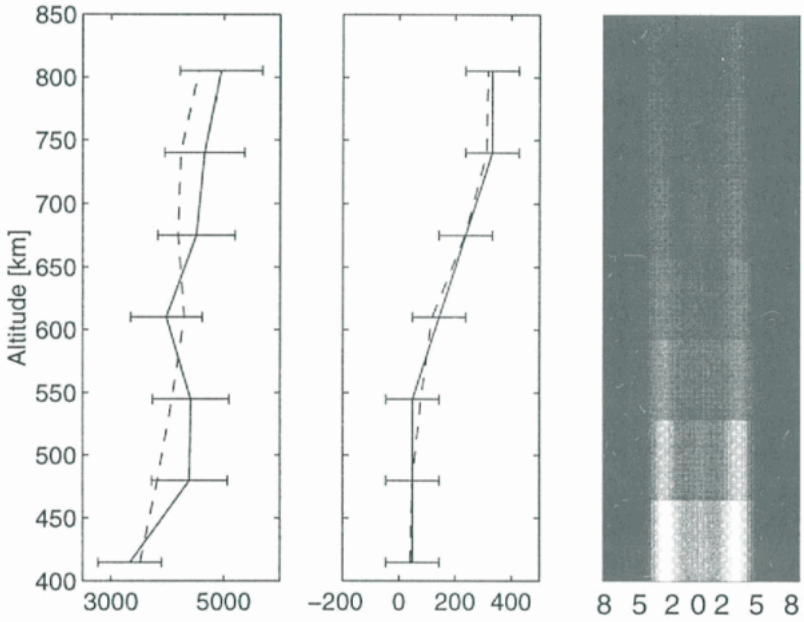

Figure 47: Calculated electron temperatures from the ion acoustic frequency (full line) and from the classical analysis (dashed line) (left panel). Calculated ion vertical drift from the ion acoustic frequency (full line) and from the classical analysis (dashed line) (middle panel). Grey scale coded spectra normalised to the maximum value.

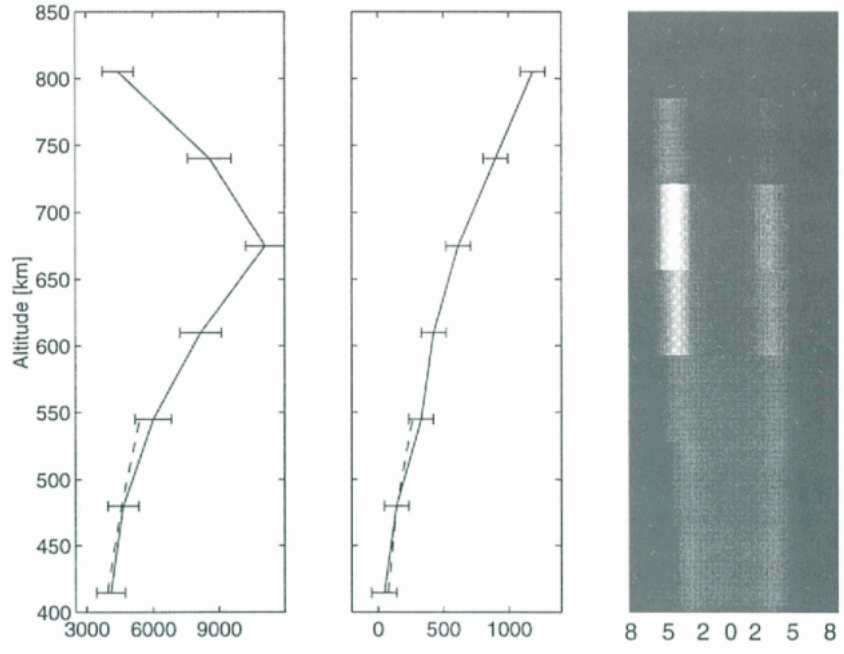

Figure 48: Same as Figure 47, but for a region of enhanced ion acoustic fluctuations

compressions due to solar wind dynamic pressure. The model has been used to demonstrate that this idea was not consistent with the sequences of images seen by an all-sky camera and the events seen by the EISCAT radars. However, the events were consistent with the effects of reconnection pulses.

The cusp model is based partly on the concept of how ions will react with the magnetopause Alfvén wave. Data from the day-side magnetopause and from hybrid simulations have shown that the predictions of the model are remarkably accurate. The simulations show that two such waves should be produced by a magnetopause reconnection site. Previous theory has thus been generalised to allow for the effects of Alfvén waves launched by the reconnection site and standing on the inner edge of the Low-Latitude Boundary layer, on the inflow from the magnetospheric side of the boundary. With this extension, the model reproduces observations remarkably well. This confirms that transient auroral events seen in the Low-Latitude Boundary layer are on open field lines and are due to pulsed reconnection. Later work has included effects of ion reflection from the two Alfvén waves and showed that day-side precipitations are well explained as being on open field lines, rather than on closed field as previously supposed. This can explain a number of paradoxes which were never resolved by the old view of the magnetic topology. For example, it has been shown that the projection of the reconnection X-line can be longer than the cusp, so the application of a typical reconnection voltage does not cause excessive flow speeds through a narrow "throat" (Lockwood and Moen, 1996, Moen et al, 1996, Lockwood et al, 1997).

Non-Thermal Plasmas Echoes

The COherent SCATter (COSCAT) experiment has been employed to make continued observation of E-region plasma irregularities with EISCAT at magnetic aspect angles close to orthogonal. The temporal resolution of COSCAT observations was previously limited to 1 s by the minimum dump time of the EISCAT correlator. Following the work of Schlegel et al. (1990) a new high temporal resolution experiment was developed for COSCAT and successfully run between the 7th and 14th March, 1997. Individual power profiles were recorded in consecutive locations in the correlator memory, which was dumped every 5 seconds. This procedure enabled coherent backscatter power to be measured at 12.5 ms resolution and a measurement of the full autocorrelation function to be made every 100 ms. The observations indicate that E-region UHF radar backscatter is dominated by individual scatterers that have lifetimes between 20 and 60 ms (Eglitis et al. 1997b).

Incoherent scatter spectra occasionally indicate the presence for brief periods of ionospheric small-scale structures and turbulence at scales smaller than the typical space and time resolution of the radar. Such events violate the assumption of space and time uniformity used in the analysis of the received signal. This results in an erroneous estimate of the derived ionospheric parameters, or even in the failure of the analysis when the measured spectrum departs too much from its usual shape. Two types of such phenomena have been extensively studied, namely the small-scale auroral structures of intense flow bursts, and the ion-acoustic turbulence. The large differences in their spectral signature and origin illustrate both the variety of the small-scale phenomena occurring in the ionosphere, and the capability of the incoherent scattering technique to detect them and to infer original information on the mechanisms responsible for them.

EISCAT has observed sporadic events (less than 20 s) occurring near a substorm onset, characterised by a strong ion temperature increase in the auroral F-region and associated with significant anisotropy and distorted incoherent scatter spectra. The simultaneously observed electric field is too weak to account for the temperature increase by frictional heating. Indeed, it is interpreted as a spurious effect of the standard analysis procedure in the presence of short-lived ion drift velocity fluctuations, perpendicular to the background magnetic field, which are unresolved by the radar because of space or time-scales smaller than the measurement resolution. By simulating this effect, a modified analysis of incoherent scatter spectra has been developed to infer the real temperatures and the amplitude of velocity fluctuations. The resulting ion and electron temperatures are found to be respectively overestimated and underestimated relative to the initial predictions of the standard analysis. The maximum velocity variation amplitude reaches up to about 2000 ms^{-1}. Co-ordinated satellite and ground-based data tend to argue in favour of a time varying electric field (possibly a standing Alfvén wave) as the origin of the observed EISCAT spectral distortions (Forme, Fontaine, Persson, 1998)

The case of enhanced ion acoustic echoes also prevents the use of the standard analysis procedure. The received power is extremely enhanced by up to one or two orders of magnitude above usual values, and it is mostly contained in one of the two ion acoustic lines. Using the very

clear spectral signature of these echoes, it is now possible to extract estimates of the electron temperature and the ion drift within the region of enhanced ion acoustic echoes, Figure 47. The electron gas is strongly heated up to 11,000 K with temperature gradients of about 0.02 Km^{-1} Figure 48. Such strong electron temperature gradients cause enhancements of the ambipolar electric field and account for large ion outflows with fluxes of about 1014 $m^{-2}s^{-1}$ at 800 km altitude (Forme and Fontaine, 1998).

A further chain of satellite receiving stations has been established in the north of Scandinavia enabling images of spatial structures in electron density to be obtained routinely in the auroral, cusp and polar-cap ionospheres using radio tomographic measurements. The automatic receivers were deployed at Longyearbyen, Bjørnøya and Tromsø in the summer of 1996 adding to the system that has been operating at Ny-Ålesund since 1991. The system yields regular tomographic images of the electron

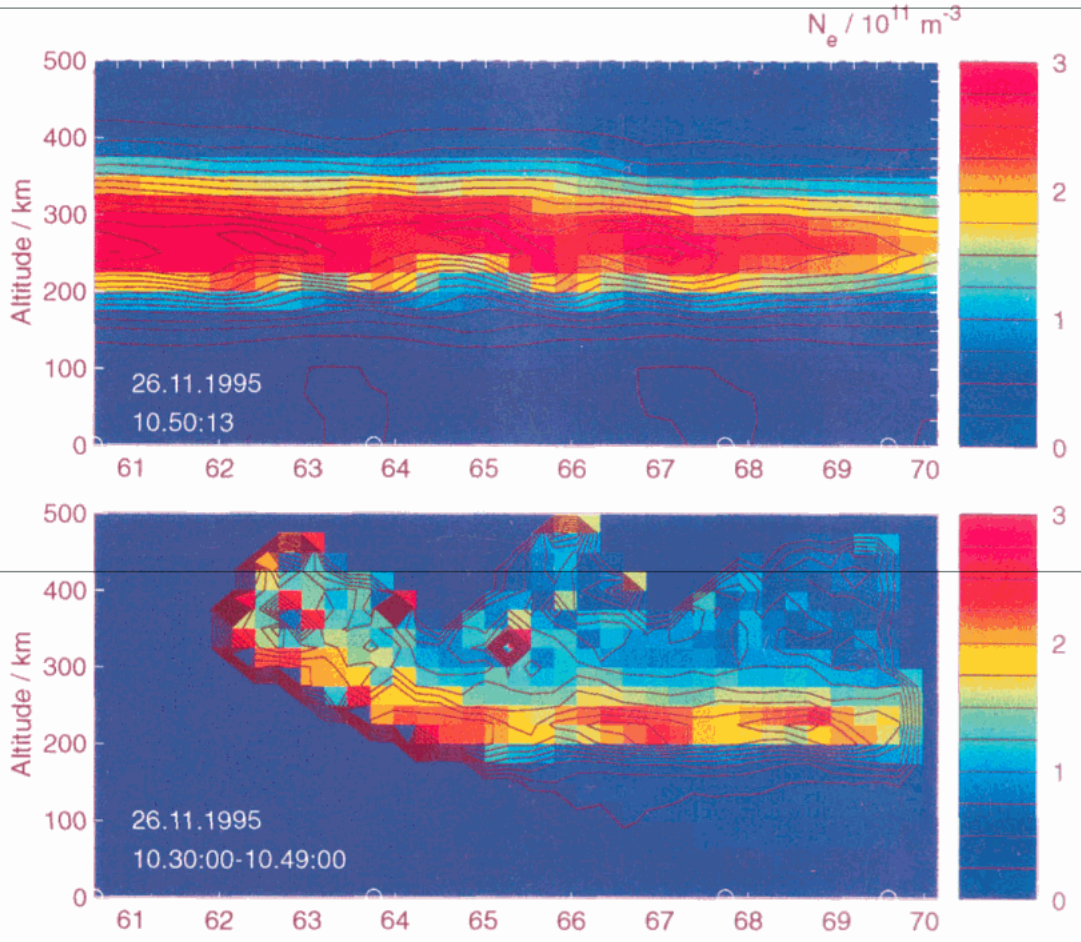

Figure 49: Travelling ionospheric disturbances in the F-region, as observed by a tomographic chain extending from Tromsø to the south of Finland (top panel) and the EISCAT VHF radar (bottom panel). Since the two observations are not simultaneous, the wave propagation causes a displacement of the wave fronts in the two panels.

Ionospheric Tomography

Electron densities measured by EISCAT have been used in verifying the capability of the satellite tomography method in mapping the ionospheric F-region. Although differences, especially in the layer thickness, may occasionally appear, the tomographic method is capable of portraying the F-region structures, e.g. travelling ionospheric disturbances, in a quite reliable way, Figure 49 (Nygrén et al., 1996; Nygrén et al., 1997.)

density in a region of key importance to the understanding of the interaction of the solar wind and the magnetosphere/ionosphere system, which also covers the viewing areas of the EISCAT and ESR radars.

The most striking advance has involved relating optical observations from all-sky camera and meridian scanning photometer instrumentation on Svalbard to electron density features seen in tomographic images. One case study in the daytime cusp sector shows, for the first time from

ground-based instrumentation, the simultaneous ionospheric signatures of three characteristic features of a magnetopause reconnection event. A region of auroral-E ionisation can be identified with energetic electron precipitation from the central plasma sheet. This terminates at its northern edge at a boundary identified with that of closed/open field lines. To the north a steep gradient is found that leads to a field-aligned enhancement with a narrow structure extending into the high topside F-layer, probably linked to a field-aligned current.

An upwards tilt in the height of the F-layer peak over a limited range of latitude to the north can be linked to the dispersion of the soft ions, precipitating on the poleward-convecting open flux-tubes. Signatures in the optical emissions, with a sharp equatorward edge to the red-line aurora and poleward moving forms, represent known characteristic features of magnetic reconnection and support the interpretation of the features imaged by tomography (Walker, Heaton, Kersley, Mitchell, Pryse and Williams).

Another project addresses the relationship between electron density enhancements at both E- and F-layer heights and the structure of discrete auroral arcs in green- and red-line emissions respectively in the region 1 field-aligned current sector, after magnetic noon. Results from case studies have enabled the ionospheric signatures of the auroral precipitation to be identified. It has also been possible to calculate the different response times for the ionisation in the two height regions (Moen et al.).

First results have been obtained linking a spatial image from ionospheric tomography to the temporal changes in electron density seen in an early run of the ESR radar. A spatially-narrow field-aligned enhancement in electron density,

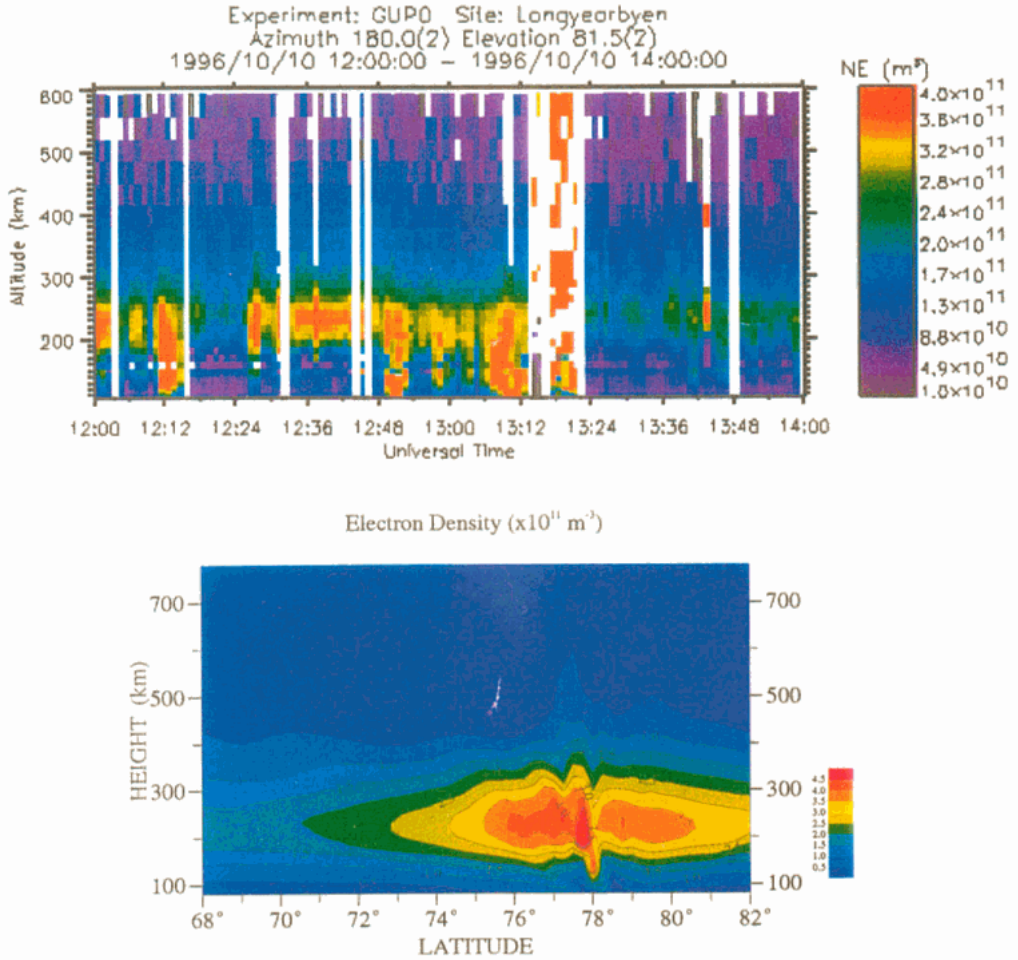

Figure 50: Upper panel: Electron densities obtained from the EISCAT Svalbard Radar on 10 October 1996. The enhancement in electron density occurring between 1307 and 1312 is of particular interest. Lower panel: Tomographic image of electron density for the satellite crossing at 70°N, 3°E at 13:21 UT on 10 October 1996. A latitudinally narrow enhancement in electron density at 78°N in the ionosphere to the West of Svalbard is a prominent feature

extending over a confined range in latitude, has been identified with a temporally-confined increase in plasma concentration measured by the radar, Figure 50. The interpretation of the observations has been aided by information on convection flows obtained from the CUTLASS HF radar system (Mitchell, Kersley, Heaton and Pryse).

Images from the high-latitude chain have been used with EISCAT observations in a study of the day-side trough, a little understood feature of the high-latitude ionosphere. Indeed, the only substantial previous work used ionosonde observations from IGY in 1957/8. The morphology of the quiet daytime trough has been established at the edge of the dusk convection cell in the post-noon sector. In a case study during disturbed geomagnetic conditions, the existence of the tongue of plasma feeding day-side photoionisation into the polar cap, predicted by modellers, has been demonstrated experimentally. Results from earlier studies have confirmed the existence of a polar hole of depleted plasma, convecting in darkness in the centre of the winter dawn cell (Pryse et al., 1997; Pryse, Kersley, Williams and Walker

Ionospheric Modelling

A numerical model which describes the vertical structure of the ionosphere between 100 and 3000 km in the auroral region has been developed. It proved its ability to reproduce in a quantitative manner the auroral ionosphere either for the smooth diurnal variations or the response to electrodynamic perturbations (Blelly et al., 1996, Diloy et al., 1996, Robineau et al., 1996).

This calibrated model has been shown to be an important tool to help understanding the behaviour of the ionosphere in situations characteristic of the high latitudes and even appears to be a predictive model which may be useful for the data processing.

The model has been used to compute numerically the ionospheric conductivities above EISCAT with respect to the solar lighting and the precipitation. The analytical model which was derived from the simulations compared well to the empirical model of solar conductivities derived from three years of EISCAT data; in particular, it allowed to show that the data used for the computation of these conductivities were polluted by data corresponding to precipitation periods (Lilensten et al., 1996).

Following this study, a predictive model of the solar conductivities above ESR has been proposed. In parallel, the analysis of the ESR data has been started and initial results show the ability of the model to reproduce accurately the ionosphere above ESR during quiet periods, Figure 51.

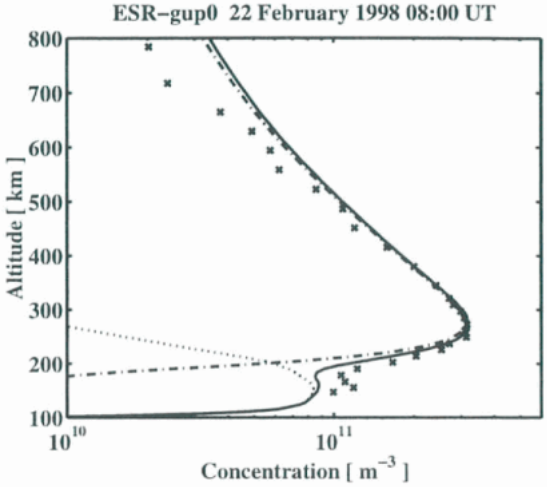

Figure 51: ESR electron concentration profile (crosses) vs. model (full line) for 22 February 1998; the O^+ (dot-dashed) and molecular ions concentrations (dotted) have been added.

A self-consistent method for the analysis of daytime electron density profiles in the F-region was developed. It is based on a theoretical F-region model with 23 chemical reactions and uses measured profiles of electron density, electron temperature, ion temperature and plasma drift. The measured electron density profile is retrieved with high accuracy. Besides, the model yields concentrations of the main neutral constituents, O, O_2, N_2, the vertical plasma drift, the exospheric temperature and the shape parameter of the neutral temperature profile. Through an iterative procedure the O+ - NO^+/O_2^+ composition in the transition height between E and F layer can also be found which improves the reliability of the incoherent scatter derived quantities. The latter can be inferred from Figure 52 comparing the results of a quiet and a disturbed day. For the disturbed day the composition ratio calculated with the model differs markedly from the profile used in the standard EISCAT data evaluation. Neutral atmospheric parameters have been derived form the model for a series of days, quiet and disturbed. The results show that the method yields reliable values of these parameters and can be used for the analysis of long-term as well as for day-to-day variations of the thermospheric parameters. (Mikhailov and Schlegel).

Several studies have been carried out relating EISCAT measurements to the results of the CTIM ionosphere-thermosphere model. This has involved investigations of specific periods as well as more general studies of long-term trends,

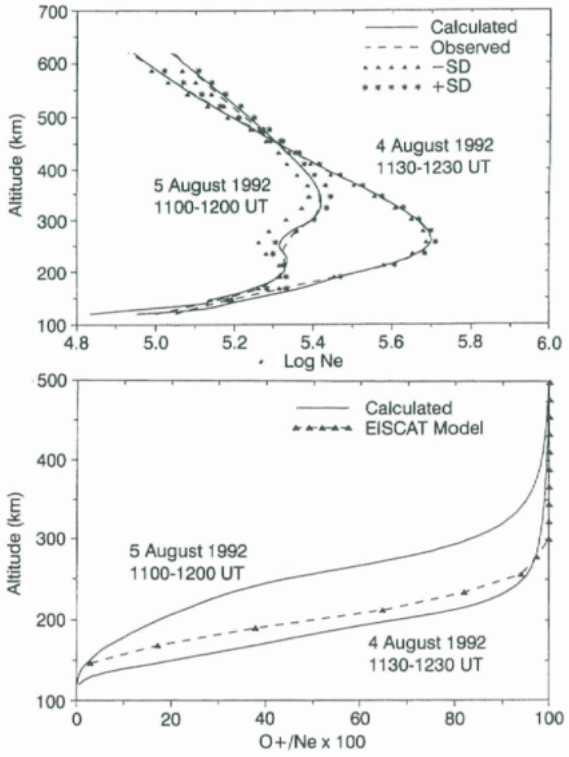

Figure 52: The upper panel shows the measured and calculated electron density profiles for a quiet (4 Aug. 1992) and a disturbed day (5 Aug. 1992), together with a band of standard deviations. The lower panel shows the ion composition used in the standard EISCAT data evaluation and the corresponding profiles corrected with the model described in the text.

seasonal and solar cycle variations. In the case studies, it has been shown that the input electric fields and particle precipitation patterns at high latitudes need only be moved small distances to have significant effects on the modelled behaviour. Virtually any EISCAT measurements can be simulated with the right combination of high-latitude inputs, though there is no guarantee that this will be a unique solution. The case studies have prompted a development of CTIM whereby a much more flexible scheme has been introduced for selecting and modifying the high-latitude inputs to find a match with the ionospheric response (Schoendorf et al., 1996, Aruliah et al, 1996a, 1996b, 1997).

Continued work on the UCL FPI database which pointed to the equinoctial asymmetry found in thermospheric and ionospheric data has revealed further unexpected behaviour in long-term trends. In particular, it has been found that there is a solar cycle dependence of the electric field - that is, at the same Kp there is a different electric field behaviour at solar maximum and solar minimum. This was hinted at in the way the thermospheric winds behaved with solar cycle, but the average ion velocities were then shown to have a similar trend, and a plausible explanation for this has since been modelled with the CTIM model (Aruliah et al, 1996a,b, 1997).

Besides long-term trend studies, case studies have been completed involving auroral phenomena and their connection to the solar-terrestrial interaction exemplified by travelling convection vortices and substorm morphology (Luhr et al, 1997; Gazey et al, 1996).

EISCAT data have been used to validate the new tidal generation code in CTIM. An improvement on previous versions of CTIM has been introduced by making the lower boundary the input layer, and making the velocities, temperatures and pressures there self-consistent. This has given the model the ability to simulate tidal oscillations self-consistently at much lower levels than before - in fact at heights where EISCAT often sees strong tidal signatures Some preliminary evaluations of the success of modelling the radar data have been made and this work is continuing with more directed and specific studies. Included in this will be evaluation of the modelled strength of the propagation of planetary waves into the upper thermosphere (Muller-Wodarg, 1997).

The ionospheric signature of a Flux Transfer Event seen in the EISCAT radar data on 29 March 1992 has been used as the basis for a modelling study using a new numerical model of the high-latitude ionosphere to investigate the evolution of structure in the high-latitude ionosphere. A localised velocity enhancement, of the type associated with FTEs, is added to the plasma as it passes through the cusp. This is found to produce a region of greatly enhanced ion temperature. The new model can provide greater detail during this event as it includes anisotropic temperature calculations for the O^+ ions. This illustrates the uneven partitioning of the energy during an event of this type. O^+ ion temperatures are found to become increasingly anisotropic, with the perpendicular temperatures being substantially larger than the parallel component during the velocity enhancement. The enhanced temperatures led to an increase in the recombination rate, which results in an alteration of the ion concentrations. Large upward fluxes are seen to transport plasma to higher altitudes, contributing to the alteration of the ion densities. A region of decreased O^+ and increased molecular ion concentration develops in the cusp. The electron temperature is less enhanced than that of the ions. Plasma is stored in the topside ionosphere and released several hours after the FTE has finished as the flux tube convects across the polar cap. This mechanism illustrates how

concentration patches can be created on the day-side and modified as they proceed into the night-side polar cap (Balmforth, Moffett and Rodger).

of the O-mode heater wave to the Z-mode near the Spitze angle which is about 6.0° at Tromsø. Many hours of excellent data on several days

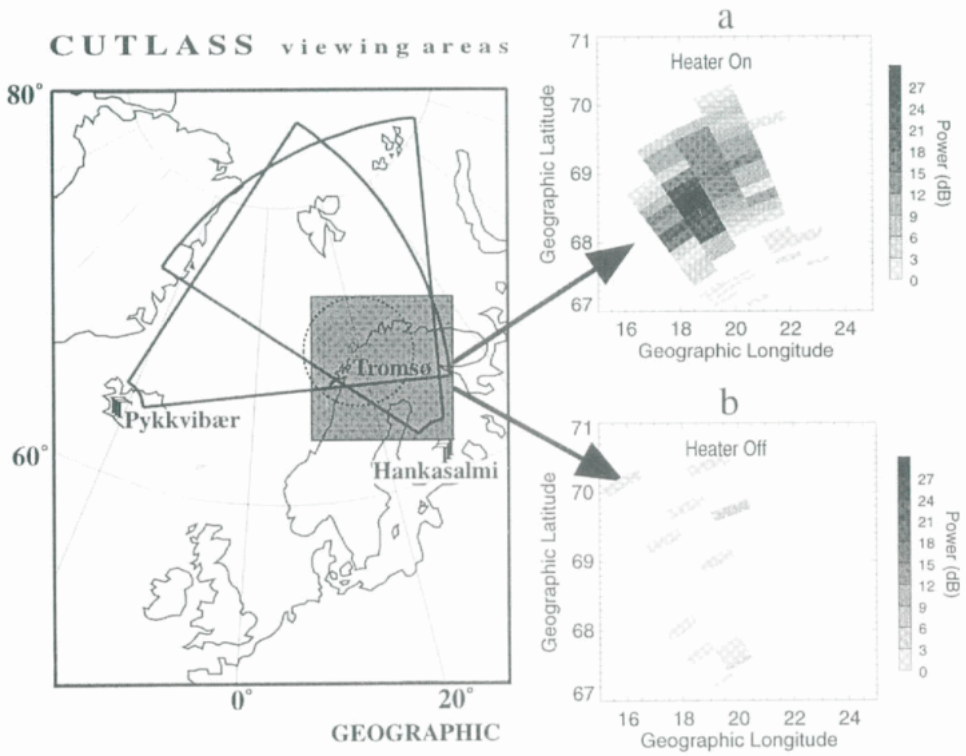

Figure 53: The map on the left depicts the locations and fields-of-view of the CUTLASS and EISCAT radars. The shaded region indicates the area covered by the spatial plots presented in (a) and (b). (a) Returned power from the CUTLASS Finland radar on 26 April 1996, during a heater-on period. (b) As for (a), but showing returned power during a heater-off period

Ionospheric Modification

Analysis and interpretation of EISCAT Langmuir turbulence data taken during previous Heating campaigns progressed with several publications. With the increasing part of the solar cycle conditions are improving for further experiments which have become rather advanced in the variety of measurement techniques used. In an effort to understand previous results of out-shifted plasma lines and to test a recently advanced theory proposed to explain them, an extensive heating campaign was held in November 1997. Both EISCAT UHF (tristatic) and VHF incoherent scatter radars were used with chirped modulation and other pulsed techniques to observe both natural and enhanced plasma lines with high spatial and frequency resolution.

An HF radar (Dynasonde) made supporting measurements and stimulated electromagnetic emissions (SEE) were measured to determine the proximity of the HF heater wave from a gyro-harmonic. The UHF antenna was moved systematically between vertical and field aligned in order to look for effects related to conversion

were obtained. Enhanced topside UHF plasma lines were observed for antenna directions which are close to the magnetic field (Kohl, Rietveld, la Hoz, Hagfors, Mishin, Isham and Leyser).

Extensive use has been made of the CUTLASS HF radars to study small scale field-aligned plasma density irregularities which are efficiently excited by the EISCAT high power HF facility during O-mode heating of the F-region. CUTLASS has proven an ideal tool for this purpose, since it is sensitive to irregularities with scale sizes of a few tens of cm across the geomagnetic field. Also, the Tromsø site is within the field of view of both the Finnish and Icelandic radars which comprise the CUTLASS pair. A number of important new results have been obtained from experimental campaigns carried out during 1996/7.

Figure 53 illustrates an example of the first detailed study of the two-dimensional distribution of heater induced irregularities. These were mapped by the CUTLASS Finland radar, using a five beam scan with a 1 s dwell time in each pointing direction. Range resolution is 15 km and

the beam widths correspond to distances of around 50 km at these ranges (1000 km). The heated region extends over three degrees of latitude and six degrees of longitude. This result is also important in establishing the threshold electric fields required to excite irregularities at the edges of the heater beam. Thresholds are often less than 0.01 Vm^{-1} (Bond et al., 1997).

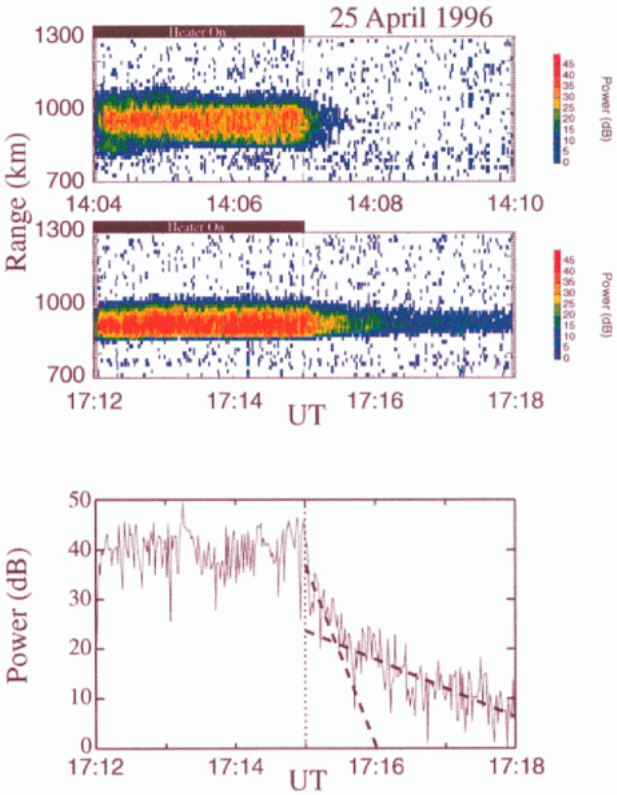

Figure 54: Examples of heater-induced plasma irregularities as observed by the CUTLASS Finland radar.

Figure 54 illustrates two examples of the temporal decay of heater induced irregularities seen in CUTLASS beam 5 backscatter from 25 April 1996. In the upper panel, backscatter falls below the noise level in less than one minute, whereas in the second panel the decay is not complete in three minutes. Preliminary results indicate that shorter decay times tend to occur close to midday (LT) and lengthen towards dusk. The data in the lower panel indicate that a two stage decay process is clearly evident as the decay times lengthen; the dotted lines are two exponential functions fitted to the data after heater off (Bond, Robinson, Eglitis, Wright, Stoker and Lester).

The scatter in Figure 55 is from a comparison of CUTLASS and EISCAT tristatic measurements of the drift speed of heater induced irregularities. There is good correlation between the two forms of measurement indicating that, for these conditions at least, the artificially induced irregularities appear to drift with the background flow (Eglitis, Robinson, Rietveld, Wright and Bond).

Electron density irregularities on the scale of 10's of meters to kilometres can be excited using the EISCAT Heating facility. They can be studied using several different techniques such as the anomalous absorption of diagnostic HF

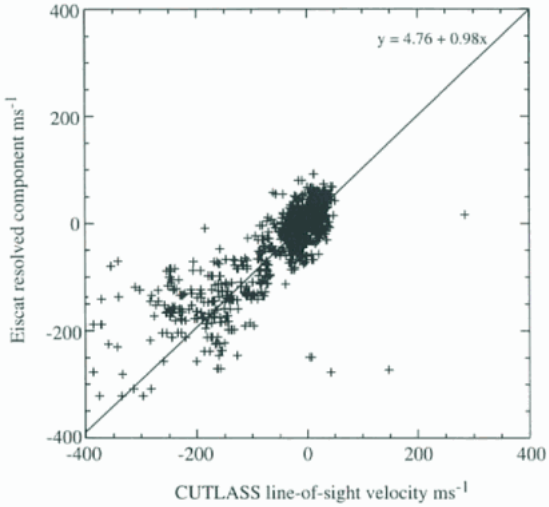

Figure 55: Graph of the resolved component of the plasma drift velocity determined from EISCAT against the irregularity phase speed of artificial field-aligned irregularities detected by the CUTLASS Finland radar

waves and coherent HF radars. In the last two years a variety of new instruments and techniques have been applied to study their formation processes and to use them as a diagnostic of ionospheric motions. CUTLASS allows continuous remote sensing of the irregularities from Finland and Iceland. The dependence of the back-scattered power on the difference of the heater-frequency from a gyro-harmonic has been clearly demonstrated. The heater-produced irregularities allow a short integration time which, combined with a 15 km range resolution, resulted in radar measurements of a naturally occurring ULF wave at far better temporal and spatial resolution than has been achieved previously. For example, a narrow small scale resonance width of 60 km was measured for a field line resonance. In a complementary technique, a receiver near St. Petersburg with an antenna pointing towards Tromsø, was able to receive signals from BBC HF broadcast transmitters which are scattered off similar artificial irregularities of tens of meter scale sizes. Again, variable Doppler shifts due to pulsations were measured. In addition it was shown that on occasion the scatter must have been

from E-region heights, and on another occasion intriguing signals which are probably the second harmonic of a Stimulated Electromagnetic Emission feature were observed.

A third way of examining artificial kilometre scale irregularities was tried for the first time in a campaign in November 1997 using spaced receivers on the ground to record the signals from polar orbiting Russian navigation satellites as they passed through the heated region. A tomography analysis of the data is in progress (Rietveld, Robinson, Yeoman, Bond, Wright, Tereschenko and Blagoveschenskaya).

The generation of ELF waves using modulated ionospheric heating, whereby one modulates the conductivity of the auroral electrojet, has been studied extensively in previous years. Recent advances have been made through new receivers,

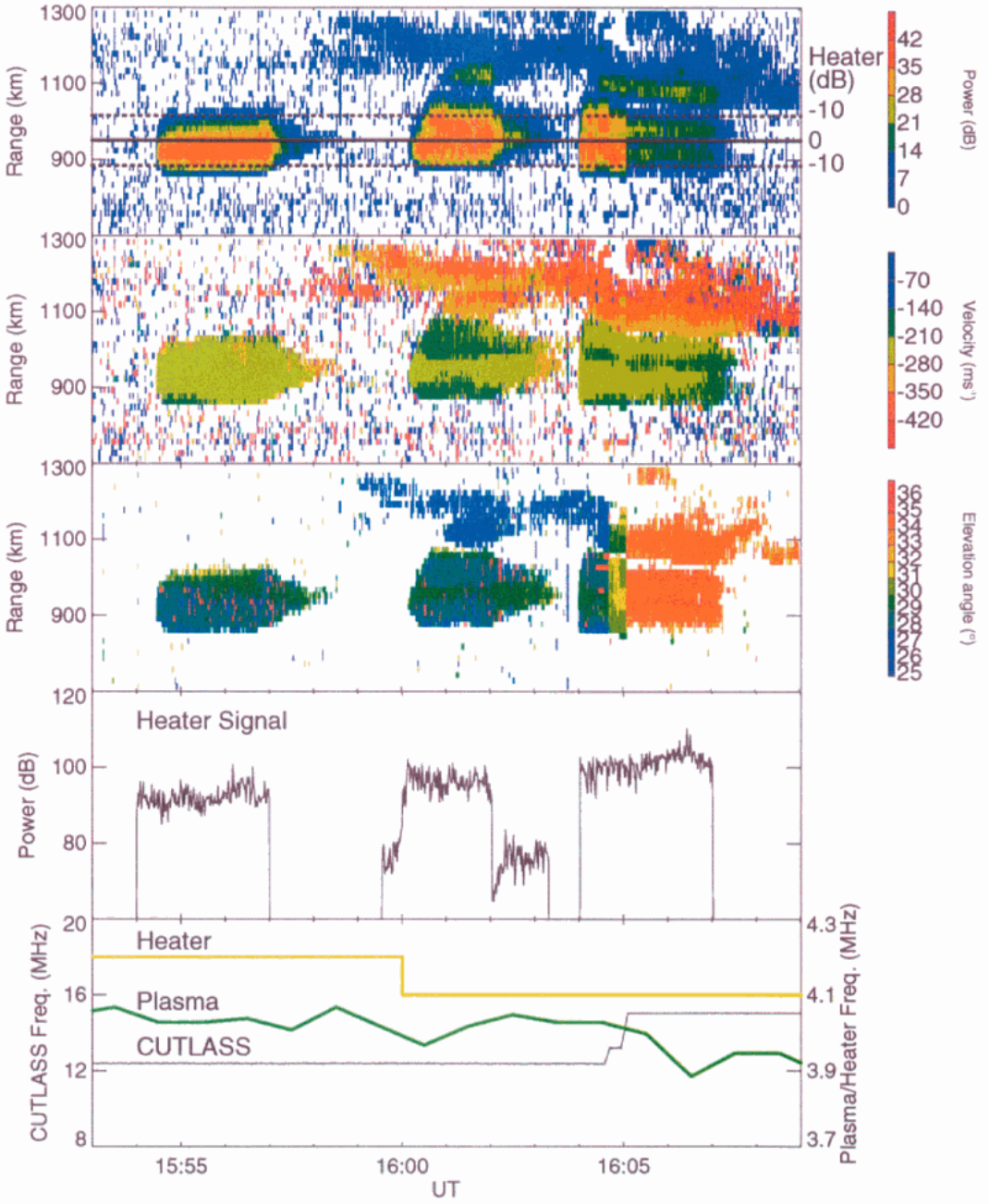

Figure 56: Observations of artificial and natural plasma irregularities observed by CUTLASS Finland on 24 April 1996. Depicted are the CUTLASS measured backscatter power (top panel), irregularity phase speed (second panel) and elevation angle (third panel). The modulation of the heater (fourth panel) is monitored by an independent receiver and the bottom panel depicts the heater, plasma and CUTLASS frequency for the period of observation.

extremely accurate GPS timing and modern data storage technology. They allow a much more detailed analysis of the data after the measurements such as simultaneous measurements of the ELF modulation harmonics and their source heights. From such measurements information on the D-region can be obtained over a wider height range since the different harmonics have their source at different heights. Measurements were also made to investigate the possibility of O-mode heating producing enhanced ELF wave generation through the modulation of an E-region instability. Although there were indications of such an instability-enhanced mechanism, subsequent measurements showed that an instrumental effect could also explain the results (Rietveld, Stubbe and Barr).

modulation while AM was sinusoidal. Another possibility is that BS transmission can be phase modulated and thus the radiated VLF signal has several components in its spectrum and received VLF signal may be harmonically distorted. API experiments have a modulation pattern which contains harmonics at 100 Hz intervals. These harmonics were received in the VLF frequency range between about 1 kHz and 6 kHz (Oikarinen et al. 1997).

The detailed data in Figure 56 illustrate the first observations of the interaction of heater waves with natural F-region radio aurora. Man-made radio aurora can be clearly observed in the intensity data in the upper panel, during the 'heater on' times (indicated by the data in the forth panel) in ranges between 850 and 1050 km

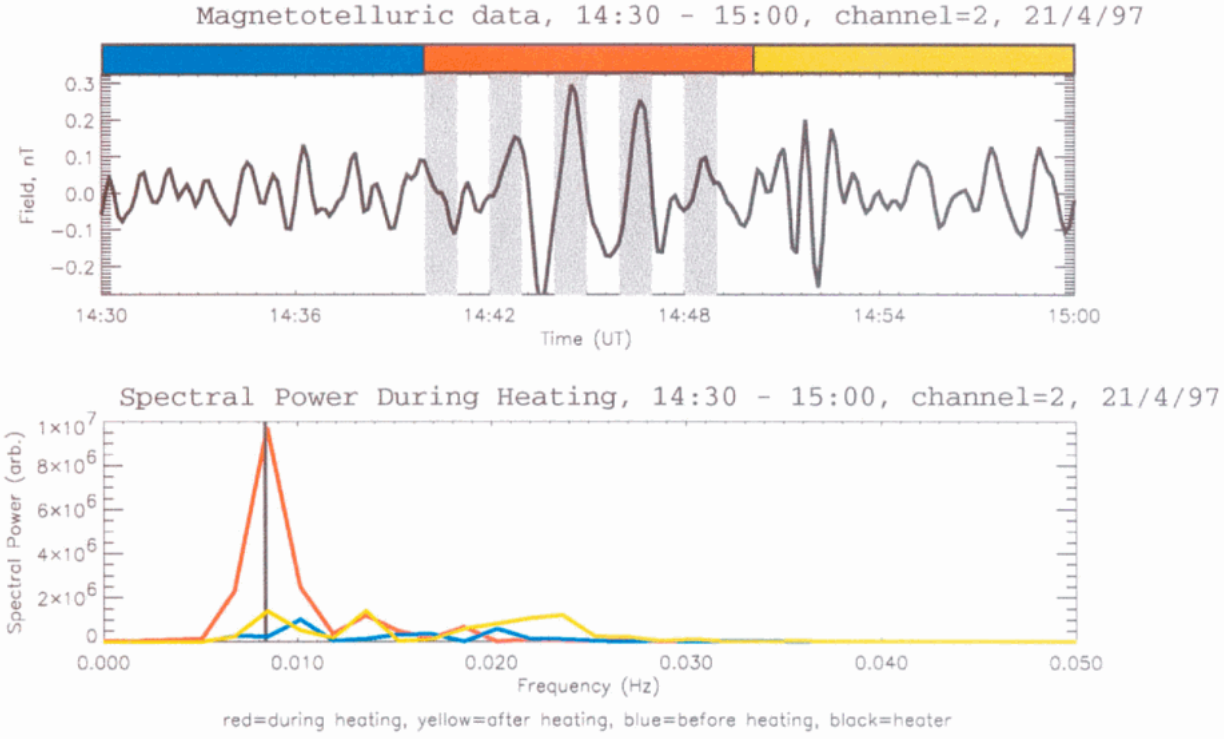

Figure 57: Magnetotelluric data taken from experiments run on 21 April, 1997. The top panel illustrates magnetotelluric measurements made at Wick before, during and after a period of artificial modification. The lower panel is a plot of the spectral panel during heating

VLF waves generated by the EISCAT heater wave in the ionosphere have been investigated. Both amplitude modulation (AM) and beam swinging (BS) of the heater have been used. The power spectral densities of the VLF signal at 2375 Hz and its harmonic 4750 Hz were inspected. There is no big difference between the methods at the basic frequency but at the harmonic the difference is surprisingly clear. One reason for this is that BS corresponds to on-off

from the Finland radar. Weak, natural aurora begin to appear in the farthest radar ranges just before 16:00 UT, and then drift steadily towards the heater beam. A remarkable event takes place just after 16:01 UT when a natural aurora comes close to the outer edge of the heater beam and is suddenly artificially enhanced by the high power radio waves. A similar thing happens just after the heater is turned on at 16:04 UT. The differences in the speeds of the natural and

artificial aurora are clearly illustrated in the velocity data in the second panel, and altitude differences can be inferred from the angle of arrival data in the third panel. The fifth panel indicates changes in the operating frequencies of CUTLASS and the heater, and also the peak plasma frequency, during the heating sequence.

During a heating campaign in April, 1997, artificially excited ULF waves from a heater modulated electrojet above Tromsø were detected a ULF wave characteristic of the development of a field line resonance (FLR) driven by a cavity mode caused by a magnetospheric impulse. When the heater is on, striating the ionosphere with field-aligned ionospheric electron density irregularities, a large enough radar target is generated to allow post-integration of the CUTLASS data over only one second. When combined with 15 km range gates, this gives radar measurements of a naturally occurring ULF wave at a far better temporal and spatial resolution than

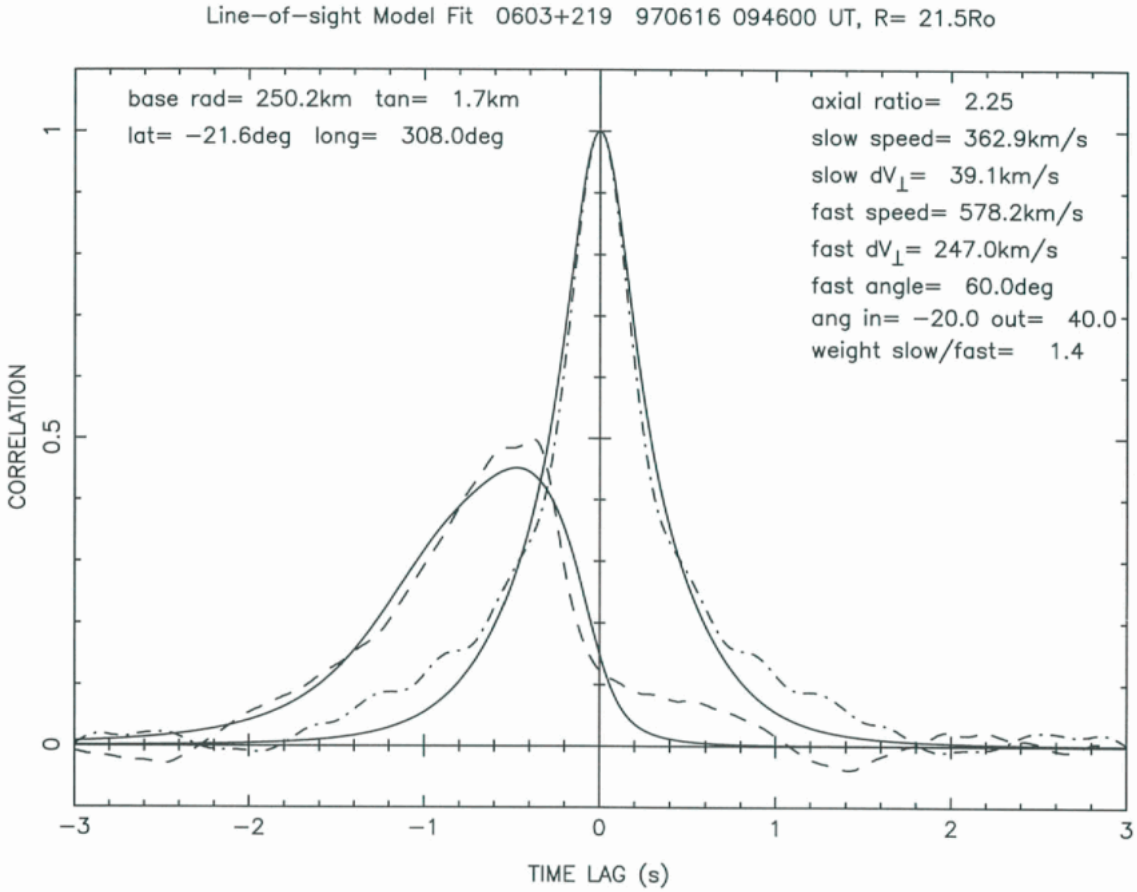

Figure 58: The auto and cross correlation functions of the power spectra from an observation of source 0603p219 on 16 June 1997. The dotted line is the data and the solid line represents the fitted curve.

by sensitive magnetotelluric field meters which were deployed at Wick in Scotland (Figure 57, lower panel). This is the largest range (around 2000 km) over which heater induced ULF waves have so far been detected.

The magnetic field times series (upper panel) and spectrum (centre panel) for waves of two minutes period, indicate field strengths higher than expected from simple dipole calculations, and could indicate some type of resonant response at Wick, where, as it happens, the field line resonance frequency is around two minutes.
The CUTLASS Finland radar has been operated in conjunction with the heater facility to examine has been achieved previously. The time-dependent signature of the ULF wave has been examined. The wave evolved from a large scale cavity resonance, through a transient where the wave period was latitude-dependent and the oscillation had the characteristics of freely-ringing field lines, and finally to a very narrow, small scale local field line resonance. The resonance width of the FLR was only 60 km and this has been compared with previous observations and theory. The FLR wave signature is strongly attenuated in the ground magnetometer data. This leads to the characterisation of the impulse driven FLR being only very crudely achieved with ground-based

diagnostics. An accurate determination of the properties of the cavity and field line resonant systems challenges the currently available limitations of ionospheric radar techniques. The combination of the latest ionospheric radars and facilities such as the Tromsø heater can result in a powerful new tool for geophysical research (Yeoman et al., 1997).

When fast and slow streams in the solar wind occur at the same latitude, owing to solar rotation there are occasions when a region of fast flowing plasma emerges from the Sun behind a region of slow flow. As the fast stream overtakes the slow stream, a compression region forms at the leading edge of the fast stream, which eventually generates shocks at a point beyond the Earth's

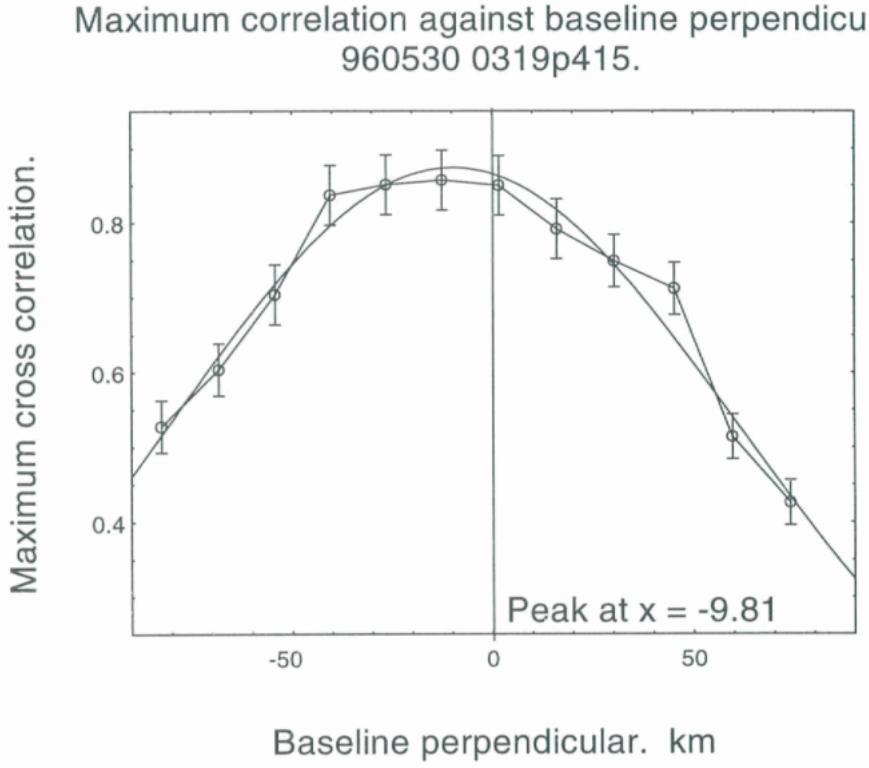

Figure 59: A plot to show how the correlation of the signal between the two sites varies as the baseline perpendicular to the direction of radial flow changes during the observation. A curve has been fitted which has a peak that is offset from zero by around 10km, indicating an off-radial component in the flow of the solar wind

Passive Observations, IPS

Measurements of interplanetary scintillation (IPS) made using EISCAT have continued to yield important results. Earlier work had confirmed that the solar wind has two distinct speeds at around 400 and 800 kms^{-1}. The fast streams are associated with the high latitude polar coronal holes and the low speeds with the equatorial streamer belt.

Recent work has studied the interaction of fast- and slow-streams when they occur at the same heliocentric latitude. In addition the technique has been extended to include measurements of the exact direction of the mid- and high-latitude solar wind, which in turn implies the direction of the interplanetary magnetic field.

orbit. These well known phenomena are called co-rotating interaction regions (CIRs); fully-developed CIRs have been studied by spacecraft. EISCAT IPS studies, however, have displayed a unique capability to study the early stages of a CIR, closer to the Sun.

Figure 58 shows an example where the cross-correlation function of the observations made at two sites are compared with a theoretical model to give values of the fast- and slow-stream velocities along the line of sight. The model fits two velocities owing to the bi-modal nature of the solar wind. In this case the 'fast' speed is found to be 578 kms^{-1} - slower than the usual value of 700-800 kms^{-1}, and the ratio of the "scintillation weight" per unit volume of the slow and fast streams is only 1.4 - far lower than the typical

value of ~10 which occurs because the slow stream is normally much denser. These results indicate that the fast stream has been slowed down to an intermediate velocity and the density and turbulence of the fast stream have been greatly enhanced, as expected in a compression region.

Previously, the observations of CIRs closest to the Sun had been made by the Helios space probe at 70 solar radii. Helios saw well developed CIRs, but without the forward and reverse shocks seen further out. The use of EISCAT has allowed CIRs to be seen much closer to the Sun. Observation were made of source 0431p206 on three days in May 1996 at three separate distances from the Sun. At 17.6 solar radii the fast stream velocity is 742 kms^{-1}, typical of a fast stream seen above a coronal hole. At 24.6 solar radii the fast stream velocity had fallen to 623 kms^{-1} and at 27.9 kms^{-1} it had fallen further to 507 kms^{-1}. This analysis seems to suggest that CIRs begin to form at distances beyond approximately 20 solar radii. However, the observations at these distances are in regions of strong scattering meaning that there is an increased uncertainty in interpreting the data. In this case, the weak scattering regime begins at approximately 25 solar radii and so it is possible to conclude with certainty that the CIRs begin to develop at this distance at least.

The maximum cross-correlation coefficient between the scintillations observed by two spaced antennas is a maximum when the two antennas lie in the same plane as the direction of flow of the solar wind. Observations are normally scheduled for such times on the assumption that this flow is exactly radial. However, when extended observations of interplanetary scintillation are made, so that the orientation of the baseline between the two sites varies significantly, the results provide strong evidence that maximum correlation corresponds to a direction of flow with a small but significant component that is non-radial. Figure 59 shows an example of how the maximum cross-correlation varies for different spacing of the antennas in the plane perpendicular to the radial. When a Gaussian curve is fitted to the data, it indicates that maximum correlation occurs for a perpendicular spacing of -9.8 km. This corresponds to a component of flow offset 1.5° away from radial in an equatorward direction.

Owing to the small size of the non-radial component, it was necessary to make a careful estimate of the random errors involved in the measurements and then use a Monte Carlo method to determine whether the apparent offsets were genuine or a result of random error. Out of eleven extended observations analysed so far, four show offsets of between 1° and 2° significant at 10% or less (i.e. with less than 10% chance that the result is due to random error) and in each case the offset is directed towards the equator.

Pulse Schemes

It has been discovered that Barker codes can be replaced by short alternating codes in phase coded pulse codes. In this way pulse codes with a high range resolution can be constructed, having no small range ambiguities, which necessarily appear when Barker codes are used (Nygrén et al, 1996)

The problem of finding long alternating codes for high-resolution experiments has been solved completely. The method was found by investigating the regular behaviour in the known strong alternating codes up to the length of 32 bits. It was observed that these codes follow a pattern which allows their construction from smaller elements in a straightforward manner. A mathematical formulation of this pattern was constructed, and a rigorous mathematical proof was given that a pattern of arbitrary length necessarily makes a strong alternating code. The search method can also be converted to a game greatly resembling ordinary dominoes, Figure 60. A complete search has been made up to the length of 1048576 bits and the longest code found consists of 4194304 bits (Markkanen and Nygrén, 1996, 1997; Nygrén and Markkanen, 1997).

At high snr, the self-noise makes an important contribution to the accuracy of the incoherent scatter measurements. Then the superiority of the alternating codes is not evident, and in some cases, multipulse methods are better. The performance deficit is mainly caused by covariances between the lag estimates. This is best seen in range integration where adding up 2 or 3 gates produces an increase of only 1.5 and 2, instead of 2 and 3 for independent observations.

Randomisation, i.e. multiplication of the bits in the alternating code by ±1 so that the same sequence is applied to all codes in the sequence, reduces the covariances significantly. The range integration then leads to a speed increase of 1.8 and 2.5, when adding two and three gates together, respectively. In practice the snr is neither low nor infinite, and calculations for realistic signal strengths are needed to assess to significance of randomisation. The speed increase varies from 1.1 to 1.25-1.4 for ESR and UHF experiments at typical electron densities, which means the a specifieded accuracy is obtained 20-30% faster than with a non-randomised experiment. Randomisation does not increase the work load of either the radar system or the data processing system.

Randomised alternating codes are also better than random codes. Both produce similar covariances within a single range gate, but random codes produce, unlike randomised alternating codes, covariances between the same lags at different ranges at a level of 20% (Lehtinen et al., 1997).

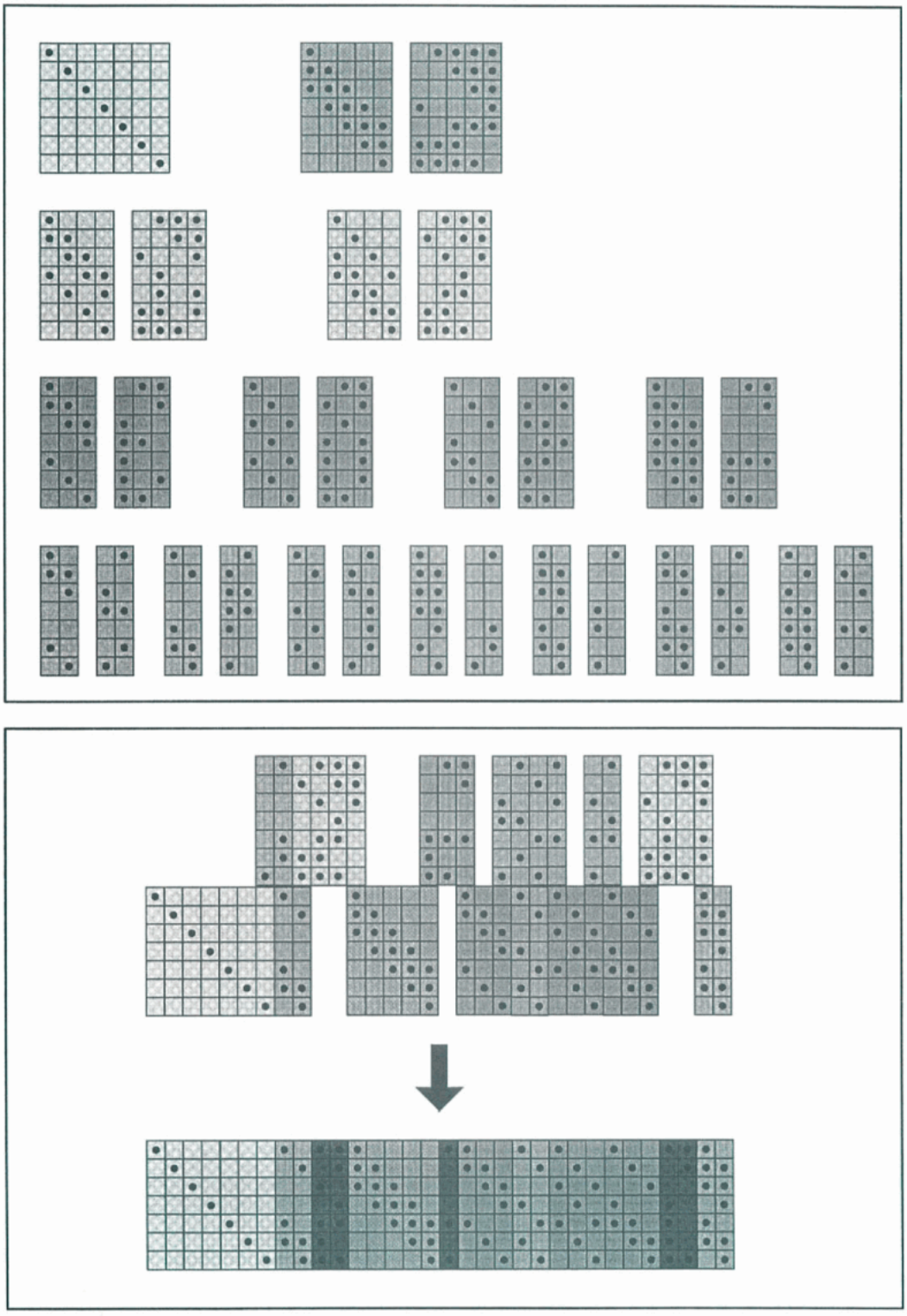

Figure 60: A 32-bit domino game. The bones of the game are shown in the top panel and playing the game in the bottom panel. The idea is that the last and first columns of successive bones must be identical. When the top row of the final setting is wiped off, the dot pattern in each column is the binary presentation (with the least significant bit on the top) of the Walsh index of the respective column of the sign matrix of the code.

Data Analysis Techniques

The "full profile" technique can be efficiently used to extract independent information on the ion composition and temperature from incoherent scatter data. The implementation was designed for EISCAT CP-1 and CP-2 data analysis where the fitted data are the gated lag profile cross products, namely the plasma correlation functions. The first key point in the method is that the high resolution/low signal (coded pulse) and low resolution/high signal (long pulse) data must be fitted simultaneously. The second is that a suitable functional model of ion composition profile, with a sufficient amount of flexibility to include all possible variations, is essential (Cabrit and Kofman, 1996).

CP-1 data from 1987 to 1994 have been processed using this 'global fit' method, introducing another analytical function to model the ion composition profile and choosing the best method to select the initial conditions for the 'full profile' procedure. A statistical analysis of the results was done to obtain averages of electron concentration and temperature, ion temperature, composition and bulk velocity. The behaviour of the parameters defining the ion composition profiles - z_{50} (transition altitude between atomic and molecular ions) and Dz (width of the profile) have been described for various seasons and for high and low solar activities (Litvine, Kofman and Cabrit).

An interesting behaviour was observed that still needs a detailed explanation. z_{50} and dz show anticorrelation in summer and correlation in winter. This means that when z_{50} decreases, dz also decreases in winter and dz has the opposite behaviour in summer. Spring and autumn are transition periods between these two opposite behaviours. A qualitative explanation of the temporal behaviour of the transition altitude (z_{50}) between molecular and atomic ions and the width (dz) of the composition profile has been proposed which supports the results. The correlation and anti-correlation between these two quantities are explained by the gradients of electron density and of ion production.

Comparison with the IRI model shows similarities in the shape (except in winter) of z_{50} and dz parameters but the values and the exact behaviour are really different. The profiles are quite different. The main reason for these differences comes from the fact that the IRI model is built on a small number of measurements of the composition especially for the auroral zone. Compared with Lathuillere and Pibaret (1992), different seasonal variations of the behaviour of the composition parameters, mainly for the width of the transition region between molecular and atomic ions are observed. The spatial resolution of the "full profile" analysis is much better than the resolution of the earlier analysis and is free from gradient effects. This can explain the differences.

Plasma parameters are derived by GUISDAP, and other analysis programs, on the assumption that the plasma is in thermal equilibrium. However, in the cusp and polar cap regions the ionospheric plasma is often strongly non-Maxwellian and can display significant small scale structure, so it is important not to take standard analysis results at face value.

Accordingly, some raw data from October 10, 1996 have been subjected to visual inspection. The raw lag profile data are range gated into 360 μs autocorrelation functions, Fourier transformed into the power spectral domain, and plotted in false colour. As an example, three consecutive 10 second averages are shown in Figure 61. There is a pronounced and persistent spectral asymmetry at 200 to 220 km altitude, reminiscent of earlier EISCAT and quite possibly a signature of a non-Maxwellian velocity distribution. Another possibility is that the spectra have been distorted through the presence of unresolved velocity shears within the scattering volume.
The gate separation in the diagram is 3 km, but as the data are measured with a 360 μs transmitter pulse, every gate represents a smoothed average over 47 km in altitude, or about one half the scale height of the ionised component of the atmosphere at 250 km. For an equilibrium ionosphere the total signal power is therefore expected to vary smoothly from one gate to the next. Instead, one observes a power dip at about 280 km and a significant short-scale power variability with altitude. As the snr is close to unity, the noise variance is of the order of a few percent, but the observed variability is much larger and statistically significant. The data can therefore only be understood in terms of a very irregular, even "patchy", electron density profile with significant variability on scales of a few kilometres.

It is evident from these and other similar observations that full reduction of ESR data to plasma parameters will be a nontrivial matter. On the other hand, a wealth of non-equilibrium ionospheric science will result.

In magnetically perturbed periods, the ion-velocity distribution-function also departs from a Maxwellian, and therefore the classical analysis of incoherent scatter spectra does not provide accurate estimates of the ionospheric parameters. Two models of non-Maxwellian distribution

function have been extensively compared: the polynomial expansion approximation which is a solution of the Boltzmann equation, and a numerical distribution based on a Monte Carlo method. Both approaches lead to identical results for electric fields up to 100 mVm^{-1} and for the two ion species O^+ and NO^+. These comparisons have resulted in new collision cross-section models depending on the electric field strength for use in the polynomial expansion approximation model (Gaimard 1996, Gaimard, St. Maurice, Lathuillere and Hubert).

work with enough accuracy. Howevre, taking advantage of the tristatic capabilities of EISCAT, and the fact that in the case of aspect angles of about 21°, both NO^+ and O^+ ion velocity distribution function are very close to a Maxwellian, a new experimental strategy has been proposed. The aim of this strategy is to to measure objectively the predicted difference between the temperature of the two ion species in the presence of moderate electric fields (Hubert et al., 1996; Leblanc, Gaimard, St. Maurice, Lathuillere and Hubert).

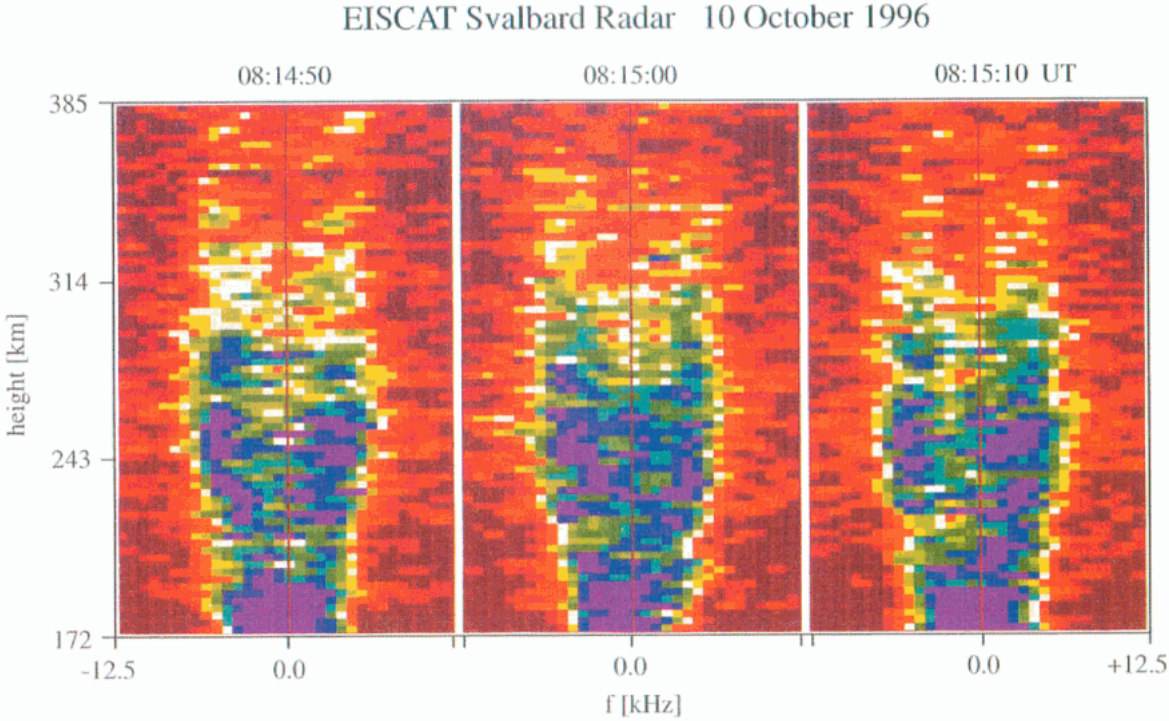

Figure 61: Spectrograms of three consecutive 10 s GUP0 raw data averages, taken with the ESR antenna pointing along the magnetic field. The colour code represents signal power on a linear scale.

A new analysis of incoherent scatter spectra, based on this analytical ion velocity distribution function model (Gaimard et al., 1996), has been used to calculate the ion composition at the onset of a magnetic substorm on 24 March 1995.

At this time the electric field was 70 mVm^{-1} and the transition altitude between molecular and oxygen ions reaches 270 km. A very good agreement has been obtained with the simulation done with the TRANSCAR ionospheric model, provided a 30% increase of the MSIS N_2 density and a 60% decrease of the oxygen density were used as model inputs (Lathuillere et al. 1997).

A search has been made for a way to derive the plasma parameters from incoherent scatter spectra without any a-priori model. It was found that it is only in a pure ionosphere composed of O^+ ions or of NO^+ ions that a non-constrained routine can

New characteristics of the O^+ ion distribution in a background of atomic neutrals subjected to intense external cross electromagnetic forces have also been found. The one dimensional distribution function along the magnetic field displays a core-halo shape which can be accurately fitted by a two Maxwellian model at different temperatures. The Maxwellian shape for an angle of 21°± 1° has been confirmed at the accuracy level of Monte Carlo simulations (Hubert and Leblanc, 1997).

In the presence of two ions, Incoherent Scatter results depend markedly upon the ion composition model used in the data analysis. Transformation formulas were proposed in the past for applying composition-dependent correction factors to retrieve the basic ionosphere parameters (namely the electron concentration and temperature, and the electron to ion

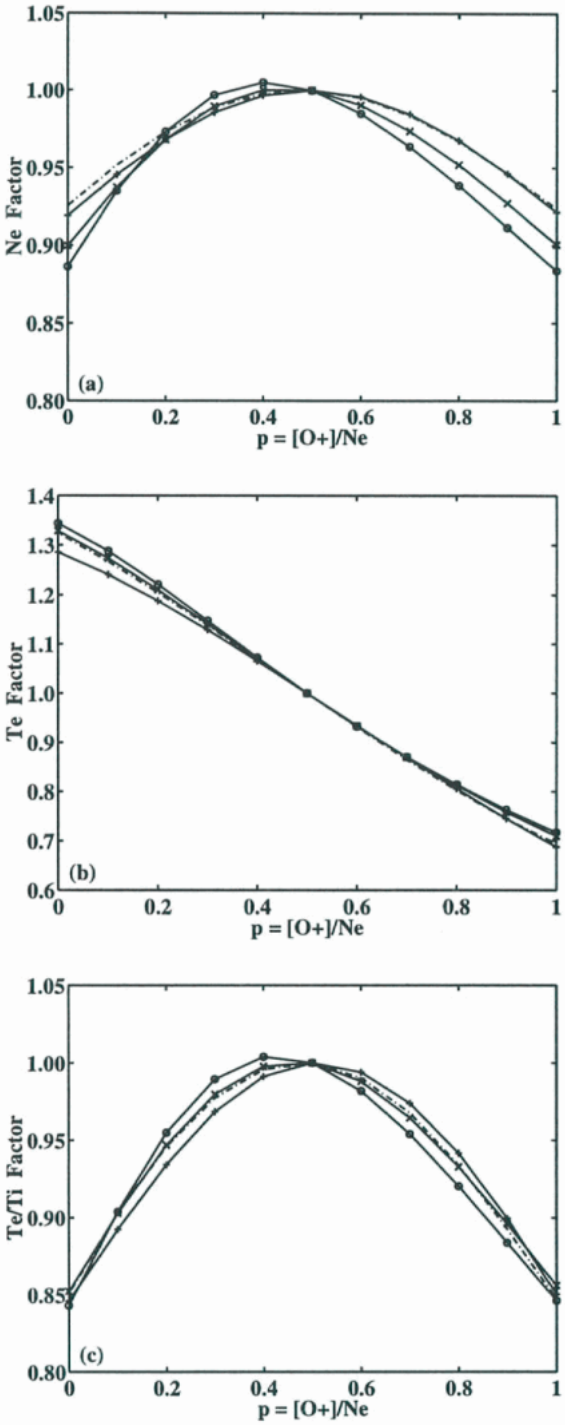

Figure 62: Correction factor for the electron density N_e (1a), for the electron temperature T_e (1b) and for the $r=T_e/T_i$ ratio (1c). These factors are normalized for a reference composition parameter p=0.5. The Waldteufel correction factors, normalized in the same way, are shown for comparison as dotted-dashed curves. Curves labelled with + ,x and o symbols stand for $[T_e/T_i]ref$ = 1, 2 and 3, respectively.

temperature ratio). Such formulas were aimed to avoid rerunning the analysis for a new ion composition which differs from the one used in the initial analysis. The domains of validity of these formulas have been investigated, in particular with respect to their electron to ion temperature ratio dependency. A generalised bi-dimensional polynomial formulation was developed, which gives results which differ from a full analysis by less than 0.2% as compared with a full analysis, Figure 62. This is valuabele in numerical model vs. data comparisons in the F1-region where the composition problem is crucial (Alcaydé et al, 1996).

The Svalbard Radar (ESR)
EISCAT technical highlight of the biennium

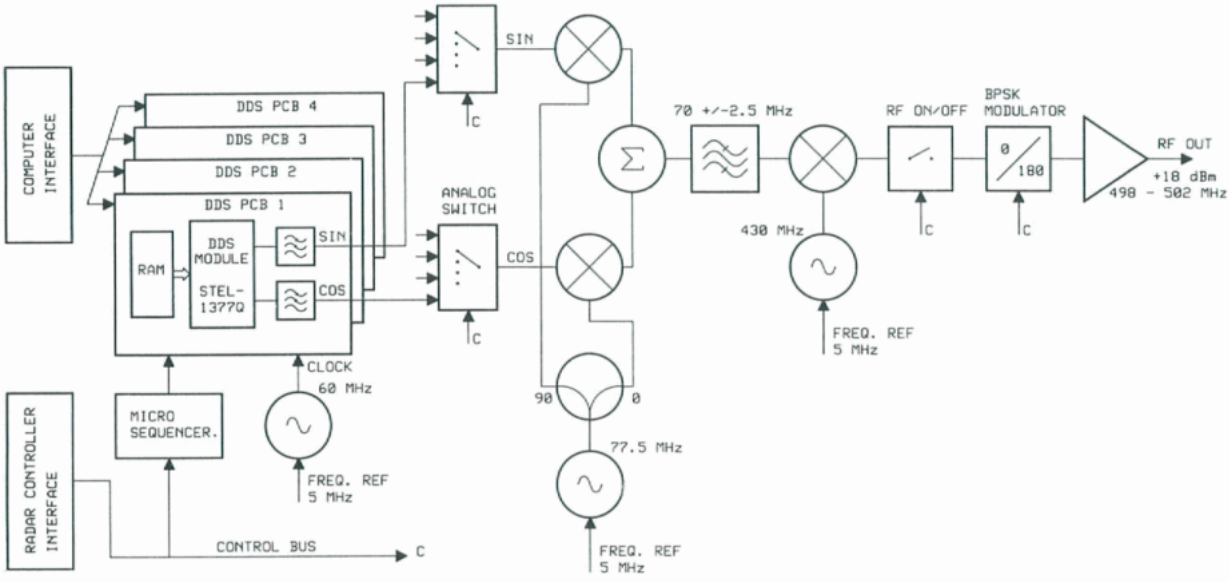

Figure 63: Schematic circuit diagram of the EISCAT Svalbard Radar (ESR) exciter

On August 22, 1996, Phase I of the EISCAT Svalbard Radar (ESR) was officially inaugurated. This event marked the successful end of a four-year race against the clock by the staff of EISCAT, charged with constructing and commissioning the new radar on Spitsbergen in time to match the start of scientific operations of the ESA Cluster programme.

In many ways, the ESR project represents a technological quantum leap for the Association. Novel and unconventional techniques have been successfully applied to almost all parts of the new radar, resulting in a very high performance system. The experience gained during the design, construction and commissioning of the ESR will certainly prove invaluable during the upcoming modernisation of the mainland stations. There follows below a technical overview of the Svalbard radar system. Interested readers, desiring more in-depth information, are referred to the "official ESR system paper", which appeared in Radio Science 32, no. 6, pp. 2283 - 2307 (1997).

Transmitter

The primary RF waveform is generated at low power by a direct digital synthesis (DDS) unit (Figure 63). Output signals from four independent DDS units are fed to an analog multiplexer, controlled by the transmitter radar controller. This permits phase-coherent switching between up to four frequencies, if desired. In addition, each source can be loaded with a new frequency in less than a microsecond, so permitting the execution of very complicated radar algorithms that combine clutter-free multi-frequency, within-pulse correlation measurements of overspread targets with single or dual frequency, pulse-to-pulse measurements of underspread targets.

The DDS signal is translated to the 500 MHz range by mixing in two steps. RF on-off switching and 0/180° phase modulation are performed after the second mixer. The modulated 500 MHz signal is amplified to about +18 dBm and supplied to the power amplifiers

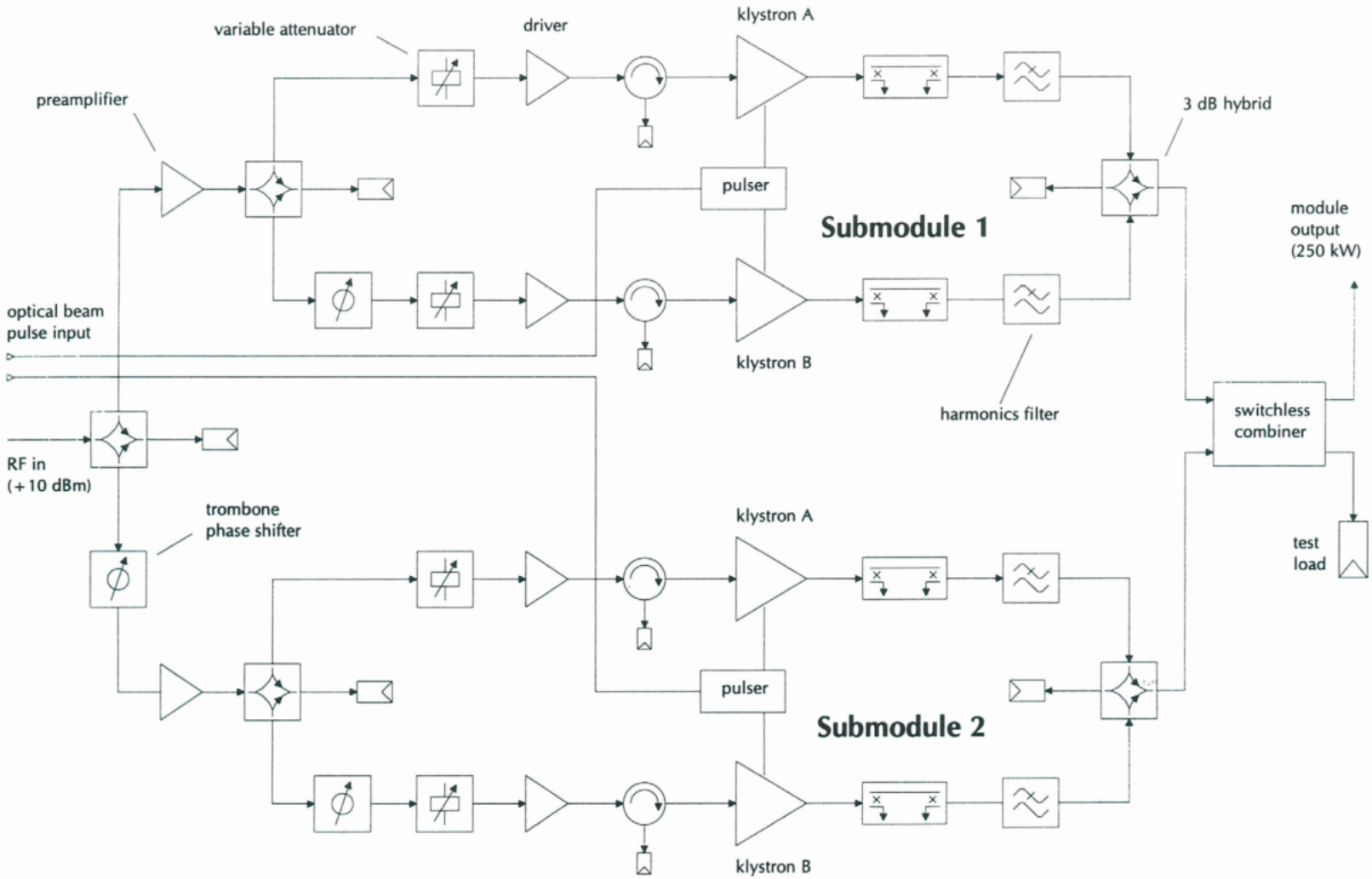

Figure 64: Block Diagram of basic 250-kW ESR transmitter module

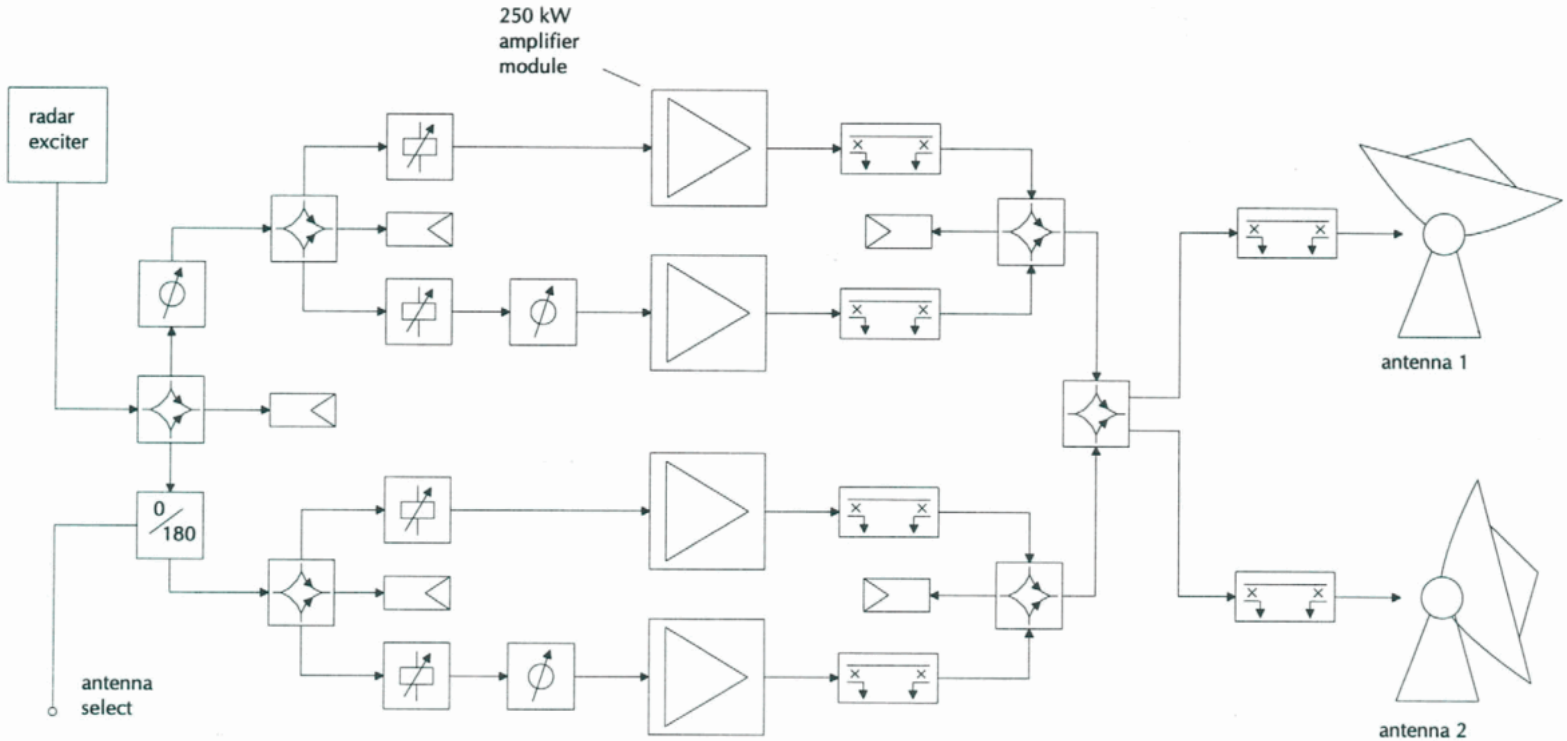

Figure 65: Block diagram of the envisaged phase II (1-MW, two-antenna) system. The full output power can be switched between two antennas on a pulse-to-pulse basis by reversing the phase of the RF drive to one half of the transmitter

These are slightly modified UHF TV transmitters, using 64 kW TV klystrons as the active devices. In Phase I of the ESR implementation, four transmitters generate a nominal 500 kW of RF power. A contract for upgrading the system to the 1 MW (Phase II) level by the addition of another four transmitters has been placed. This upgrade will come on line at the end of 1997.

In each transmitter, the signal is first boosted by a solid state driver and then amplified to a peak power of 2 x 64 kW by two paralleled klystrons. A stack of 45, series-connected insulated-gate bipolar transistors switches the klystron modulating anode voltage between about –700 V and the full beam voltage in less than 10 µs, thus allowing operation down to altitudes of a few kilometres for stratospheric observations. The system can be run at up to 2 ms pulse lengths and 25% duty cycle, the highest ever used in a monostatic incoherent scatter radar.

A 250 kW "transmitter module" (Figure 64) is formed by combining two transmitters through a four-port switchless combiner (SC) network. By changing the SC settings, the output power can be divided between the module output and a test load in any desired ratio. If one klystron should fail, most of the available power can still be directed to the output by resetting the SC appropriately.

In the Phase II transmitter system, shown in Figure 65, the full transmitter power can be switched between the two outputs of the final power combiner by reversing the phase of the low-level RF drive supplied to one half of the system. When the second antenna is added, this feature will be used to alternate transmissions between the two antennas on a pulse-to-pulse basis.

The klystron beam power supplies are fitted with storage capacitors, which are charged to about 25 kV during the receiving part of the radar cycle. When RF is being transmitted, each klystron draws a current in the order of six amperes from the capacitors, causing the beam voltage to drop at a rate of a few kilovolts per millisecond. This induces a phase lag in the output signal, which eventually shows up in the received data as a systematic negative Doppler bias. Measurements made on the ESR transmitters show a mean shift of about -25 Hz, corresponding to a -10 ms^{-1} target speed error. Rather than attempting to compensate for this effect in the exciter, a sample of the transmitted RF waveform is injected into the receiver and processed using the same algorithms as used for processing the scatter signals. In this way, the instantaneous frequency offset is continuously measured and recorded together with the scatter data, thus allowing its removal during the analysis. The technique is also very helpful for spotting system malfunctions.

Antenna

The ESR antenna (Figure 66) is a fully steerable, 32 m diameter dual reflector Cassegrain system, set up to transmit right-hand circular (RHC) and receive left-hand circular (LHC) waves. Thanks to a successful simultaneous full-wave optimisation of both the main and secondary reflector shapes, it provides high gain and low noise performance. Tests using celestial calibrator sources indicate a gain of (42.5+/- 0.2) dBi. The antenna noise temperature is below 30 K at all elevations greater than 15° and even drops to about 20 K at certain azimuths.

The antenna is very fast (2.8° s^{-1}). It can move a full 180° in elevation through the zenith, and its control computer automatically selects the shortest path to a new pointing direction. Full pointing performance (<0.01° wobble) is retained up to a wind speed of 20 ms^{-1}, and the antenna can drive into the safety stow position at winds of over 27 ms^{-1}. A tower mounted weather station monitors the wind speed and takes command of the antenna whenever the wind speed exceeds 27 ms^{-1} for more than ten seconds; it is then automatically stowed and shut down. Several control systems alarms can also automatically drive the antenna to the stow position.

Since the antenna is electrically small (53λ), it exhibits very strong feedhorn-subreflector coupling, and a large fraction of the transmitted power is reflected from the subreflector back into the horn and returned through the OMT receiver port. Measurements on the completed antenna show that the effective TX to RX port isolation is only -19 dB. When transmitting 1 MW of power, more than 11 kW returns to the OMT receiver port. The specially designed ESR receiver protector diverts this power into a waster load, where it is dissipated harmlessly, thus helping to keep the cross-polarisation in the main beam below -30 dB. At the same time, it provides better than -90 dB TX-to-RX isolation to prevent receiver degradation and burnout.

Figure 66: Aerial view of the EISCAT Svalbard radar, looking down the Advent valley toward WNW

The ESR is located close to the approach to the Longyearbyen airport, and special precautions have to be taken to ensure that the main radar does not illuminate approaching aircraft. An aircraft detection system comprising a low power C-band radar transceiver and a pyramidal horn antenna with a half-power beam-width of 10° is installed in the main antenna. The horn is mounted at the apex of the sub-reflector tripod and points coaxially with the main beam. The video output from the radar transceiver is processed in a dedicated PC. A thresholding routine disables the main radar transmitter and triggers an alarm whenever echoes are detected above a preset level. The system is failsafe; the main transmitter cannot be activated unless the aircraft detection radar is running and detecting no targets. If it is turned off, the main system stops automatically. The failsafe feature includes a link to the airport control tower, providing the air traffic controllers with radar status information in real time and a mechanism for turning off the ESR in an emergency.

Receiver

Figure 67 shows a schematic diagram of the receiver. To minimise losses, the preamplifier and first mixer are located in the antenna apex cabin. The first amplifier stage is cooled to 30 K physical temperature by a closed circuit helium refrigerator. The second stage operates at room temperature. The preamplified signal is first routed through a switching network where the transmitted RF waveform samples are introduced. In the first mixer, the signal is down-converted to a first IF at (70+/-2.5) MHz and amplified, before being sent down to the receiver back end in the control room. The receiver noise temperature is less than 15 K, of which about 1.5 K is contributed by the second and subsequent stages.

In the back end, the broadband first IF signal is further down-converted and passed through a 7.5+/-1.9 MHz anti-aliasing filter. The band-limited signal is amplified by a high performance 43 dB amplifier and digitised to 12 bits of resolution by a wide-band A/D converter running at 10 MHz sampling rate; the technique is known as constructive undersampling.

At this point, the ESR receiver goes fully digital. Channel separation and all further processing of the individual channels (translation to baseband, real-to-complex conversion, decimation, low-pass filtering and resampling) are all done in the digital domain. A number of extremely important advantages result: the A/D conversion gain is the same for all frequencies and channels, DC offset and mains related hum interference disappear, and because real-valued sampling is used, spectral image problems introduced by quadrature detector unbalance are nonexistent. The post-detection filter impulse responses also become totally predictable and stationary.

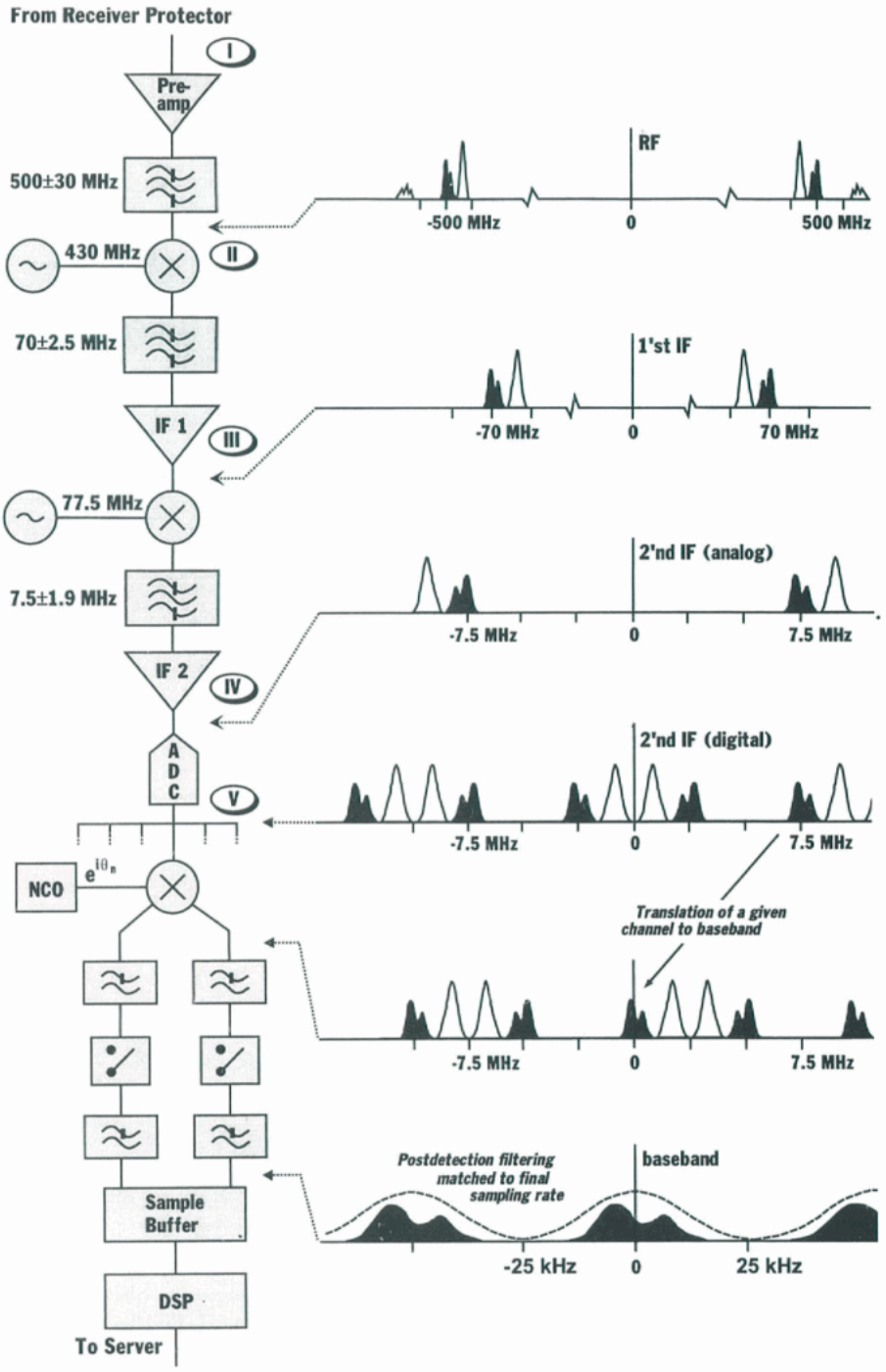

Figure 67: Functional block diagram of the ESR receiver. For clarity, signal flow through only one channel board is illustrated

The A/D output data stream is split into six branches, each feeding a "channel board". This EISCAT in-house design uses application specific digital signal processing chips to implement a digital single channel, tuneable IF-to-baseband translator, real-to-complex data converter, decimator, FIR filter, sampling gate and swinging buffer output data memory on a 6U Eurocard. To recover an individual narrow-band signal (e.g. an ion line spectrum) from the composite data stream, a numerical local oscillator (NCO) in the digital down-converter is set to the corresponding IF frequency (to a resolution of 3×10^{-3} Hz) and the decimating FIR filter chips are loaded with an appropriate set of filter coefficients and decimation factors. The system permits an extreme degree of frequency agility. The NCO can be reprogrammed from a RAM frequency table in about 300 ns, so making it possible to use a single channel board to receive a theoretically infinite number of different frequencies in sequence. In some experiments, the NCOs are reprogrammed at the beginning of each radar cycle to match the new frequencies set in the exciter; thus, six channel boards do a job that would have required at least eight physical IF channels in a more conventional receiver back end.

Signal processing

When the ESR system was being specified in 1992/1993, array processors, hardware FFT processors and fast, programmable digital signal processor systems were already widely available as commercial VME bus board level products, and used for signal processing at other incoherent scatter facilities. Against this background, it was decided to construct the ESR DSP system using commercial hardware throughout, and to make it modular, so that it could be upgraded as needed.

Figure 68 shows a diagram of the ESR Phase I receiver back end and DSP. The six receiver channel boards are organised as two groups of three. Each group comprises a DSP unit and a controller board, which arbitrates the communication between the DSP, the channel boards and the radar controller. The DSP units are LSI dBV42 VME boards, equipped with two 50 MHz Texas Instruments TMS 320C40 signal processors and a total of 29.5 Mbyte of RAM.

One of the 'C40 processors controls all data transfers to and from the channel boards and handles a number of housekeeping tasks. When the system is being set up for an experiment, the main server downloads NCO frequency tables and filter coefficient values to the DSP, which then accesses the individual channel boards and stores the values in local RAM. When the experiment is running, raw data from one channel board at a time is read by the DSP on a cycle-by-cycle basis. The DSP then processes pairs of complex raw data samples into complex autocorrelation coefficient estimates ("lag profiles") and averages these over a number of radar cycles. In terms of processing power, each two-processor DSP board is the equivalent of one of the old EISCAT digital correlators, used at the mainland sites. The experiments run so far use about 50% of the DSP bandwidth, or less, thus leaving some room for experiment code refinements.

At the end of an integration period, the data are transferred to the main server for post-processing and storage. Since the DSP architecture allows processing and data transfer to run concurrently, data can be recorded continuously with no holes in the time series. If the lag profile data require decoding, a FIR filter C program running on the server performs this. The data are merged with a set of auxiliary parameters (antenna pointing direction, transmitter power etc.) and written to hard disk files.

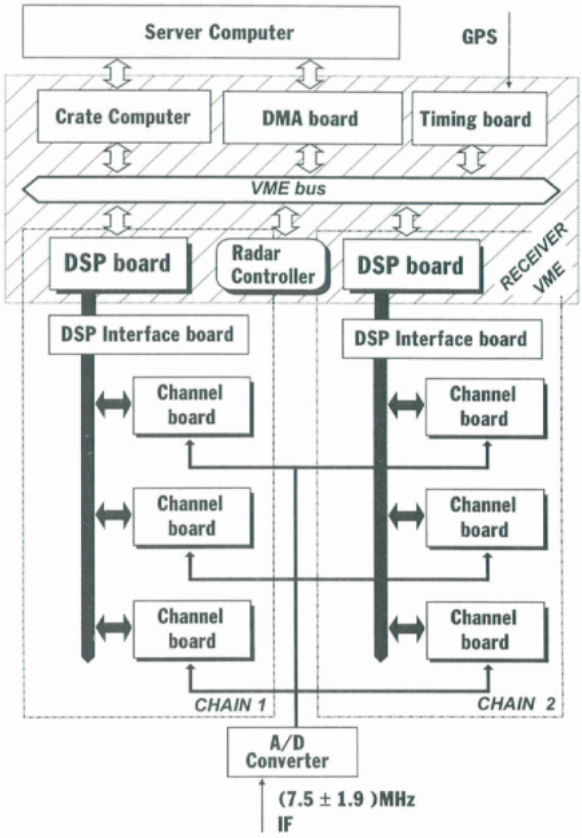

Figure 68: Block diagram of the digital receiver back end

Computer system

The ESR network and process control computer system is shown in Figure 69. All control hardware conforms to the VME bus protocol and packaging standards. An Ethernet based local area network handles all computer intercommunication. The server and all process computers are connected to a switched Ethernet hub, which gives process-control related traffic priority over other network traffic. The server-hub link runs at 100 Mbit/s and all others at 10 Mbit/s. The router for the external site network connection is also tied into the hub, thus eliminating competition for bandwidth between control processes and interactive users.

To avoid the burden of having to maintain a mixed operating system environment, the ESR computer system does not attempt to provide fully deterministic real time behaviour. Instead, fast processor hardware and the multitasking capabilities of Solaris 2 provide the rapid response required for data recording and fast experiment context switching. A six CPU,

85 MHz SPARCserver 1000E handles experiment control and monitoring, raw data decoding and storage, data integration, data analysis, storage of analysed data and data display. It also performs file server duty for the receiver and transmitter VME crate computers, which are diskless SPARCstation 2 compatibles running under Solaris. The ACU is an exception to the Solaris-oriented philosophy. It contains a Motorola 68040, running the OS-9 real time operating system from local hard disk. If required, the ACU can be run in a stand-alone mode and operate the antenna independently of the main computer network.

The receiver VME crate has a 16 bit parallel DMA link to the server. In normal operation, the network connection is used for control and monitoring, while DSP output data are transferred to the server on the DMA link at rates approaching 5 MByte/s. A fallback configuration, using the network both for data transfer and system control, is also available, but can only handle low data transfer rates. A disk array, presently fitted with 12+12 GB of hard disk space, provides intermediate storage for over 60 hours of GUP0/GUP1 type raw data. For safety, the disks are mirrored. Exabyte and DAT tape drives are used to off-load data from the disks for transfer to the mainland, dissemination and archiving.

Two radar controllers, one each in the transmitter and receiver VME crates, handle synchronous control of time-critical hardware functions at sub-microsecond time resolution. These EISCAT-designed, VME compatible units contain two 256 K banks of fast RAM, which are loaded by the control computer before the start of an experiment. One of the banks, 32 bits wide, stores the instruction table, i.e. the actual bit patterns that are mapped out onto the hardware control lines. The other bank, 24 bits wide, stores the associated dwell count table, i. e. a table of numbers telling for how many clock cycles each instruction bit pattern should remain set before the next one in sequence is accessed. At the end of an instruction sequence, the unit recycles the sequence from the beginning until a pre-programmed number of loops are exhausted; it then commands the DSP to stop averaging data, dump its memories and begin a new integration. The readout logic is clocked at a 10 MHz rate, and new commands can thus be issued every 100 ns.

A GPS-derived IRIG-B time code signal is broadcast to all VME crates. Commercial VME boards decode the IRIG-B and provide absolute UTC to the crate computers. The GPS receiver is also used to discipline a high performance 10 MHz crystal oscillator, which generates a site-wide reference frequency signal. This is distributed to all VME crates and processed to generate a range of phase coherent clock signals.

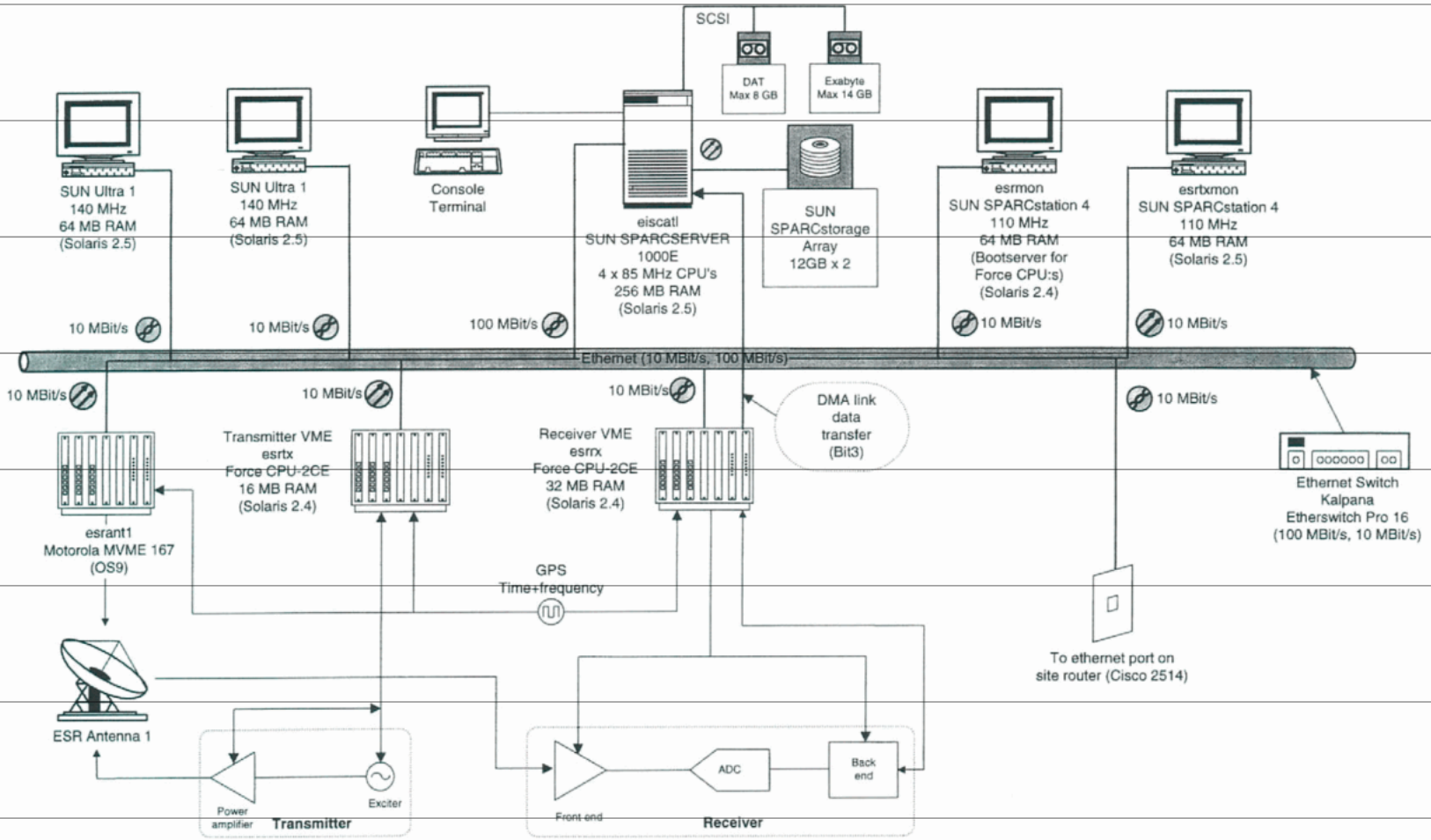

Figure 69: Schematic diagram of the ESR control computer network

Publications

Journals and Books, 1996

Alcaydé, D., J. Fontanari, P.-L Blelly and C. Lathuillere, On the influence of ion composition in the F1-region on incoherent scatter spectra, Ann. Geophys. 14, 1526-1529, 1996.

Aikio, A.T. and K.U. Kaila, A substorm observed by EISCAT and other ground-based instruments - evidence for near-Earth substorm initiation, J. atmos. terr. Phys., 58, 5-22, 1996.

Aruliah, A.L., A.D. Farmer, D. Rees, and U. Brandström, The seasonal behaviour of high-latitude thermospheric winds and ion velocities observed over one solar cycle. J. Geophys. Res., 101, 15701-15711, 1996.

Aruliah, A.L., A.D. Farmer, T.J. Fuller-Rowell, M.N. Wild, M. Hapgood and D. Rees, An equinoctial asymmetry in the high-latitude thermosphere and ionosphere, J. Geophys. Res.,101, 15713-15722, 1996.

Blelly, P.-L., J. Lilensten, A. Robineau, J. Fontanari and D. Alcaydé, Calibration of a numerical ionospheric model with EISCAT observations, Ann. Geophys., 14, 1375-1390, 1996.

Blelly, P.-L., A. Robineau and D. Alcaydé, Numerical modelling of intermittent ion outflow events above EISCAT, J. atmos. terr. Phys., 58, 273-285, 1996.

Blelly, P.-L., J. Lilensten, A. Robineau, J. Fontanari and D. Alcaydé, Calibration of a numerical ionospheric model with EISCAT observations, Ann. Geophys., 14, 1375-1390, 1996.

Blelly, P.-L., A. Robineau and D. Alcaydé, Numerical modelling of sporadic ions outflow events above EISCAT, J. atmos. terr. Phys., 58, 273-285, 1996.

Blix, T.A., E.V. Thrane, S. Kirkwood and R.N. Sudan, Experimental evidence for unstable waves in the lower E/upper D-region excited near the bisector between the electric field and the drift velocity, Geophys. Res. Lett., 23, 2137-2140, 1996.

Breen, A.R., W.A. Coles, R. Grall, U.P. Løvhaug, J. Markkanen, H. Misawa and P.J.S. Williams, EISCAT measurements of interplanetary scintillation. J. atmos. terr. Phys., 58, 507-519, 1996.

Breen, A.R., W.A. Coles, R. Grall, M.T. Klinglesmith, J. Markkanen, P.J. Moran, B. Tegid and P.J.S. Williams, EISCAT measurements of the solar wind. Ann. Geophys., 14, 1235-1245, 1996.

Breen, A.R., P.J.S. Williams, A. Etemadi V.N. and Davda, Uncertainties in measurements of electron temperature and the estimation of F-region electron heat conduction from EISCAT data, J. atmos. terr. Phys., 58, 145-159, 1996.

Brekke, A. and Y. Kamide, On the relationship between Joule and frictional heating in the polar ionosphere, J. atmos. terr. Phys., 58, 139-144, 1996.

Bremer, J., P. Hoffman, A.H. Manson, C.E. Meek, R. Rüster and W. Singer, PMSE observations at three different frequencies in Northern Europe during summer 1994, Ann. Geophys., 14, 1317-1327, 1996.

Burns, C.J. and J.K. Hargreaves, The occurrence and properties of large-scale irregular structures in the auroral F-region, J. atmos. terr. Phys., 58, 217-232, 1996.

Bösinger, T., K. Kaila, R. Rasinkangas, P. Pollari, J. Kangas, V. Trakhtengerts, A. Demekhov and T. Turunen, An EISCAT study of a pulsating auroral arc: simultaneous ionospheric electron density, auroral luminosity and magnetic field pulsations, J. atmos. terr. Phys., 58, 23-35, 1996.

Cabrit, B. and W. Kofman, Ionospheric composition measurement by EISCAT using a global fit procedure, Ann. Geophys., 14, 1496-1505, 1996.

Cabrit, B., H. J. Opgenoorth and W. Kofman, Comparison between EISCAT UHF and VHF backscattering cross-section, J. Geophys. Res., 101, 2369-2376, 1996.

Carlson, H., Incoherent scatter radar mapping of polar electrodynamics, J. atmos. terr. Phys., 58, 37-56, 1996.

Collis, P.N., The high latitude D-region and mesosphere revealed by the EISCAT incoherent scatter radars during solar proton events, Adv. Space Res., 18, (3)83-(3)92, 1996.

Collis, P.N., J.K. Hargreaves and G.P. White, A localised co-rotating auroral absorption event observed near noon using imaging riometer and EISCAT, Ann. Geophys., 14, 1305-1316, 1996.

Cowley, S.W.H. and M. Lockwood, Time-dependent flows in the coupled solar wind-magnetosphere-ionosphere system, Adv. Space Res., 18, (8)141-(8)150, 1996.

Davis, C.J. and M Lockwood, Predicted signatures of pulsed reconnection in ESR data, Ann. Geophys., 14, 1246-1256, 1996.

Diloy, P.Y., J. Fontanari, D. Alcaydé, U.P. Løvhaug and A.P. van Eyken, Is EISCAT able to determine the H^+ temperature and velocity? Numerical simulations, J. atmos. terr. Phys., 58, 287-295, 1996.

Diloy, P.Y., A. Robineau, J. Lilensten, P.-L. Blelly and J. Fontanari, A numerical model of ionosphere including the E-region above EISCAT, Ann. Geophys., 14, 191-200, 1996.

Eglitis, P.E., I.W. McCrea, T.R. Robinson, T.B. Jones, K. Schlegel, and T. Nygrén, Flow dependence of COSCAT spectral characteristics, J. atmos. terr. Phys., 58, 189-203, 1996.

Fontaine, D. and C. Peymirat, Large-scale distributions of ionospheric horizontal and field-aligned currents derived from EISCAT, Ann. Geophys., 14, 1284-1296, 1996.

Foster, C. and M. Lester, Observations of nightside auroral plasma upflows in the Fregion and topside ionosphere, Ann. Geophys., 14, 1274-1283, 1996.

Frey, H.U., G. Haerendel, S. Buchert and B.S. Lanchester, Auroral-arc splitting by intrusion of a new convection channel. Ann. Geophys., 14, 1257-1264, 1996.

Frey, H.U., G. Haerendel, D. Knudsen, S. Buchert and O.H. Bauer, Optical and radar observations of the motion of auroral arcs, J. atmos. terr. Phys., 58, 57-70, 1996.

Gaimard, P., C. Lathuillere and D. Hubert, Non Maxwellian studies in the auroral F-region: a new analysis of incoherent scatter spectra, J atmos. terr. Phys., 58, 415-433, 1996.

Gault, W.A., G. Thuillier, G.G. Shepherd and C. Lathuillere, Validation of O(1S) wind measurements by WINDII: the Wind Imaging Interferometer on UARS, J. Geophys. Res., 101, 10405-10430, 1996.

Gazey, N.G.J., M. Lockwood, M. Grande, C.H. Perry, P.N. Smith, S. Coles, A.D. Aylward and R.J. Bunting, EISCAT/CRRES observations: nightside ionospheric ion outflow and oxygen-rich substorm injections, Ann. Geophys., 14, 1032-1043, 1996.

Grall, R.R., W.A. Coles, M.T. Klinglesmith, A.R. Breen, P.J.S. Williams, J. Markkanen and R. Esser, Measurements of the solar wind speed in the south polar stream near the Sun, Nature, 379, 429-432, 1996.

Guio, P., N. Bjørnå and W. Kofman, Alternating-code experiment for plasma-line studies, Ann. Geophys., 14, 1473-1479, 1996.

Hall, C., Spatio-temporal predictions of polar mesospheric summer echoes, J. Geophys. Res., 101, 23491-23498, 1996.

Hansen, G. and U.-P. Hoppe, Investigation of the upper mesospheric dynamics under late polar summer conditions by EISCAT and LIDAR, J. atmos. terr. Phys., 58, 317-336, 1996.

Haerendel, G., B.U. Olipitz, S. Buchert, O.H. Bauer, E. Rieger and C. La Hoz, Optical and radar observations of auroral arcs with emphasis on small-scale structures, J. atmos. terr. Phys., 58, 71-84, 1996.

Hocke, K. and K. Schlegel, A review of atmospheric gravity waves and travelling ionospheric disturbances 1982-1995, Ann. Geophys., 14, 917-940, 1996.

Hocke, K, K. Schlegel and K. Kirchengast, Phases and amplitudes of TIDs in the high latitude F-region observed by EISCAT, J. atmos. terr. Phys., 58, 245-256, 1996.

Hubert, D., F. Leblanc and P. Gaimard, Current state-of-the-art for the measurement of non-Maxwellian plasma parameters with the EISCAT UHF facility, Ann. Geophys., 14, 1506-1512, 1996.

Huuskonen, A. and M. Lehtinen, General incoherent scatter analysis and GUISDAP error estimates valid for high signal strengths, J. atmos. terr. Phys., 58, 435-464, 1996.

Huuskonen, A., M. S. Lehtinen, and J. Pirttilä, Fractional lags in alternating codes: improving incoherent scatter measurements by using lag estimates at non—integer multiples of baud length, Radio Sci., 31, 245-261, 1996.

Isham, B., C. La Hoz, H. Kohl, T. Hagfors, T.B. Leyser and M.T. Rietveld, Recent EISCAT Heating results using chirped ISR, J. atmos. terr. Phys., 58, 369-384, 1996.

Jakowski, M., E. Sardon, E. Engler, A. Jungstand and D. Klähn, Relationships between GPS-signal propagation errors and EISCAT observations, Ann. Geophys., 14, 1429-1437, 1996.

Jenkins, B., R.J. Moffett, J.A. Davies and M. Lester, A nightside ion-neutral frictional heating event: ion composition and O^+ and NO^+ temperature anisotropy, Adv. Space Res., 18, (3)57 - (3)60, 1996.

Kagen, L.M., M.C. Kelley and R.A. Doe, Ionospheric electron heating by structured electric fields: Theory and experiment, J. Geophys. Res., 101, 10893-10907. 1996.

Kikuchi, T., H Lühr, T. Kitamura, O. Saka and K. Schlegel, Direct penetration of the polar electric field to the equator during a DP2 event as detected by the auroral and equatorial magnetometer chains and the EISCAT radar, J. Geophys. Res., 101, 17,161-17,173, 1996.

Kirchengast, G., K. Hocke and K. Schlegel, The gravity wave-TID relationship: insight via theoretical model-EISCAT data comparison, J. atmos. terr. Phys., 58, 233-243, 1996.

Kirkwood, S., Lower thermosphere mean temperatures, densities and winds measured by EISCAT : seasonal and solar-cycle effects, J. Geophys. Res., 101, 5133-5148, 1996.

Kirkwood, S., U. von Zahn and K.-H. Frike, EISCAT and ALOMAR review of potential for co-operative science, J. atmos. terr. Phys., 58, 337-348, 1996.

Kofman, W., C. Lathuillere and B. Pibaret, Neutral dynamics of the high latitude E-region from EISCAT measurements: a new approach, J. atmos. terr. Phys., 58, 337-348, 1996.

Kofman, W. and J.P. Saint-Maurice, Non thermal ionospheric plasma studies using incoherent scatter technique. J. atmos. terr. Phys., 58, 965-978, 1996.

Kohl, H., and M. T. Rietveld, Harmonics of the ion acoustic frequency in the heater induced ion spectrum, J. Geophys. Res., 101, 5391-5395, 1996.

Korenkov, Yu.N., V.V. Klimenko, M. Förster, V.A. Surotkin and J. Smilauer, Global modelling study (GSM TIP) of the ionospheric effects of excited N_2 convection and heat fluxes by comparison with EISCAT and satellite data for 31 July 1990, J. Geophys. Res., 14, 1362-1374, 1996.

Lanchester, B. S., K. Kaila and I. W. McCrea, Relationship between large horizontal electric fields and auroral arc elements, J. Geophys. Res., 101, 5075-5084, 1996.

Lehtinen, M. and A. Huuskonen, General incoherent scatter analysis and GUISDAP, J. atmos. terr. Phys., 58, 435-452, 1996.

Lehtinen, M., A. Huuskonen and J. Pirttilä, First experiences of full-profile analysis with GUISDAP, Ann. Geophys., 14, 1487-1495, 1996.

Lester, M., J.A. Davies and T.S. Virdi, High latitude Hall and Pedersen conductances during substorm activity in the SUNDIAL-ATLAS campaign, J. Geophys. Res., 101, 26719-26728, 1996.

Lewis, R.V., P.J.S. Williams, G.H. Millward and S. Quegan, Modelling the generation and propagation of atmospheric gravity waves by activity in the auroral electrojet, J. atmos. terr. Phys., 58, 807-820, 1996.

Lilensten, J, and P.O. Amblard, The use of time-frequency tools of signal processing for EISCAT data analysis, Ann. Geophys. 14, 1513-1525, 1996.

Lilensten, J, P.-L. Blelly, W. Kofman and D. Alcaydé, Auroral ionospheric conductivities: a comparison between experiment and modelling, and theoretical f10.7-dependent model for EISCAT and ESR, Ann. Geophys., 14, 1297-1304, 1996.

Lockwood, M., The relationship of day-side auroral precipitation to the open-closed separatrix and the pattern of convective flow, J. Geophys. Res., 102, 17475-17487, 1996.

Lockwood, M., S.W.H. Cowley and T.G. Onsager, Ion acceleration at both the interior and exterior Alfvén waves associated with the magnetopause reconnection site: signatures in cusp precipitation, J. Geophys. Res., 101, 21501-21515, 1996.

Lockwood, M. and C.J. Davis, An analysis of the accuracy of magnetopause reconnection rate variations deduced from cup ion dispersion characteristics, Ann. Geophys. 14, 149-161, 1996.

Lockwood, M., and C.J. Davis, On the longitudinal extent of magnetopause reconnection bursts, Ann. Geophys., 14, 865-878, 1996.

Lockwood, M. and J. Moen, Ion populations on field-lines within the low-latitude boundary layer: Theory and observations during a day-side transient event, Geophys. Res. Lett., 23, 2895-2898, 1996.

Lyatsky, W., E.G. Belova and A.B. Pashin, Artificial magnetic pulsation generation by powerful ground-based transmitter, J. atmos. terr. Phys., 58, 407-414, 1996.

Lühr, H., M. Lockwood, P. E. Sandholt, T. L. Hansen and T. Moretto, Multi-instrument ground-based observations of a travelling convection vortices event, Ann. Geophys. 14, 162-181, 1996.

Malnes, E., N. Bjørnå and T.L. Hansen, Anomalous echoes observed with the EISCAT UHF radar at 100-km altitude, Ann. Geophys., 14, 1328-1342, 1996.

Manninen, J., T. Turunen, A. Lubchich, E. Titova and T. Yahnin, Relations of VHF emissions to impulsive electron precipitation measured by EISCAT radar in the morning sector of the auroral oval, J. atmos. terr. Phys., 58, 97-106, 1996.

Markkanen, M. and T. Nygrén, A 64-bit strong alternating code discovered, Radio Sci., 31, 241-243, 1996.

Moen, J., D. Evans, H.C. Carlson and M. Lockwood, Day-side moving auroral transients related to LLBL dynamics, Geophys. Res. Lett, 23, 3247-3250, 1996.

Moen, J., M. Lockwood, P.E. Sandholt, U.P. Løvhaug, W.F. Denig, A.P. van Eyken and A. Egeland, Variability of day-side high-latitude convection associated with a sequence of auroral transients, J. atmos. terr. Phys., 58, 85-96, 1996.

Moffett, R.J., G.H. Millward, S. Quegan, A.D. Aylward and T.J. Fuller-Rowell, Results from a coupled model of the thermosphere, ionosphere and plasmasphere (CTIPM), Adv. Space Res., 18, (3) 33-39, 1996.

Namgaladze, A.A., O.V. Martynenko, A.N. Namgaladze, M.A. Volkov, Yu.N. Korenkov, V.V. Klimenko, I.V. Karpov and F.S. Bessarab, Numerical simulation of an ionospheric disturbance over EISCAT using a global ionospheric model, J. atmos. terr. Phys., 58, 297-306, 1996.

Namgaladze, A.A., A.N. Namgaladze and M.A. Volkov, Numerical modelling of the thermospheric and ionospheric effects of magnetospheric processes in the cusp region, Ann. Geophys., 14, 1343-1355, 1996.

Nilsson, H., S. Kirkwood and N. Bjørnå, Bistatic measurements of incoherent scatter plasma lines, J. atmos. terr. Phys., 58, 175-188, 1996.

Nilsson, H., S. Kirkwood, J. Lilensten and M. Galand, Enhanced incoherent scatter plasma lines, Ann. Geophys. 14, 1462-1472, 1996.

Nygrén, T., Studies of the E-region ion-neutral collision frequency using the EISCAT incoherent scatter radar, Adv. Space Res., 18, (3)79-(3)82, 1996.

Nygrén, T., Introduction to incoherent scatter measurements, 140 pp., Invers Publications, Sodankylä, 1996.

Nygrén, T., A. Huuskonen and P. Pollari, Alternating-coded multipulse codes for incoherent scatter experiments, J. atmos. terr. Phys., 58, 465-477, 1996.

Nygrén, T., M. Markkanen, M. Lehtinen, E.D. Tereshchenko, B.Z. Khudukon, O.V. Evstafiev and P. Pollari, Comparison of F-region electron density observations by satellite radio tomography and incoherent scatter methods, Ann. Geophys., 14, 1422-1428, 1996.

Nygrén, T., and T. Turunen, The ability of the EISCAT radar in measuring fast variations and low values of E-region electron density, Adv. Space Res., 18, (3)75-(3)78, 1996.

Olsson, A., A.I. Eriksson and P. Janhunen, On the current-voltage relationship in auroral breakups and westward-travelling surges, Ann. Geophys., 14, 1265-1273, 1996.

Olsson, A., M.A.L. Persson, H.J. Opgenoorth and S. Kirkwood, Particle precipitation in auroral breakups and westward travelling surges, J. Geophys. Res., 101, 24661-24673, 1996.

Osepian, A., S. Kirkwood and N. Smirnova, Energetic electron precipitation during auroral events observed by incoherent scatter radar, Adv. Space Res., 17, (11)149-(11)155, 1996.

Osepian, A. and S. Kirkwood, High-energy electron fluxes derived from EISCAT electron-density profiles, J. atmos. terr. Phys., 58, 479-488, 1996.

Palmer, J.R., H. Rishbeth, G.O.L. Jones. and P.J.S. Williams, A statistical study of polar mesosphere summer echoes observed by EISCAT, J. atmos. terr. Phys., 58, 307-315, 1996.

Pellinen-Wannberg, A and G. Wannberg, Enhanced ion-acoustic echoes from meteor trails, J. atmos. terr. Phys., 58, 495-506, 1996.

Pivovarov, V.G., Yu.L. Sverdlov, N.G. Sergeeva and V.N. Lytkin, A new approach to the determination of the E-region drift velocity using radar Doppler spectral shape, J. atmos. terr. Phys., 58, 489-494, 1996.

Pryse, S.E., L. Kersley and I.W. Walker, Blobs and irregularities in the auroral ionosphere. J. atmos. terr. Phys., 58, 205-216, 1996.

Pulinets, S.A., K.F. Yudakhin, D. Evans and M. Lester, the study of the ionospheric variability within the Euro-Asian sector during the SUNDIAL/ATLAS-1 mission, J. Geophys. Res., 101, 26759 - 26768, 1996.

Rietveld, M.T., P.N. Collis, A.P. van Eyken and U.P. Løvhaug, Coherent echoes during EISCAT UHF Common Programmes, J. atmos. terr. Phys., 58, 161-174, 1996.

Rietveld, M.T., E. Turunen, H. Matveinen, N.P. Goncharov and P. Pollari, Artificial periodic irregularities in the auroral ionosphere, Ann. Geophys., 14, 1437-1453, 1996.

Rinnert, K., Quasi-periodic precipitation with periods between 40 and 60 minutes, Ann. Geophys., 14, 707-715, 1996.

Robineau, A., P.-L. Blelly and J. Fontanari, Time-dependent models of the auroral ionosphere above EISCAT, J. atmos. terr. Phys., 58, 257-271, 1996.

Robinson, T.R., F. Honary, A.J. Stocker., T.B. Jones and P. Stubbe, First EISCAT observations of the modification of F-region electron temperature during heating at harmonics of the electron gyrofrequency, J. atmos terr. Phys., 58, 385-395, 1996.

Safargaleev, V., T. Turunen, W. Lyatsky, J. Manninen and A. Kozlovsky, Pre-break-up events in auroras and EISCAT data, Ann. Geophys., 14, 1170-1176, 1996.

Schoendorf, J., A.D. Aylward and R.J. Moffett, Modelling high-latitude electron densities with a coupled thermosphere-ionosphere model, Ann. Geophys., 14, 1391-1402, 1996.

Sedgemore, K.J.F., P.J.S. Williams, G.O.L. Jones and J.W. Wright, A comparison of EISCAT and Dynasonde measurements of the auroral ionosphere, Ann. Geophys. 14, 1403-1412, 1996.

Sergeev, V., A. Aikio, T. Bösinger, A. Brekke, L. Hakkinen, J. Kangas, R. Pellinen and P. Pollari, Night-time patterns of ionospheric convection, conductance, horizontal and field-aligned currents during a steady magnetospheric convection event, J. atmos. terr. Phys., 58, 107-120, 1996.

Smith, M.F. and M. Lockwood, The Earth's magnetospheric cusps, Rev. Geophys., 34, 233-260, 1996
St-Maurice J.P., W. Kofman and D. James, In-situ generation of intense electric fields in the lower ionosphere, J. Geophys. Res., 101, 335-356, 1996.

Stubbe, P., Review of ionospheric modification experiments at Tromsø, J. atmos. terr. Phys., 58, 349-368, 1996.

Stubbe, P., The ionosphere as a plasma laboratory, in Modern Ionospheric Science, eds. Kohl, Rüster and Schlegel, European Geophysical Society, Katlenburg-Lindau, FRG, 274-321, 1996.

Taylor, J.R., T.K. Yeoman, M. Lester, B. Emery and D.J. Knipp, Variations in the polar cap during intervals of substorm activity on March 20-21 1990 deduced from AMIE convection patterns, Ann. Geophys., 14, 879-887, 1996.

Turunen, E., Incoherent scatter radar contributions to high latitude D-region aeronomy, J. atmos. terr. Phys., 58, 707-725, 1996.

Volkov, M.A. and A.A. Namgaladze, Models of field-aligned currents needful to simulate the substorm variations of the electric field and other parameters observed by EISCAT, Ann. Geophys., 14, 1356-1361, 1996.

Walker, I.K., J.A.T. Heaton, L. Kersley, C.N. Mitchell, S.E. Pryse and M.J. Williams, EISCAT verification in the development of ionospheric tomography, Ann. Geophys., 14, 1413-1421, 1996.

Wannberg, G., A. Pellinen-Wannberg and A. Westman, An ambiguity-function-based method for analysis of Doppler decompressed radar signals applied to EISCAT measurements of oblique UHF-VHF meteor echoes, Radio Sci., 31, 497-518, 1996.

Williams, P.J.S., A. Etemadi, I.W. McCrea and H. Todd, Errors due to random noise in velocity measurements using incoherent-scatter radar, Ann. Geophys. 14, 1480-1486, 1996.

Wright, J.W., Argo P.E. and Pitteway M.L.V, On the radiophysics and geophysics of ionogram spread F, Radio Sci., 31, 349-366, 1996.

Theses, 1996

Davies, J.A., Ion frictional heating in the high-latitude ionosphere, Ph.D. thesis, University of Leicester, UK, 1996.

Gaimard, P., Fonctions de distribution de vitesses non-Maxwelliennes dans le plasma ionosphérique et application à la mesure par diffusion incohérente, Ph.D. thesis, Joseph Fourier University, Grenoble, France, 1996.

Karlsson, P., Production of a database for magnetospheric modelling, MSc thesis, Swedish Institute of Space Physics, IRF-Internal Note 035, October 1996.

Mitchell, C.N., Tomographic imaging of ionospheric electron density, Ph.D. thesis, University of Wales, Aberystwyth, UK, 1996.

Persson, M.A.L., Co-ordinated radar and satellite studies of magnetospheric substorms, Ph.D. thesis, Swedish Institute of Space Physics, Uppsala Division, IRF Scientific Report 233, May 1996.

Sedgemore, K.J.F., A comparison of EISCAT and Dynasonde measurements of the auroral ionosphere, Ph.D. thesis, Prifysgol Cymru Aberystwyth, UK, 1996.

Wallman, S., Preparation of a visual user interlace for a global database, containing satellite and ground-based geophysical data, M.Sc. thesis, Swedish Institute of Space Physics, IRF-Internal Note 034, October 1996.

Wright, D.M., HF Doppler observations of ULF waves: system development and high latitude results, Ph.D. thesis, University of Leicester, UK, 1996.

Proceedings, Reports, etc., 1996

Blelly, P.-L., A. Robineau, J. Lilensten, and D. Lummerzheim, 8-moment fluid models of the terrestrial high latitude ionosphere between 100 and 3000 km, in Solar Terrestrial Energy Program (STEP): Handbook of Ionospheric Models, R.W. Schunk, ed., 53-72, 1996.

Cowley, S.W.H., The auroral ionosphere and its coupling to the magnetosphere and the solar wind, in Modern Ionospheric Science, (Kohl, H., Rüster, R. and Schlegel, K., eds), EGS Publications, Katlenburg-Lindau, 32- 66, 1996.

Fox, N.J., M. Lockwood, S.W.H. Cowley, V.N. Davda, G. Enno, E. Friis-Christensen, R.A. Greenwald, M.R. Hairston, M.G. Kivelson, M. Lester, H. Lühr, D.K. Milling, J.S. Murphree, M. Pinnock and G.D. Reeves, Summary of a multipoint study of a substorm occurring on 7 December 1992, Proc. Third International Conference on Substorms (ICS-3), ESA SP-389, 539-544, 1996.

Gazey, N.G.J., P N. Smith, R P. Rijnbeek, M.J. Buchan and M. Lockwood, The motion of auroral arcs within convective plasma flow, Proc. Third International Conference on Substorms (ICS-3), Versailles, France, 12-17 May 1996, ESA SP-389, 1996.

Kersley, L., S.E. Pryse, I.K. Walker, J.A.T. Heaton, C.N. Mitchell, M.J. Williams and C.A. Willson, Imaging of electron density troughs by tomographic techniques, Proc. Ionospheric Effects Symposium, Alexandria, VA, USA, 1A-2-1 - 1A-2-8, 1996.

Lester, M., N.J. Fox, G.D. Reeves and M.R. Hairston, Ionospheric convection during different phases of magnetospheric substorms, Third International Conference on Substorms (ICS-3), ESA SP-389, 103-108, 1996.

Lockwood, M., The case for transient magnetopause reconnection, EOS, Trans. Am. Geophys. Union, 77, 246-250, 1996.

Turunen, E., H. Matveinen, J. Tolvanen and H. Ranta, D-Region ion chemistry models, STEP Handbook of Ionospheric Models, edited by R.W. Schunk, 1-25, 1996.

Journals and Books, 1997

Anderson, P.C., I.W. McCrea, D.J. Strickland, J.B. Blake and M.D. Looper, Co-ordinated EISCAT/DMSP measurements of electron density and energetic electron precipitation, J. Geophys. Res., 102, 7421, 1997.

Aruliah, A.L., J. Schoendorf, A.D. Aylward and M.N. Wild, Modelling the high-latitude equinoctial asymmetry, J. Geophys. Res., 102, 27207-27216, 1997.

Barr, R. and P. Stubbe, ELF and VLF wave generation by HF heating: a comparison of AM and CW techniques, J. atmos. sol.-terr. Phys., 59, 2265-2279, 1997.

Barr, R., P. Stubbe, M T. Rietveld and E. Nielsen, Enhanced ELF wave generation efficiency using 'O' mode HF heating, Geophys. Res. Lett., 24, 1403-1406, 1997.

Basu, S., E. Costa, R. C. Livingston, K.M. Groves, H.C. Carlson, P.K. Chutrvedi and P. Stubbe, Evolution of sub-kilometre scale ionospheric irregularities generated by high-power HF waves, J. Geophys. Res., 102, 7469-7475, 1997.

Bond, G.E., T.R. Robinson, P. Eglitis, D.M. Wright, A.J. Stocker, M.T. Rietveld and T.B. Jones, Spatial observations by the CUTLASS coherent scatter radar of ionospheric modification by high power radio waves, Ann. Geophys., 15, 1412-1421, 1997.

Breen, A.R., W.A. Coles, R.R. Grall, M.T. Klinglesmith, J. Markkanen, P.J. Moran, B. Tegid and P.J.S. Williams, EISCAT measurements in the solar wind, Ann. Geophys., 14, 1235-1245, 1997.

Cho, Y. N. and J. Röttger, An updated review of polar mesosphere summer echoes: observation, theory, and their relationship to noctilucent clouds and sub-visible aerosols, J. Geophys. Res., 102, 2001-2020, 1997.

Collis, P.N., An improved technique to determine neutral winds in the auroral mesosphere using the EISCAT VHF incoherent scatter radar, J. atmos. sol.-terr. Phys., 59, 1909-1918, 1997.

Collis, P.N. and J.K. Hargreaves, Co-ordinated studies using imaging riometer and incoherent scatter radar, J. atmos. sol.-terr. Phys., 59, 873-890, 1997.

Collis, P.N., J.K. Hargreaves, W.G. Howarth and G.P. White, Joint imaging riometer - incoherent scatter radar observations: a four-dimensional perspective on energetic particle input to the auroral mesosphere, Adv. Space Res., 20, (6)1165-(6)1168, 1997.

Cowley, S.W.H. and M. Lockwood, Incoherent scatter radar observations related to magnetospheric dynamics, Adv. Space Res., 20, (4/5)873-(4/5)882, 1997.

Costa, E., S. Basu, R.C. Livingston, and P. Stubbe, Multiple baseline measurements of ionospheric scintillation induced by high-power HF waves, Radio Sci., 32, 191-197, 1997.

Davies, J.A. and T.R. Robinson, Heating of the high-latitude ionospheric plasma by electric fields, Adv. Space Res., 20, (6)1125 - (6)1128, 1997.

Davies, J.A., M. Lester and I.W. McCrea, A statistical study of ion frictional heating observed by EISCAT, Ann. Geophys., 15, 1399 - 1411, 1997.

del Pozo, C.F., J.K. Hargreaves and A.D. Aylward, Ion composition and effective ion recombination rate in the night-time auroral lower ionosphere, J. atmos. sol.-terr. Phys., 59, 1919-1943, 1997.

Fontaine, D. and C. Peymirat, The large-scale current system and the ionosphere- magnetosphere coupling, Adv. Space Res., 20, 459-467, 1997.

Galand, M., J. Lilensten, W. Kofman and R.B. Sidje, Proton transport model in the high latitude ionosphere. 1 : multistream approach of the transport equation, J. Geophys. Res., 102, 22261-22272, 1997.

Hall, C.M., The influence of negative ions on mesospheric turbulence traced by ionisation: implications for radar and in situ experiments, J. Geophys. Res., 102, 439-443, 1997.

Hall, C.M., Kilometre scale kinetic energy perturbations in the mesosphere derived from EISCAT velocity data, Radio Sci., 32, 93-101, 1997.

Hall, C.M. and U.-P. Hoppe, Characteristic vertical wavenumbers for the polar mesosphere, Geophys. Res. Lett, 24, 837-840, 1997.

Hocking, W.K. and J. Röttger, Studies of polar mesosphere summer echoes over EISCAT using calibrated signal strengths and statistical parameters, Radio Sci., 32, 1425-1444, 1997.

Hubert, D. and F. Leblanc, The auroral O^+ non-Maxwellian velocity distribution function revisited, Ann. Geophys., 15, 249-254, 1997.

Jackel, B.J., D.R. Moorcroft and K. Schlegel, Characteristics of very large aspect angle E-region coherent echoes at 933 MHz, Ann. Geophys., 15, 54-62, 1997.

Jenkins, B., R.J. Moffett, J.A. Davies and M. Lester, Nightside ion frictional heating: atomic and molecular ion temperature anisotropy and ion composition changes, J. atmos sol.-terr. Phys., 59, 1329 - 1341, 1997.

Jones, D.G., I.K. Walker and L. Kersley, Structure of the poleward wall of the trough and the inclination of the geomagnetic field above the EISCAT radar, Ann. Geophys.,15, 740-746, 1997.

Kauristie, K., T.I. Pulkkinen, A. Huuskonen, R.J. Pellinen, D. N. Baker, A. Korth and M. Syrjäsuo, Auroral precipitation fading before and at substorm onset: ionospheric and geostationary signatures, Ann. Geophys., 15, 967-983, 1997.

Kersley L., S.E. Pryse, I.K. Walker, J.A.T. Heaton, C.N. Mitchell, M.J. Williams and C.A. Willson, Imaging of electron density troughs by tomographic techniques, Radio Sci., 32, 1607-1621, 1997.

Kirkwood, S., Thin ion layers in the high-latitude lower ionosphere, Adv. Space. Res., 19, (1)149-(1)158, 1997.

Klostermeyer, J., A height- and time-dependent model of polar mesosphere summer echoes, . J. Geophys. Res., 102, 6715-6727, 1997.

Kosch, M.J., T. Hagfors and D. Rees, A new Fabry-Perot interferometer for atmospheric studies with the EISCAT incoherent scatter radar, Adv. Space Res., 20, (6)1133-(6)1136, 1997.

Lanchester, B. S., M. H. Rees, D. Lummerzheim, A. Otto, H. U. Frey and K. U. Kaila, Evidence for large fluxes of auroral electrons in filaments of 100 m width caused by transient parallel electric fields, J. Geophys. Res., 102, 9741-9748, 1997.

Lathuillere, C., J. Lilensten, W. Gault and G. Thuillier, The meridional wind in the auroral thermosphere : results from EISCAT and WINDII-O^1D co-ordinated measurements, J. Geophys. Res., 102, 4487-4492, 1997.

Lathuillere, C., P.L. Blelly, J. Lilensten and P. Gaimard, Storm effects on the ion composition, Adv. Space Res., 20, 1699-1708, 1997.

Lehtinen, M., A. Huuskonen and M. Markkanen, Randomization of alternating codes: improving incoherent scatter measurements by reducing correlations of gated autocorrelation function estimates, Radio Sci., 32, 2271-2282, 1997.

Lockwood, M., Testing substorm theories: the need for multi-point observations, Adv. Space Res., 20, (4)883-(4)894, 1997.

Markkanen, M. and T. Nygrén, Long alternating codes II: a practical search method, Radio Sci., 32, 9-18, 1997.

Mikhailov, A. and K. Schlegel, Self-consistent modelling of the daytime electron density profile in the ionospheric F-region, Ann. Geophys., 15, 314-326, 1997.

Mishin, E., T. Hagfors and W. Kofman, On origin of out-shifted plasma lines during HF modification experiments, J. Geophys. Res., 102, 27265-27269, 1997.

Mitchell, C.N., L. Kersley, J.A.T. Heaton and S.E. Pryse, Determination of the vertical electron-density profile in ionospheric tomography: experimental results, Ann. Geophys., 15, 747-752, 1997.

Mitchell, C.N., L. Kersley and S.E. Pryse, The effect of receiver location in two-station experimental ionospheric tomography, J. atmos. sol.-terr. Phys., 59, 1411-1415, 1997.

Mitchell, C.N., S E Pryse, L Kersley and I K Walker, The correction for the satellite-receiver longitude difference in ionospheric tomography, J. atmos. sol.-terr. Phys., 59, 2077-2087, 1997.

Nozawa, S., A. Brekke and R. Fujii, Studies of the E-region neutral wind in the auroral ionosphere using two long-run data, J. geomagn. Geoelectr., 49, 641-673, 1997.

Nygrén, T. and M. Markkanen, Long alternating codes 1: search by playing dominoes, Radio Sci., 32, 1-8, 1997.

Nygrén, T., M. Markkanen, M. Lehtinen, E.D. Tereshchenko, and B.Z. Khudukon, Stochastic inversion in ionospheric radiotomography, Radio Sci., 32, 2359-2372, 1997.

Oikarinen, A., J. Manninen, J. Kultima and T. Turunen, Observations of intensity variations and harmonics of the heater induced VLF waves, J. atmos. sol.-terr. Phys., 59, 2351-2360, 1997.

Opgenoorth, H.J., Ground-based supporting programmes for the IASTP, Adv. Space Res., 20, 609-620, 1997.

Opgenoorth, H.J. and M. Lockwood, Opportunities for magnetospheric research with co-ordinated CLUSTER and ground-based observations, Space Sci. Rev., 79, 599-637, 1997.

Peymirat, C. and D. Fontaine, Polar cap convection inferred from EISCAT observations, Ann. Geophys., 15, 403-411, 1997.

Robinson, T.R., A.J. Stocker, G.E. Bond, P. Eglitis, D.M. Wright, and T. B. Jones, O- and X-mode heating effects observed simultaneously with the CUTLASS and EISCAT radars and low power HF diagnostics at Tromsø, Ann. Geophys., 15, 134-136, 1997.

Schlegel, K. and A. V. Gurevich, Radar backscatter from plasma irregularities of the lower E-region induced by neutral turbulence, Ann. Geophys., 15, 870-877, 1997.

Schlesier, A, E. Mishin and K. Schlegel, "Non-collisional" ionisation and temperature layers in the auroral E/F1 layer: EISCAT observations, Geophys. Res. Lett., 24, 1407-1410, 1997.

Sergienko, T., I. Kornilov, E. Belova, T. Turunen and J. Manninen, Optical effects in aurora caused by ionospheric HF-heating, J. atmos. sol.-terr. Phys., 59, 2401-2407, 1997.

Shen, C., M. Zi and K. Schlegel, Two types of ionospheric disturbances in the auroral region, Chinese J. Polar Sci., 8, 8-17, 1997.

Stocker, A.J., T.R. Robinson, T.B. Jones and P. Stubbe, The effect of artificial modification in the E-region on HF ray propagation, J. atmos. sol.-terr. Phys., 59, 2435-2446, 1997.

Stubbe, P. and T. Hagfors, The Earth's ionosphere: a wall-less plasma laboratory, Surveys in Geophysics, 18, 1, 57-127, 1997.

Wannberg, U.G., I. Wolf, L.-G. Vanhainen, K. Koskenniemi, J. Röttger, M. Postila, J. Markkanen, R. Jacobsen, A. Stenberg, R. Larsen, S. Eliassen, S. Heck and A. Huuskonen, The EISCAT Svalbard Radar, a case study in modern incoherent scatter radar system design, Radio Sci., 32, 2283-2307, 1997.

Yeoman, T.K., D.M. Wright, T.R. Robinson, J.A. Davies and M. Rietveld, High spatial and temporal resolution observations of an impulse-driven field line resonance in radar backscatter artificially generated with the Tromsø heater, Ann. Geophys., 15, 634-644, 1997.

Theses, 1997

Bond, G.E., The interaction of radio waves with the auroral ionosphere, Ph.D. thesis, University of Leicester, UK, 1997.

Chaxel, Y., Radar and modelling studies of polar mesospheric summer echoes, Ph.D. thesis, University of London, UK, 1997.

Foster, C., Auroral ion upflows in the F-region and topside ionosphere, Ph.D. thesis, University of Leicester, UK, 1997.

Muller-Wodarg, I.C.F., Modelling tides propagating through the mesopause into the Earth's upper atmosphere, Ph.D. thesis, University College, London, UK, 1997.

Olsson, A., Studies of magnetosphere ionosphere coupling in auroral substorms using radar and satellite techniques, Ph.D. thesis, Uppsala University, Swedish Institute of Space Physics, Scientific Report 240, 1997.

Saito, S., Electron temperature enhancements associated with strong electric fields in the polar E-region using EISCAT CP-1 data, Master thesis, Nagoya University, Japan, 1997.

Westman, A., Development of high resolution radar measurements techniques for studies of transient phenomena in the ionospheric E and F layers, Ph.D. thesis, University of Umeå, Sweden, IRF Scientific Report 246, 1997.

Proceedings, Reports, etc., 1997

Hagfors, T., Plasma fluctuations excited by charged particle motion and their detection by weak scattering of radio waves, in Incoherent Scatter: Theory, Practice and Science, (Ed.) D. Alcaydé, EISCAT Scientific Association, Kiruna, 1-32, 1997.

Hall, C.M., B. Hansen, B.-O. Husøy, U.-P. Hoppe and A.P. van Eyken, Telescience with the EISCAT incoherent scatter radars and Universities of Tromsø and Saskatchewan MF radar, Proc. 13th ESA Symposium, Öland, Sweden, 26-29 May 1997, ESA SP-397, 1997.

Kirkwood, S., The anomalous winter ion layer – a mystery waiting for a sounding rocket, Proc. 13th ESA Symposium, Öland, Sweden, 26-29 May 1997, ESA SP-397, 371-374, 1997.

Pryse, S.E., L. Kersley, C.N. Mitchell and M.J. Williams, Developments in the reconstruction of images of the auroral ionosphere, Proc. Computerized Ionospheric Tomography (CIT) Conference (Algorithms, Geophysics and Applications), Univ. of Texas at Austin, Texas, USA, 1997.

Röttger, J., Radar observations of the lower and middle atmosphere, in Incoherent Scatter: Theory, Practice and Science, (Ed.) D. Alcaydé, EISCAT Scientific Association, Kiruna, 263-314, 1997.

Schlegel, K., The use of incoherent scatter data in ionosphere and plasma research, in Incoherent Scatter: Theory, Practice and Science, (Ed.) D. Alcaydé, EISCAT Scientific Association, Kiruna, 89-120, 1997.

Spencer, P., A new solution to the problem of ionospheric tomography using convex optimisation, Proc. Computerized Ionospheric Tomography (CIT) Conference (Algorithms, Geophysics and Applications), Univ. of Texas at Austin, Texas, USA, 1997.

EISCAT REPORTS AND MEETINGS

Reports 1996 - 1997:

EISCAT Annual Report 1994/1995		
EISCAT Technical Report 97/53	Incoherent Scatter: Theory, Practice and Science	D. Alcaydé

Brochure:

EISCAT	July 1996
The EISCAT Svalbard Radar- An evolutionary step into EISCAT´s future	Leaflet April 1997

Meetings 1996:

COUNCIL	46th meeting, 20/21 May	Oslo, Norway
	47th meeting, 25/26 Nov.	Tromsö, Norway
SAC	50th meeting, 10/11 May	Den Haag, Netherlands
	51st meeting, 14/15 Nov.	Copenhagen, Denmark
AFC	46th meeting, 18/19 April	Copenhagen, Denmark
	47th meeting, 28 October	Stockholm, Sweden

Meetings 1997:

COUNCIL	48th meeting, 12/13 May	Copenhagen, Denmark
	49th meeting, 17/18 Nov.	Kiruna, Sweden
SAC	52nd meeting, 23/24 April	Vienna, Austria
	53rd meeting, 17/18 Oct.	Toulouse, France
AFC	48th meeting, 14 April	Copenhagen, Denmark
	49th meeting, 26 Sept.	Hamburg, Germany

EISCAT Scientific Association

BALANCE SHEET 1996

As at 31.12.96

Values in SEK

Fixed Assets

	Book Value 31.12.95	Additions	Disposal	Depreciation	Book Value 31.12.96
KST					
Buildings	8 107 447			351 498	7 755 950
Tenancy	93 117	10 228		1 935	101 410
VSQ	207 829			28 302	179 527
Transmitter	20 356 723			2 005 497	18 351 226
UHF Antenna	4 167 555			1 318 871	2 848 684
VHF Antenna	6 697 729			1 541 362	5 156 367
Time & Frequency		141 785			141 785
Computers	2 461 869	619 981		659 833	2 422 017
Vehicles	747 260	140 320	76 594	178 279	632 707
Office & Workshop	775 213	245 460		219 616	801 056
Instrumenation	608 132	82 926		225 911	465 146
	44 222 875	1 240 700	76 594	6 531 104	38 855 876
ESR					
Computers	1 754 620	714 392		287 372	2 181 640
Vehicles	297 309	309 031		84 159	522 181
Office & Workshop	573 127	55 999		136 541	492 585
Instrumentation	844 098	208 766		226 737	826 127
Transmitter	13 620 404	3 725 637			17 346 041
Antenna	33 323 085	9 256 458			42 579 543
Site Building	25 122 069	366 944			25 489 013
Testhall	161 709			17 968	143 741
Receiver	739 906	54 564			794 470
Data Acquisition	1 465 293	1 585 717			3 051 010
Controller	300 795	37 334			338 129
Peripheral	124 060	69 115			193 176
Housing	1 790 018	190 928		187 522	1 793 424
	80 116 494	16 574 885	0	940 299	95 751 079
KST + ESR Total	124 339 369	17 815 586	76 594	7 471 403	134 606 956

Current Assets

	Book Value 31.12.95	Book Value 31.12.96
EISCAT Total		
Site Advance	1 004 842	239 640
Prepayments and accrued inc.	386 639	133 423
Petty Cash	3 130	1 828
Debtors:		
Value added tax	545 397	485 425
Others	10 554	16 074
Associate contribution	5 559 438	0
Banks:		
Special Accounts	4 424 828	2 762 123
Ordinary Accounts	25 793 767	73 772 728
	37 728 596	77 411 239
Total Assets (Current + Fixed)	162 067 966	**212 018 195**

Capital and Liabilities

Capital

	1995	1996
Funds invested		
Pool	94 298 256	94 298 256
UHF Spare Klystron	3 019 411	3 019 411
Capital Operating	27 609 903	28 773 009
In Kind	25 123 200	25 123 200
Other	421 160	421 160
Heating	2 289 000	2 289 000
ESR	78 050 608	94 625 494
(gross)	230 811 538	248 549 530
Depreciation	-106 472 169	-113 942 573
(net)	124 339 369	134 606 956
Funds held on reserve		
Evolutionary Development fund	1 296 536	63 083 170
Evolutionary Interest fund	67	CLOSED
Klystron Fund	0	0
Spare parts reserve	611 462	764 405
Capital Operating reserve	7 401 716	3 320 044
KST Surplus Fund	0	368 738
ESR Construction Project Fund	18 126 378	CLOSED
	27 436 159	67 536 357
Special Account	4 424 828	2 762 123
Total Capital	156 200 356	204 905 436

Liabilities

Liabilities		
Creditors	2 092 812	6 933 152
Provisions	447 011	179 608
Associate contribution prepayment	3 327 787	0
	5 867 610	7 112 759
Total (Capital + Liabilities)	162 067 966	**212 018 195**

Values in MSEK

Recurrent Expenditure 1996

	Outcome	*Budget*
Personnel	**12 051**	*12 142*
Administration	**5 226**	*5 100*
Operation	**3 998**	*4 250*
Total (KST)	**21 275**	*21 492*
ESR Project	**5 759**	*6 827*

EISCAT Scientific Association

BALANCE SHEET 1997

As at 31.12.97

Values in SEK

Fixed Assets

	Book Value 31.12.96	Additions	Disposal	Depreciation	Book Value 31.12.97
Computers	4 603 657	262 934	80 290	993 739	3 792 561
Vehicles	1 154 888	380 307	148 000	245 649	1 141 547
Office & Workshop	1 293 642	120 700		394 390	1 019 951
Instrumentation	1 291 274	210 631		441 668	1 060 236
ESR Transmitter	17 346 041	13 420 426		1 734 604	29 031 863
ESR Antenna	42 579 543	50 660		4 257 954	38 372 249
ESR Site Building	25 489 013	621 561		2 548 901	23 561 673
ESR Testhall	143 741			17 967	125 774
ESR Receiver	794 470			79 447	715 023
ESR Data Acquisition	3 051 010	1 662 950		811 363	3 902 597
ESR Controller	338 129	33 802		33 813	338 118
ESR Peripheral	193 176			19 318	173 858
ESR Housing	1 793 424	6 744		206 615	1 593 553
KST Buildings	7 755 950		0	349 363	7 406 586
KST Tenancy	101 410	38 033		2 139	137 304
KST VSQ	179 527		0	28 891	150 636
KST Transmitter	18 351 226		0	2 029 197	16 322 029
KST UHF Antenna	2 848 684	1		1 310 009	1 538 675
KST VHF Antenna	5 156 367	0		1 559 846	3 596 521
KST Receivers	0	53 225			53 225
KST Time & Frequency	141 785			14 179	127 606
	134 606 956	16 861 974	228 290	17 079 054	134 161 586

Current Assets

	Book Value 31.12.96	Book Value 31.12.97
EISCAT Total		
Site Advance	239 640	0
Prepayments and accrued inc.	133 423	528 971
Petty Cash	1 828	2 464
Debtors:		
Value added tax	485 425	348 214
Others	16 074	67 134
Associate contribution	0	2 061 464
Banks:		
Special Accounts	2 762 123	0
Ordinary Accounts	73 772 728	60 934 475
	77 411 239	63 942 721
Total Assets (Current + Fixed)	212 018 195	**198 104 307**

Capital and Liabilities

Capital

	1996	**1997**
Funds invested		
Pool	94 298 256	94 298 256
UHF Spare Klystron	3 019 411	3 019 411
Capital Operating	28 773 009	29 342 771
In Kind	25 123 200	25 123 200
Other	421 160	421 160
Heating	2 289 000	2 289 000
ESR	94 625 494	110 689 416
(gross)	248 549 530	265 183 215
Depreciation	-113 942 573	-131 021 629
(net)	134 606 956	134 161 586
Funds held on reserve		
Evolutionary Development fund	63 083 170	50 349 953
Spare parts reserve	764 405	755 556
Capital Operating reserve	3 320 044	3 635 385
Surplus Fund	368 738	3 588 496
	67 536 357	58 329 390
Special Account	2 762 123	0
Total Capital	204 905 436	192 490 975

Liabilities

Liabilities		
Creditors	6 933 152	5 395 332
Provisions	179 608	218 000
	7 112 759	5 613 332
Total (Capital + Liabilities)	212 018 195	**198 104 307**

Values in MSEK

Recurrent Expenditure 1997

	Outcome	*Budget*
Personnel	**12 392**	*14 158*
Administration	**6 658**	*7 320*
Operation	**5 094**	*6 681*
Total	**24 144**	*28 160*

The EISCAT Svalbard Radar (ESR) is from 1997 included in the normal operation.

EISCAT Associate contributions MSEK

1996	Contribution	Percentage
CNRS (France)	6 238	25%
MPG (Germany	6 238	25%
NFR (Sweden)	2 495	10%
PPARC (United Kingdom)	6 238	25%
RCN (Norway)	2 495	10%
SA (Finland)	1 248	5%
	24 951	100%

1997	Contribution	Percentage
CNRS (France)	6 564	23,25%
MPG (Germany	6 564	23,25%
NFR (Sweden)	2 626	9,30%
NIPR (Japan)	1 976	7,00%
PPARC (United Kingdom)	6 564	23,25%
RCN (Norway)	2 626	9,30%
SA (Finland)	1 313	4,65%
	28 234	100,00%

EISCAT Svalbard Radar Project Financial Outcome MSEK

Investments	1990-1996	1997	1998-	Total
Computers	2 703			2 703
Vehicles	730			730
Office & Workshop	739			739
Instrumentation	1 346			1 346
Transmitter	17 346	13 420	1 200	31 966
Antenna	42 580	51	37 300	79 930
Site Building	25 489	622		26 111
Testhall	180			180
Receiver	794		1 100	1 894
Data Acquisition	3 051	1 663		4 714
Controller	338	34		372
Peripheral	193			193
Housing	2 066	7		2 073
	97 555	15 796	39 600	152 951

Recurrent		
Personnel	7 582	*1997 and onwards: ESR recurrent*
Administration	7 881	*in the normal budget.*
Operation	6 473	
	21 937	

Grand total (Investment + Recurrent)	**174 888**

EISCAT Svalbard Radar Project Funding MSEK

Source	1990-1997	Percentage
CNRS (France)	14 007	8%
MPG (Germany	7 186	4%
NFR (Sweden)	20 038	11%
NIPR (Japan)	41 928	24%
PPARC (United Kingdom)	24 961	14%
RCN (Norway)	43 867	25%
SA (Finland)	11 006	6%
EISCAT and other income	11 567	7%
	174 560	100%

EISCAT SCIENTIFIC ASSOCIATION
Dec. 1996

	Finland	France	Germany	Japan (1)	Norway	Sweden	United Kingdom
COUNCIL	J. Kangas T. Turunen	M. Aubry W. Kofman	G. Haerendel T. Hagfors * M. Meinecke	R. Fujii T. Hirasawa S. Kokubun	A. Brekke B. Benterud	J. Gustavsson H. Opgenoorth	G. Brooks T. B. Jones M. Lockwood
SAC	M. Lehtinen	D. Alcaydé	W. Baumjohann (2) K. Rinnert (2)	T. Ogawa	C. La Hoz	S. Kirkwood	P.J.S. Williams *
AFC	E. Ikonen *	G. Leliévre	A. Röhr	C. Maeda	A. Andersen	F. Karlsson	G. Brooks

SAC = Scientific Advisory Committee; AFC = Administrative and Finance Committee; * = Chairperson

(1) Japan joined EISCAT 1 April 1996

(2) W. Baumjohann replaced K. Rinnert from the 51st SAC meeting

EISCAT Senior Staff:

Director: J. Röttger (on secondment from MPG)
Deputy Director Science: A.P. van Eyken
Deputy Director Technical: U. G. Wannberg
Executive Assistant: H. Andersson

Site Leaders:
Kiruna: I Wolf
Sodankylä: M. Postila
Tromsö Radar: R. Jacobsen
Tromsö Heating: M. Rietveld

Non-Associate member of SAC was A. D. Richmond (USA)

EISCAT SCIENTIFIC ASSOCIATION
Dec. 1997

	Finland	France	Germany	Japan	Norway	Sweden	United Kingdom
COUNCIL	J. Kangas T. Turunen	D. Alcaydé W. Kofman * J. F. Minster	G. Haerendel T. Hagfors M. Meinecke	R. Fujii T. Hirasawa S. Kokubun	A. Brekke K. Kveseth (1) T. O. Moen (1)	J. Gustavsson H. Opgenoorth	G. Brooks T. B. Jones M. Lockwood
SAC	M. Lehtinen	C. Lathuillere	W. Baumjohann	T. Ogawa	C. La Hoz *	S. Kirkwood	P.J.S. Williams
AFC	M. Vihma-Kaurinkoski	G. Debouzy	A. Röhr	C. Maeda	A. Andersen	F. Karlsson	G. Brooks *

SAC = Scientific Advisory Committee; AFC = Administrative and Finance Committee; * = Chairperson

(1) K. Kveseth replaced T. O. Moen from the 49th Council meeting

EISCAT Senior Staff:

Director: J. Röttger (on secondment from MPG)

Deputy Director Science: A.P. van Eyken

Deputy Director Technical: U. G. Wannberg

Executive Assistant: H. Andersson

Site Leaders:

Kiruna: I Wolf

Sodankylä: M. Postila

Tromsö Radar: R. Jacobsen

Tromsö Heating: M. Rietveld

Non-Associate member of SAC was P. Stauning (Denmark)

Annual Report 1996-1997 of the EISCAT Scientific Association

EISCAT Headquarters
P.O. Box 812, S-981 28 Kiruna, Sweden

Scientific contributions: EISCAT Associates and staff
Finishing and printing: Tryckerikompaniet, Kiruna

ISSN 0349-2710, September 1999

THE EISCAT ASSOCIATES

December 1997

SA
Suomen Akatemia
Finland

CNRS
Centre National de la Recherche Scientifique
France

MPG
Max-Planck-Gesellschaft
Germany

NIPR
National Institute of Polar Research

Japan

RCN
Research Council of Norway
(Norges Forskningsråd)
Norway

NFR
Naturvetenskapliga Forskningsrådet
Sweden

PPARC
Particle Physics and Astronomy Research Council
United Kingdom

EISCAT Scientific Association

HEADQUARTERS

EISCAT Scientific Association
Box 812
SE-981 28 KIRUNA, Sweden
Phone +46-980-79153
Fax +46-980-79161
email: eiscat@eiscathq.irf.se

SITES

Kiruna

EISCAT
Swedish Institute of Space Physics
Box 812
SE-981 28 KIRUNA, Sweden
Phone +46-980-79136
Fax +46-980-79161
email: eiscat@eiscat.irf.se

Sodankylä

EISCAT
Geophysical Observatory
FIN-99600 SODANKYLÄ, Finland
Phone +358-16-619880
Fax +358-16-610375
email: eiscat@eiscat.sgo.fi

Tromsø

EISCAT
Ramfjordmoen
N-9027 Ramfjordbotn, Norway
Phone +47-776-92166
Fax +47-776-92380
email: eiscat@eiscat.uit.no

Longyearbyen

EISCAT Svalbard Radar
P.O. Box 432
N-9171 Longyearbyen, Norway
Phone +47-7902 1236
Fax +47-7902 1751
email: eiscat@esr.eiscat.no